Title
Nanotechnology for Improving Sensitivity and Quantitative Capabilities of Paper-Based Diagnostic Devices

Author
Bradbury, Daniel

Publication Date
2020

UNIVERSITY OF CALIFORNIA

Los Angeles

Nanotechnology for Improving Sensitivity and Quantitative Capabilities of Paper-Based Diagnostic Devices

A dissertation submitted in partial satisfaction of the
requirements for the degree Doctor of Philosophy
in Bioengineering

by

Daniel William Bradbury

2020

ABSTRACT OF THE DISSERTATION

Nanotechnology for Improving Sensitivity and Quantitative Capabilities of Paper-Based Diagnostic Devices

by

Daniel William Bradbury

Doctor of Philosophy in Bioengineering

University of California, Los Angeles 2020

Professor Daniel T. Kamei, Chair

Providing effective healthcare to underrepresented populations is a major challenge worldwide due to environmental, economic, and social disparities. Both developing countries and low income rural/urban areas in the US tend to have reduced healthcare access which limits the frequency and quality of medical screenings as well as treatment options. This has led to an increased effort in the development of point-of-care devices which emphasize, immediate and onsite results. One device that has the potential to fulfill these requirements is the lateral-flow immunoassay (LFA). While the LFA has been successful in the form of the over-the-counter pregnancy test, it still does have some disadvantages that limit its ability to fully replace sophisticated laboratory-based assays. Throughout this thesis, I will be discussing the development

of cutting-edge technologies to address the two major disadvantages of the LFA which are its poor quantitative characteristics and low sensitivity.

Cerebrospinal fluid (CSF) leaks are a common complication of numerous procedures in Otolaryngology. These leaks are relatively difficult to diagnose and the current laboratory-based tests to do so have a turn-around time that is unacceptable for rapid clinical decision making. We addressed this problem by developing the first rapid diagnostic test kit for the detection of CSF leaks. In Chapter 2, we describe the development of a barcode-style LFA for the semi-quantitative detection of beta-trace protein, which is present in CSF at high concentrations. This work was expanded upon in Chapter 3, where we created a complete, standalone rapid diagnostic test kit composed of our barcode-style LFA, a collection swab, dilution buffers, disposable pipettes, and instructions. Clinical studies demonstrated excellent predictive capabilities of this kit in distinguishing patient samples containing CSF from those that did not.

In some cases, a more quantitative readout than what the barcode-style LFA can achieve is required. In Chapter 4, we developed a new technique to introduce an even more quantitative readout to the LFA without the need of electronic readers. This technology was applied to the therapeutic drug monitoring of the cardiac glycoside digoxin. Digoxin capture and binding occurs on a modified LFA test strip which utilizes platinum nanozyme probes that possess catalase-like activity. This test strip is combined with a reaction that controls the anisotropic etching of gold nanorods to produce a wide range of visible color hues dependent on the initial digoxin concentration in the sample which allowed for naked-eye quantification.

We then shifted to the development of technologies to improve the detection limit and sensitivity of the LFA. Our lab previously discovered the phenomenon of an aqueous two-phase system (ATPS) separating on paper, which allowed for the seamless integration of biomarker preconcentration and detection on the LFA. In Chapter 5, we have extended the functionality of an ATPS separating on paper to automate the sequential delivery of signal enhancement reagents in addition to concentrating biomarkers. The timing of reagent delivery was controlled by changing the initial composition of the ATPS and a mathematical model was developed to help predict the ATPS flow behavior. We applied this technology to automate biomarker preconcentration and nanozyme signal enhancement on the LFA, resulting in a 30-fold improvement in detection limit over the conventional LFA when detecting *Escherichia coli*, all while maintaining a single application step.

In late 2019, a new virus known as SARS-CoV-2 began to sweep across the globe, leading to the COVID-19 pandemic. The development of highly sensitive and easily deployable rapid diagnostic tests is a vital aspect of managing this pandemic. In Chapter 6, we discuss ongoing efforts to develop a highly sensitive, nanozyme signal enhanced LFA for the rapid detection of the SARS-CoV-2 nucleocapsid protein. A 3D-printed casing was designed to store the test strip and all reagents in a way that maintains user friendly operation by eliminating liquid handling steps. Besides developing highly sensitive diagnostics, the ability to deploy these tests quickly and in a highly scalable manner is crucial for being able to manage a pandemic. The work described in Chapter 7 highlights the integration of novel fibronectin-based antibody mimetics, called monobodies, into the LFA for the detection of the nucleocapsid protein of SARS-CoV-2. These monobodies are advantageous over monoclonal antibodies in that they are rapidly developed and produced recombinantly in *Escherichia coli* which is more affordable and scalable than monoclonal antibody production.

The dissertation of Daniel William Bradbury is approved.

Aaron Meyer

Dino Di Carlo

Benjamin Wu

Daniel T. Kamei, Committee Chair

University of California Los Angeles

2020

This work is dedicated to my family who has always encouraged and supported me

TABLE OF CONTENTS

TABLE OF FIGURES

ACKNOWLEDGMENTS

This work absolutely could not have been done without the mentorship, friendship, support, and encouragement of so many individuals. My biggest thanks go out to my advisor, Dr. Daniel T. Kamei. This has been said many times over the years, but Dan really is one of the best mentors anyone could possibly hope for as well as an amazing friend. Dan's class, BE201 Engineering Principles of Drug Delivery, was one of the most challenging yet enjoyable and rewarding classes I have ever taken. This class was taken during my first quarter at UCLA and I was immediately struck by the passion and dedication that Dan had for teaching. As the quarter progressed, it became more and more clear to me that joining Dan's lab and being mentored by him was the path that I wanted to take. He cares so much about every single individual he works with, and constantly pushes and challenges them to reach their full potential. Members of the lab learn quickly that while obtaining data is important, it is not what is most important to Dan. Rather, he is completely dedicated to and motivated by the personal and professional growth of his students. It is always what we learn along this journey that is most important to him. I cannot thank Dan enough for the lessons that I have learned and for working so hard to establish such an amazing and supportive culture for the entire lab.

There are also many past and present members of the lab who made this time in graduate school so memorable. When I first joined the lab, Phuong Nguyen welcomed me into the lab and trained me on lab protocols. Ricky Chiu, was a great mentor to me who really motivated and encouraged me to think big early on. Kristine Mayle was always so full of energy which helped balance out some of the tiredness and brought the lab to life. I always admired Garrett Mosley for his work ethic and drive to do whatever it took to get the job done. David Pereira and Sherine

Cheung were both my TAs for BE201. My conversations with David about the lab were one of the reasons I was joined. He'd also always be down for a boba or food run. Honestly it was a shock to me when I joined the lab just how much all the grad students in the lab ate. They introduced me to this wonderful place called Sawtelle Boulevard and I was very well fed. Garrett, David, and I also have a similar, goofy sense of humor filled with face-palm worthy and cringy jokes so there was never dull moment when we were all in the office together (…sorry Sherine). Sherine has been one of my best friends and biggest supporters throughout my time at UCLA. I honestly cannot imagine having gone through this experience without her sitting next to me every day for 5 years. She was always available to talk and encourage me, even during my last year when she had already left the lab. I truly treasure all of the memories we have made together and adventures we have gone on over these years. Allison, who became a good friend during her time as an MS student, was also very supportive and fun to be around during late night study or lab sessions. Nguyen Le joined the lab as an undergrad around the same time I joined as a PhD student. It was great to have him around all the way through his MS, and I always enjoyed our conversations about football and classical music over Tsujita.

I am very grateful for all the students who I have worked with and have helped on my research projects over the years. April Pan was the first student who I worked with. She really helped get the ACE-LFA project started and designed a casing which was vital to the success of the project. Milad Azimi, Alexia Diaz, and Ceci Falktoft all joined the ACE-LFA project a couple years later and helped finish this work. Milad also brought a lot of device building and 3D printer knowledge to the lab which has been very helpful in numerous projects. Jasmine joined the lab right before her second year at UCLA and around the time that I had the idea for the quantitative, multicolor LFA project. Because I was focusing on finishing the ACE-LFA work at the time, I tossed this brand new project and a lot of responsibility on her plate. Even though she was very new to research, Jasmine really took ownership of this project and has been pushing it forward since. It has been an absolute pleasure to work with her and watch her develop into a mature researcher, role model, and leader in the lab. Milo Ryan joined the team the following year and helped combine the LFA with the in-solution GNR etching discussed in this thesis. I'm also grateful to Cassandra Cantu as well as Jasmine and Milo for all the work they have put in during the COVID-19 pandemic to develop a more sensitive rapid antigen test. Jerry Lu has been working to apply the ACE-LFA technology to the detection of human antibodies against SARS-CoV-2, and I appreciate his efforts to continue developing these technologies after I leave the lab. I would also like to thank all the other members of the Kamei lab for their friendship and support over the years. This is a very tight knit, family-type environment and I will cherish all the memories I have made here for the rest of my life.

I'd also like to acknowledge the friends who have supported me along the way. Jesse Liang allowed Arshia Ehsanipour, Joe de Rutte, and I to take over his desk multiple times per day to make coffee and hang out in the 5th floor student offices. Our random conversations about politics, coffee science, video games, and the latest non-coffee scientific developments were always a much needed break during some very long days in lab. When campus shut down during the COVID-19 pandemic, our little coffee club made the transition to the virtual world and we continue to talk almost every day. I am also extremely grateful to the Probst family as they have become a home away from home for me. I cannot thank them enough for welcoming me into their home during holidays when I could not travel back to NJ, and always making me feel like a part of their family.

Finally, I want to thank all my family members for their love, understanding, and support while I went through the journey. I know there were times where I would basically drop off the face of the earth and you wouldn't hear from me for weeks, but I always knew you were all still there to encourage me and root me on. I could always call Katie to talk about daily life in lab and our frustrations with our research. Whenever I went home for Christmas, Katie and Jim would always house me for a few days to hang out and spend time with my nieces, Ellie and Ginny. Gail was also always willing to pick me up early from red eye flights and appreciate (or at least fake it well!) the weird videos and jokes I would randomly send her. I also always looked forward to receiving letters mailed every few weeks by my Grandma. It definitely shows that I am her favorite youngest grandson! Of course a special thanks to my parents, Keith and Susan, for their endless patience, always keeping me accountable, and teaching me the importance of hard work. I was one of the most forgetful children imaginable and not always so easy to deal with, especially in middle school. I remember a stretch of time when my mom had to drive me back to school almost every day to pick up books that I forgot to bring home so that I could complete my homework. Even though I must have been incredibly frustrating at times, they never gave up on me and because of the lessons they have taught me over the years, I successfully could navigate graduate school. While I may not always express it, I love all of you very much and would not be the person I am today without you.

Chapter 2 is a version of A.E. Kita, D.W. Bradbury, Z.D. Taylor, M. St. John, D.T. Kamei. *Point-of-care cerebrospinal fluid detection.* Otolaryngology – Head and Neck Surgery, 2018, 159: 824-829, doi: 10.1177/0194599818789075. Sage Publications Copyright © 2018 Reprinted with permission from Sage Publications. Ashley Kita was the director of research for this article. This work was supported by a 2016 AAO-HNS Core Resident Research Award to A.E. Kita and a U.S. National Institute of Health grant 1R21NS099800-01 to D.T. Kamei and M.A. St. John.

Chapter 3 is a version of D.W. Bradbury, A.E. Kita, K. Hirota, M.A. St. John, and D.T. Kamei, *Rapid diagnostic test kit for point-of-care cerebrospinal fluid leak detection*, SLAS Technology: Translating Life Sciences Innovation, 2020, 25: 67-74, doi: 10.1177/2472630319877377. Sage Publications Copyright © 2020 Reprinted with permission from Sage Publications. D.T. Kamei was the director of research for this article. This work was supported by a 2016 AAO-HNS Core Resident Research Award to A.E. Kita and a U.S. National Institute of Health grant 1R21NS099800-01 to D.T. Kamei and M.A. St. John.

Chapter 5 is a version of D.W. Bradbury, M. Azimi, A.J. Diaz, A.A. Pan, C.H. Falktoft, B.M. Wu, and D.T. Kamei, *Automation of biomarker preconcentration, capture, and nanozyme signal enhancement on paper-based devices,* Analytical Chemistry, 2019, 91: 12046-12054. American Chemical Society © 2019 Reprinted with permission from American Chemical Society. D.T. Kamei was the director of research for this article. This work was supported by National Science Foundation grant 1707194 to D.T. Kamei.

VITA

2014	B.S., Biomedical Engineering Rutgers University New Brunswick, NJ
2015-2019	Teaching Assistant Department of Bioengineering University of California, Los Angeles Los Angeles, CA
2017	M.S., Bioengineering University of California, Los Angeles Los Angeles, CA

PUBLICATIONS

D.W. Bradbury[*], A.E. Kita[*], K. Hirota, M.A. St. John, and D.T. Kamei, “Rapid diagnostic test kit for point-of-care cerebrospinal fluid leak detection,” *SLAS Technology*, **25** (2020) 67-74.
*These authors contributed equally to this article

D.W. Bradbury, M. Azimi, A.J. Diaz, A.A. Pan, C.H. Falktoft, B.M. Wu, and D.T. Kamei, “Automation of biomarker preconcentration, capture, and nanozyme signal enhancement on paper-based devices,” *Anal. Chem.*, **91** (2019) 12046-12054.

A.E. Kita[*], **D.W. Bradbury**[*], Z.D. Taylor, M. St. John, D.T. Kamei. Point-of-care cerebrospinal fluid detection. *Otolaryngol. Neck Surg.,***159** (2018) 824-829
*These authors contributed equally to this article

PATENTS

US. Patent application, PCT/US18/24392, “Semi-quantitative lateral-flow immunoassay for the detection of CSF leaks,” filed March 26, 2018 (provisional application filed March 27, 2017)

U.S Patent application, PCT/US2017/036418, “Biomarker concentration and signal amplification for use in paper-based immunoassays and a single platform for extracting, concentrating, and amplifying DNA,” filed June 7, 2017 (provisional application filed June 9, 2016)

Chapter 1. Motivation and Background

1.1. Introduction

1.1.1. Point-of-care disease detection in resource-limited settings

It was reported that in 2016, the top 10 causes of death worldwide included both communicable and non-communicable diseases, where ischaemic heart disease and stroke lead with a combined 15.2 million deaths.[1] Ischaemic heart disease and stroke, which are both non-communicable disease, have remained the leading causes of death globally for the last 15 years. In the US, cardiovascular diseases disproportionally affect underrepresented populations, which are often in rural or urban areas.[2] These areas tend to have reduced healthcare access which limits the frequency and quality of medical screenings as well as treatment options.

While non-communicable diseases account for a majority of the 10 top causes of death in the American regions, 7 out of the 10 top causes of deaths in the African region are communicable, infectious diseases including lower respiratory infections, HIV/AIDs, and diarrhoeal diseases.[1] The greater prevalence of these communicable diseases in the African region compared to the Americas is a direct result of environmental, economic, and social disparities.[3] These disparities are responsible for the lack of basic sanitation, healthcare clinics, and centralized laboratories in these resource-limited regions, which are important for preventing infectious disease transmission.[4]

Treatments and therapies for many of these infectious diseases are available, however a lack of accurate diagnostic technologies to provide early disease detection makes successful intervention and treatment difficult in resource-limited regions. Ultimately, many deaths from infectious diseases could have been prevented if diagnosed earlier.[5] The current gold standard diagnostic technologies capable of providing accurate detection (enzyme-linked immunosorbent assay, polymerase chain reaction, high performance liquid chromatography, mass spectroscopy, etc.) are not suitable for use in developing, resource-limited countries which lack access to electricity, laboratory equipment, and trained personnel. This has led to a growing effort in the development of point-of-care diagnostic devices, which emphasize immediate and on-site testing.

The World Health Organization (WHO) has provide the ASSURED criteria to guide the development of diagnostic assays for detecting infectious diseases in resource-limited settings.[6] According to this criteria, diagnostics devices should aim to be:

- **A**ffordable by those at risk of infection
- **S**ensitive (low occurrences of false positives)
- **S**pecific (low occurrences of false negatives)
- **U**ser-friendly (simple to use and requiring minimal training)
- **R**apid and robust
- **E**quipment-free
- **D**elivered to the end user

While the ASSURED criteria were originally put forward with a focus on infectious disease detection in developing countries, these criteria are also useful for guiding the development of rapid screening tests to be used in middle/high-income countries, particularly to address disparities in healthcare that occur in the urban and rural areas that are often neglected. Additionally, devices developed under these criteria can be suitable for environmental and military field testing, rapid decision making in hospital settings, mobile clinics with limited space, and at-home screening/monitoring for increasing patient convenience.

1.1.2. Lateral-flow immunoassay

One assay that can potentially satisfy the ASSURED criteria for an effective POC device is the lateral-flow immunoassay (LFA). The LFA is a paper-based device that utilizes antibodies specific to a target antigen which are conjugated to a colorimetric indicator, usually gold nanoparticles or latex beads, to produce a readable signal. **Figure 1-1** illustrates a typical LFA setup, which is comprised of several different zones that are constructed of different, overlapping paper materials.

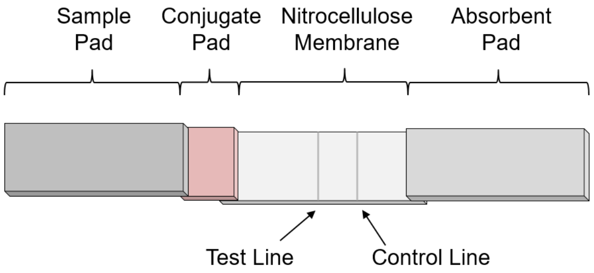

Figure 1-1 General schematic of a conventional lateral-flow immunoassay test strip.
Sample is applied to the sample pad. The conjugate pad stores the dehydrated colorimetric indicator. Binding proteins are immobilized to form the test and control lines on the nitrocellulose membrane. The absorbent pad provides a fluid sink to drive flow of sample through the strip.

In the conventional LFA test, the sample solution is applied to the sample pad of the test strip, located at the most upstream end of the strip. The sample then flows into the conjugate pad, where it will resolubilize the dehydrated, antibody-conjugated gold nanoprobes or latex particles which serve as the colorimetric indicator for the assay. The solution will next reach the nitrocellulose membrane which contains proteins immobilized at the test and control lines which make up the LFA detection zone. Finally, the sample solution will flow out of the nitrocellulose membrane and into the absorbent pad, which serves to drive fluid flow, ensuring that all of the sample crosses the LFA detection zone.

There are two main formats of the LFA: the sandwich and the competitive assay formats. Sandwich assays are suited for the detection analytes with multiple binding epitope sites, such as proteins, viruses, or bacteria. In the sandwich assay format (**Figure 1-2**), primary antibodies specific for the target analyte are immobilized on the nitrocellulose membrane to form the test line. If the target analyte is present in the sample solution, they will bind to the test line antibodies. The colorimetric gold indicator also contains primary antibodies against the target analyte, and will bind to the captured analyte at the test line, where the analyte becomes "sandwiched". Excess colorimetric indicator is captured further along the strip by secondary antibodies specific to the primary antibodies conjugated to the colorimetric indicator which form the control line. A visible control line indicates that the test is valid and that the sample has flowed throughout the membrane. In other words, if the test and control lines are not visible, it does not necessarily mean that an individual is negative for the target analyte, because the sample did not flow through the strip correctly. Accordingly, a positive result is indicated by two red bands, one at the test line and one at the control line, while a negative result corresponds to an absent test line and visible control line.

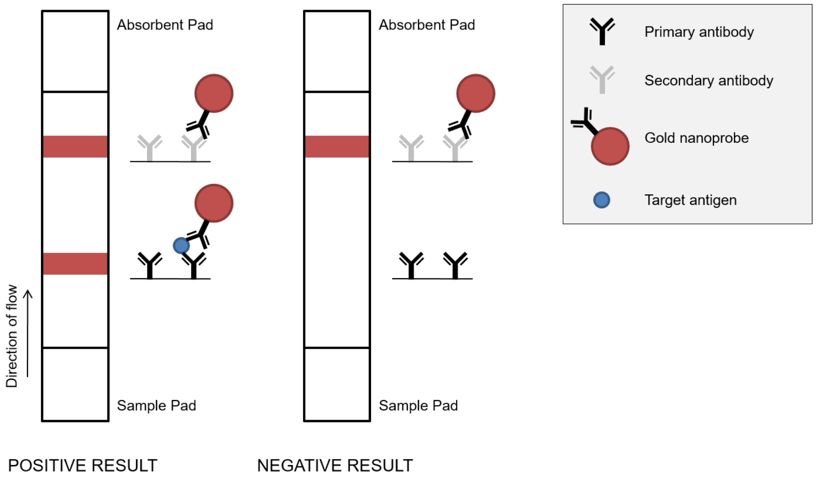

Figure 1-2 Schematic of positive and negative results for the sandwich LFA format. Positive test results in the formation of 2 visible bands while a negative test shows 1 visible band

The competitive assay is more suitable for the detection of smaller molecules with a single binding epitope, where it would not be possible for two antibodies to bind simultaneously. In the competitive assay format (**Figure 1-3**), the target analyte is immobilized on the nitrocellulose membrane to form the test line. The colorimetric indicator contains primary antibodies specific against the target analyte. If the target analyte is present in the sample solution, it will be captured by the primary antibodies on the colorimetric indicator. As the colorimetric indicator flows past the test line, it will not be able to bind to the analyte that is immobilized at the test line region because primary antibodies are already occupied with the analyte from in the sample solution. In the case of a negative test, where no analyte is present in the sample solution, the primary antibodies on the indicator are able to bind to the analyte immobilized at the test line. Excess gold indicator is captured further along the strip by secondary antibodies which form the control line. Thus, a positive result corresponds to just a visible band at the control line location, while a negative result corresponds to a visible band at both the test and control line locations.

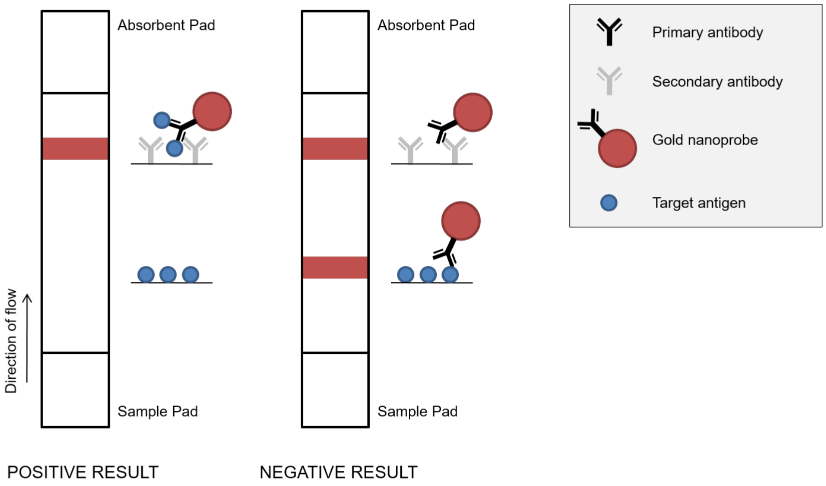

Figure 1-3 Schematic of positive and negative results for the competitive LFA format. Positive test results in the formation of 1 visible band while a negative test shows 2 visible bands

Several features that make the LFA an attractive option for a POC device include the ability to work with small sample volumes, requirement of minimal power, training, or equipment, and its ability to produce rapid results. However, the conventional LFA does suffer from a few disadvantages which limit its ability to fully replace sophisticated laboratory-based assays. For one, it only provides a qualitative "yes" or "no" answer, making it unsuitable for applications where accurate biomarker quantification is desired such as therapeutic drug monitoring or some environmental screening applications. The other major disadvantage of the conventional LFA is that it has a low sensitivity particularly when biomarkers are present at low concentrations, which is often the case for infectious diseases at their early stages of progression which is when we would like to detect them. Throughout this thesis, I will be discussing the development of cutting-edge technologies to address both the poor quantitative characteristics and low sensitivity of the LFA without the addition of complex electronics or equipment.

1.2. Overview of Quantitative LFA Readouts

A variety of different methods with varying levels of complexity have been developed to introduce a more quantitative readout to the LFA. These can largely be broken into two main categories: those that require electronic readers and those that do not. Electronic readout devices measure the LFA results through a variety of different signals, such as colorimetric,[7] fluorescent,[8] electrochemical,[9] magnetic,[10] and thermal.[11] While these devices are effective at providing a quantitative readout and lowering the detection limit of the LFA, they are not ideal for at-home screening or resource-limited settings where such a device may be cost prohibitive. There have also been efforts to couple the LFA with chemical reactions to produce a signal that could be measured by existing, more affordable, mass-produced electronic devices such as personal glucose meters[12] and handheld pressure meters.[13] While relatively affordable compared to a smartphone or benchtop reader, these methods are still not suitable for a single use, disposable test which is preferred for at-home screening.

The intensity-based method of quantitative LFA interpretation is perhaps the simplest technique to perform without any test strip modification or external devices. This method involves the user comparing the LFA test line intensity with a standard reference card that depicts the different signal intensities expected to be produced by different concentrations of analyte.[14] The matching intensity corresponds to the analyte concentration in the sample tested. One disadvantage of this technique is that it may be difficult to distinguish small intensity differences produced by small changes in analyte concentration. Additionally, LFA test lines are often relatively thin and produce an intensity gradient along the direction of flow, further making accurate intensity-based interpretation difficult.

Perhaps the most well-known approach to introducing a more quantitative readout to the LFA without introducing any additional components or user steps is the ladder-bar or barcode-style LFA.[15,16] The sandwich barcode-style LFA utilizes a test strip that has multiple different test lines printed on it, often with varying concentrations of antibody at each test line location.[17] Alternatively, different antibody species that are all specific to the same target analyte but with varying affinities can be printed on the different test lines. Each of these test lines will have a cut-off value, which is the minimum concentration of analyte in the sample necessary for that line to become visible. After testing a sample, the number of test lines that appear visible to the user can be correlated with a concentration range of the target analyte in that sample.

When designing a barcode-style LFA, there are a number of controllable factors that can affect the cut-off values. An increase in the concentration and/or affinity of the immobilized antibody will increase the amount of analyte that is captured, thus decreasing the cut-off value for that particular test line. Additionally, increasing the antibody concentration/affinity at an upstream test line will often increase the cutoff for a downstream test line. This is a result of that upstream test line capturing and depleting the sample solution of analyte to a greater degree and thus there is less remaining analyte to be captured at the downstream test lines. As a result, a greater concentration of analyte would be required for the downstream test lines to become visible. Weigl and coworkers developed a mathematical model that could predict the performance of the various barcode-style LFA setups in order to aid in assay design and optimization.[18] Through this work the authors found that by placing the lowest antibody concentration in the most upstream location, the depletion effect could be avoided and a broad logarithmic response to analyte concentration could be achieved, as opposed to the more narrow linear response that is observed when the depletion effects are present. While simple, affordable, and easy to use, the barcode-style LFA still has a limited quantitative resolution. The number of concentration ranges detectable is limited by the number of test lines that can be printed on the membrane. Therefore, the barcode-style LFA is suitable for applications where only a few, broad concentration ranges need to be distinguished but may not be applicable where more accurate analyte quantification is necessary.

More recently, Wang and coworkers developed a microfluidic chip that served as an "LFA ruler" for distance-based analyte quantification.[19] Antibody-conjugated platinum nanozymes were used as probes in the LFA. After running the sample through the test strip, the test line region was cut out and inserted into a sealed well in the LFA ruler. This well contained hydrogen peroxide, which was degraded into water and oxygen by the catalase-like activity of the platinum nanozymes, resulting in a buildup of pressure. This pressure build-up would then push a colored indicator dye through a microfluidic channel. The distance that the dye traveled was directly proportional to the analyte concentration in the original sample. Compared with the other techniques discussed above, this method has the potential to have greater quantitative resolution as well as a larger dynamic range, but does require microfluidic chip fabrication.

1.3. Introduction to Plasmonic Enzyme-Linked Immunosorbent Assay (pELISA)

1.3.1. Localized surface plasmon resonance

Metal nanoparticles have electromagnetic properties that differ significantly from bulk metals. In particular, they possess very unique optical properties.[20] When incident light interacts with metal nanoparticles, the electromagnetic field from the light induces a dipole in the nanoparticle. This dipole also results in coulombic repulsions which act as a restoring force where it pushes the free electrons to move in the opposite direction, thus generating a collective, coherent oscillation of electrons. These oscillations, called plasmons, are in resonance with the frequency of light. Overall this phenomenon, known as localized surface plasmon resonance (LSPR), results in the very strong absorption of light at these resonance frequencies by the nanoparticles.[21] By altering the size, shape, and material of the metal nanoparticles, as well as the dielectric properties of the surrounding medium, the absorbance properties can be controlled such that a variety of different colored nanoparticle suspensions can be produced.[22]

Cylindrical gold nanoparticles, also known as gold nanorods (GNRs), are particularly unique in that they possess two distinct plasmonic modes: the transverse mode, which results of the electron oscillation along the short axis of the GNRs, and the longitudinal mode oscillations which is due to electron oscillations along the longer axis of the GNRs (**Figure 1-4**).[23] By controlling the aspect ratio (length divided by the width) of the GNRs, the longitudinal mode can be tuned across the whole visible and near-infrared spectrum.[24] This makes it possible to synthesize nanorod suspensions with a wide range of optical properties and colors (**Figure 1-5**).[25] Due to their high molar extinction coefficients, tunable optical properties, ease of bioconjugation, and facile synthesis, plasmonic nanoparticles such as gold nanorods have found many useful applications as reporters in analytical assays.[26]

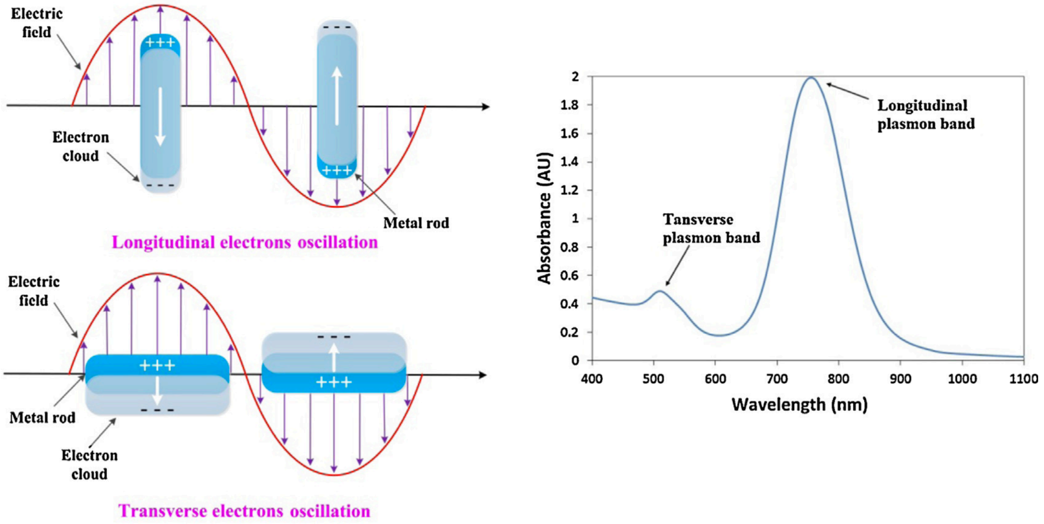

(A) (B)

Figure 1-4 Localized surface plasmon resonance excitation for gold nanorods
(A) Schematic representation of electron oscillation along the long (top) and short axis (bottom). (B) UV-Vis absorbance measurements of GNR suspensions showing LSPR plasmon bands associated with the transverse and longitudinal electron oscillations. Reproduced from ref. 23, with permission from Elsevier.

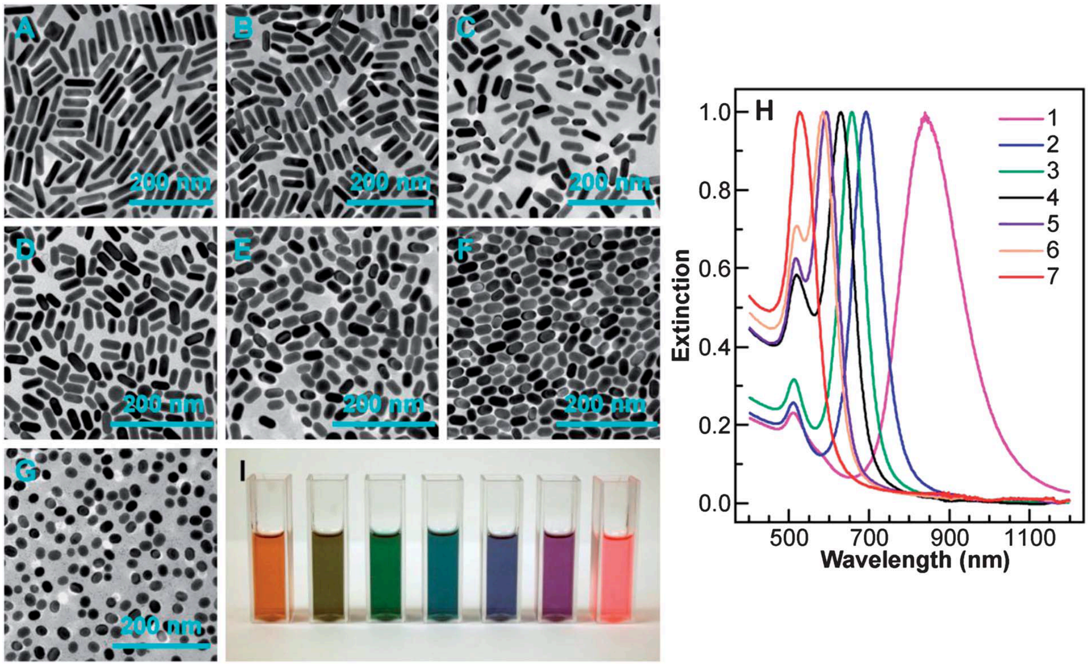

Figure 1-5 Gold nanorod suspension of varying aspect ratios
(A-G) TEM images of different sized gold nanorod suspensions (1-7), respectively. (H) UV-Vis absorbance measurements of gold nanorod suspensions. (I) Photograph of gold nanorod suspensions 1 to 7 from left to right. Reproduced from ref. 25, with permission from RSC Publishing.

1.3.2. Strategies for pELISA

As briefly mentioned in *Section 1.1.1*, the conventional enzyme-linked immunosorbent assay (ELISA) is not ideal for use in resource-limited settings due to its requirement of many user steps, a long time to result, and the requirement of expensive electronic equipment for analysis. Recently, researchers have been developing methods to produce quantitative and sensitive versions of the ELISA that do not require expensive plate readers for analysis, thereby improving its applicability to resource-limited settings. One area of research which looks to take advantage of the unique LSPR properties of metal nanoparticles is the development of the plasmonic ELISA (pELISA). In contrast to the conventional ELISA, where the signal is produced from the enzymatic catalysis of organic dyes or chromogenic substrates followed by intensity measurements with expensive well-plate readers, the pELISA utilizes an enzymatic reaction to tune the optical properties and thus visible color of a metal nanoparticle suspension as a function of the analyte concentration, which can then be easily interpreted by the naked-eye.[27] To date, there have been four main classes of plasmonic ELISA which are illustrated in **Figure 1-6**.

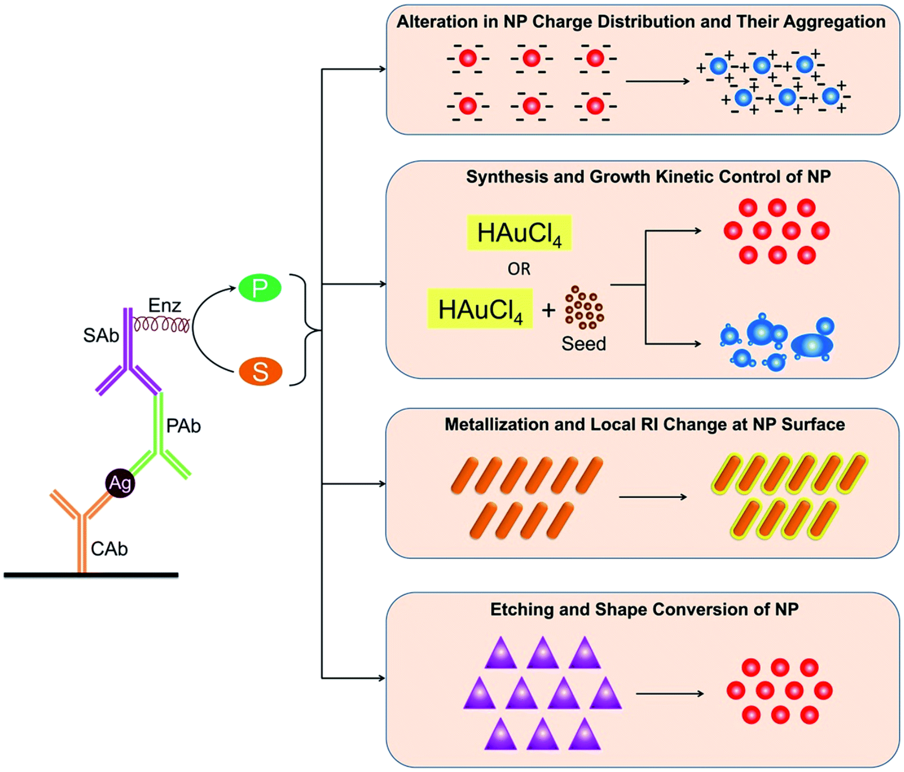

Figure 1-6 Schematic representation of the four main formats of plasmonic ELISA
Antigen (Ag) becomes sandwiched between the capture antibody (CAb) and primary antibody (PAb). Secondary antibody (SAb) labeled with enzyme (Enz) binds to primary antibody and will convert substrate (S) to product (P). Product or remaining substrate go on to alter nanoparticle (NP) plasmonic properties through one of four mechanisms: controlled aggregation, controlled synthesis and growth, metallization or change in local refractive index (RI), or etching and shape conversion. Reproduced from ref. 27, with permission from RSC Publishing.

The first strategy is based on tuning the attractive and repulsive forces between nanoparticles in suspension to control their aggregation. This aggregation can be controlled through a variety of different mechanism such as the enzymatic formation or degradation of a molecular compound which can bind to and thus bridge multiple nanoparticles,[28] or that can decrease the surface charge and thus electrostatic repulsive forces that stabilize the particles.[29] A decrease in the interparticle distance below the approximate nanoparticle diameter results in plasmon coupling which induces a red-shift in the LSPR wavelength.[30] When using gold nanoparticles, this results in a shift in suspension color from a red color to a blue color which can easily be interpreted by eye.[28]

The second strategy involves controlling the formation and growth kinetics of gold nanoparticles. Typical of gold nanoparticle synthesis, the mechanism involves a nucleation step, followed by a growth step.[31] First, a small metallic nuclei of a few atoms will form through the rapid reduction of gold ion precursors into a metallic state. This is followed by a growth step, where either gold ions are reduced and further deposited onto the surface of the nuclei, or nuclei aggregate to form larger particles. This whole process is very sensitive to the solution and reaction conditions (*i.e.* pH, ionic strength, and temperature), such that small changes in reaction parameters can significantly affect the resulting nanoparticle morphology and thus LSPR properties. Researchers de la Rica and Stevens took advantage of this by coupling an immunoassay-linked catalase reaction that degraded the hydrogen peroxide as a function of the analyte concentration in the original sample with a synthesis reaction of gold nanoparticles that utilized hydrogen peroxide as a reducing agent.[32] This allowed the synthesis of gold nanoparticles with different morphologies, depending on the initial concentration of analyte, ultimately producing red or blue color suspensions for the ultrasensitive detection of HIV-1 capsid antigen p24 and prostate specific antigen. Similar mechanisms have also been implemented for controlling the synthesis of silver nanoparticles[33,34] and GNRs with different aspect ratios.[35]

The third major category of pELISA involves the metallization of existing nanoparticles to produce core-shell nanostructures. The deposition of a thin metallic shell of different composition as the original nanoparticle can cause a shift in the LSPR absorption peak of that nanoparticle. This can result in a visible change in color hue. One reported mechanism involves the use of an immunoassay-linked alkaline phosphatase reaction to dephosphorylate *p*-aminophenol phosphate into 4-aminophenol, which then continues to reduce silver ions onto the surface of GNRs.[36] Depending on the concentration of prostate-specific antigen in the sample being tested, different amounts of *p*-aminophenol would be generated which result in different thicknesses of the silver shell being deposited onto the GNRs, thus producing distinct colored suspensions (from pink to orange to green to grey to red). Similar techniques have also been developed to deposit silver shells onto spherical gold nanoparticles, gold nanostars,[37] and gold nanobipyramids.[38]

The fourth strategy involves the controlled oxidative etching of anisotropic metal nanoparticles. Anisotropic nanoparticles often have regions of high curvature and/or sharp tips, which have high surface energies and lower protective ligand (often some type of surfactant) surface coverage. Upon the addition of an oxidizing agent to these nanoparticles, etching of surface atoms will selectively occur at these regions of greater surface energy, resulting in a predictable and reproducible shape conversion of these nanoparticles. The resulting change in size and shape will significantly alter the LSPR properties and thus the visible color produced by these particles. This strategy of etching pre-existing nanoparticles is advantageous compared to the other three strategies because it is less sensitive to environmental factors and contaminants that could affect *in situ* synthesis of nanoparticles, growth of thin metal shells, or controlled nanoparticle aggregation.

1.3.3. *Mechanism of oxidative etching of gold nanorods (GNRs)*

The advantages of nanoparticle etching and shape control led us to look further into the integration of the ELISA with the hydrogen peroxide-mediated oxidative etching of gold nanorods for the production of a multicolor, naked-eye readout. Aqueous solutions of hydrogen peroxide have previously been reported to be able to oxidize GNRs in the presence of cetyl trimethyl ammonium bromide (CTAB).[24,39,40] The dissolution mechanism of a solid gold plate by bromine in the presence of hydrogen peroxide was first reported by Pesic and Sergent.[41] Here, the hydrogen peroxide oxidizes bromide ions to form diatomic bromine in a highly acidic environment. The diatomic bromine will react with any excess bromide ions to form tribromide. The tribromide is a very reactive species that can oxidize Au(0) from a solid gold plate to produce Au(I) in the soluble form of $AuBr_2^-$, thus dissolving the gold plate.

This mechanism was extended by Ni and coworkers to explain the role of bromide in the peroxide-mediated etching of CTAB-stabilized GNRs.[42] It was demonstrated that tribromide was also responsible for the dissolution of Au(I) from the surface of GNRs resulting in the etching of the GNRs. The role of CTAB beyond a bromide ion donor was also thoroughly investigated in this study. It was proposed that CTA^+ serves a unique role in aiding the etching of GNRs, where it (1) enhances the solubility of diatomic bromine as the nonpolar diatomic bromine can associate with the hydrophobic tails of the micelles, (2) stabilizes tribromide through strong electrostatic interactions, and (3) improves accessibility of the tribromide to the surface of the GNRs by facilitating transport through the dynamic exchange of $Br_3^- - CTA^+$ complexes with the stabilizing CTA^+ bilayer around the GNRs. While CTA^+ is important for stabilizing the GNRs and tribromide, it was also found that increasing CTA^+ slowed the production of tribromide by strongly complexing with the bromide ions prior to formation of tribromide. Therefore, for efficient GNR etching, bromide ions should be kept in excess to CTA^+.

When reacting with peroxide and CTAB, GNRs are selectively etched from their tips, which are regions of high curvature, and thus are shortened. This directionality is due to the arrangement of the CTAB bilayer, where the CTAB is tightly packed along the longer face, and more loosely packed around the highly curved tips. Therefore, the repulsive, electrostatic interactions between the CTA+ bilayer on the GNRs and the CTA+ micelles with bound Br_3^- is weaker at the tips compared to the long axis of the GNR. This results in the dynamic exchange of surfactants occurring preferentially from the nanorod tips, and thus that is where the tribromide is delivered to react with the GNRs.[43]

1.3.4. pELISA using GNR etching mechanism

While hydrogen peroxide has been shown to etch GNRs in the presence of bromide, it typically requires high concentrations of hydrogen peroxide, highly acidic conditions, and/or high temperature and/or long reaction times.[24,39,40] Guo and coworkers developed a method to speed up this peroxide-mediated etching of GNRs at room temperature through the use of Fenton's reaction in order to produce colors across the whole visible spectrum in just 15 min which is a suitable time span for use in a point-of-care test.[44] Then this reaction was coupled with a competitive ELISA for the naked-eye, quantitative detection of aflatoxin B1 (AFB1). The reaction scheme for which is shown in **Figure 1-7A**.

First, a sample with some unknown amount of AFB1 is mixed with an AFB1-catalase conjugate and incubated in a well plate with immobilized anti-AFB1 antibodies. The AFB1-catalase conjugate competes with the free AFB1 for binding to the immobilized antibody. A low concentration of free AFB1 in the sample would result in a large amount of AFB1-catalase being captured on the antibodies, whereas a high concentration of free AFB1 would result in a low amount of AFB1-catalase being captured. After several washing steps, a solution of hydrogen peroxide is added into the well. Any bound catalase enzymes would degrade the hydrogen peroxide into water and oxygen. Different amounts of catalase bound to the well plate would then result in different concentrations of hydrogen peroxide remaining after this degradation step. Finally, GNRs and Fe^{2+} are introduced, where the Fe^{2+} would break down the remaining hydrogen peroxide to produce hydroxy radicals which then go on to induce the oxidative etching of GNRs. Low initial concentrations of free AFB1 would result in a small amount of GNR etching, while high concentrations of free AFB1 would result in significant GNR etching. Ultimately depending on the concentration of AFB1, a wide range of distinguishable colors were produced, which cover the whole visible spectrum from 400 to 760 nm (**Figure 1-7B**). It is also worth noting that very small changes in the concentration of AFB1 resulted in significantly color changes that could be easily interpreted by the naked-eye. Gold nanorod etching has been integrated with the ELISA and for other applications for quantitative, multicolor analyte detection.[45–47]

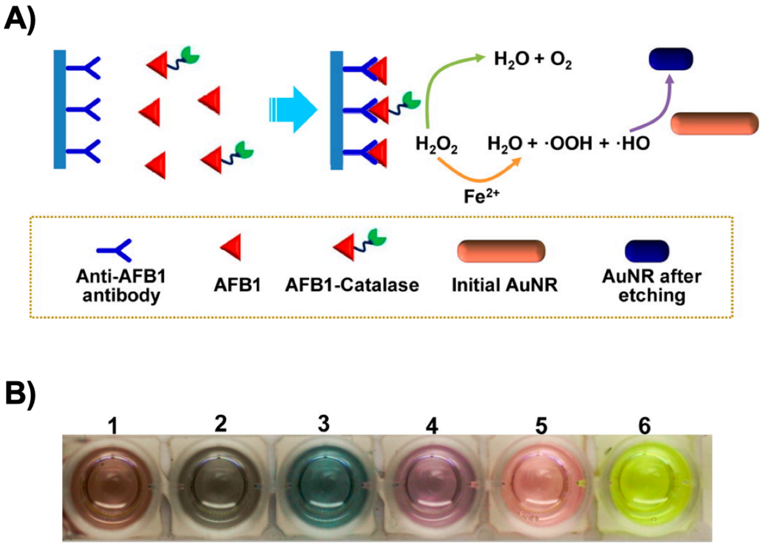

Figure 1-7 Schematic and quantification of Alfatoxin B1 with gold nanorod etching-based pELISA. (A) Alfatoxin B1 (AFB1) in sample competes with AFB1-catalase for binding to immobilized anti-AFB1. Following washing steps, hydrogen peroxide was introduced which was degraded by bound catalase. Gold nanorods and Fe^{2+} were then introduced to initiate nanorod etching and multicolor signal production. (B) Multicolor signal produced from AFB1 concentrations of 0.06, 0.12, 0.18, 0.24, 0.30, and 0.40 ng/mL, indicated by sample numbers 1 through 6. Reproduced from ref. 44, with permission from ACS.

1.4. Overview of Aqueous Two-Phase Systems (ATPSs)

Aqueous two-phase systems (ATPSs) are liquid-liquid extraction systems that have typically been used for the separation and purification of cells, viruses, organelles, proteins, nucleic acids, and other biomolecules. Because both phases consist primarily of water, ATPSs are advantageous over traditional oil-water extraction systems for the purification of biomolecules, since oil phases can denature biomolecules. Liquid-liquid extraction techniques in general have the advantage of being scalable; while they have traditionally been used for large-scale purification in the biotechnology and pharmaceutical industries, our lab has scaled the ATPS down to less than 1 g for their use in small-scale diagnostic applications.[48,49]

Three of the most common types of ATPSs are polymer-polymer, polymer-salt, and micellar systems. One common polymer-salt ATPS that our lab has utilized in the past is composed of polyethylene glycol (PEG) and potassium phosphate salt. In the PEG-potassium phosphate salt ATPS, phase separation occurs when the concentrations of PEG and salt exceed a certain critical value. Mechanistically, PEG molecules are normally surrounded by water molecules due to hydrogen bonding with the oxygen present in its repeating chain. Upon the addition of the potassium phosphate salt, these hydrogen bonds are disrupted by the electric field emanating from the salt ions, resulting in the water molecules being drawn away from PEG.[50,51] As the water is pulled away from the PEG molecules, nearby PEG molecules can approach one another more closely and experience increased attractive van der Waals interactions. The interactions between PEG molecules becomes more favorable, while the interactions between the water and PEG becomes less favorable. This results in the formation of microscopic PEG-rich domains that coexist with microscopic salt-rich domains. Due to the interfacial tension between these domains, they will coalesce over time in order to decrease the overall interfacial energy of the system. As they coalesce and grow in size, they will migrate depending on their relative densities, where the denser salt-rich domains will form a macroscopic bottom salt-rich phase, and the less dense PEG-rich domains will form a macroscopic top PEG-rich phase.

Phase separation of aqueous two-phase systems occurs only under certain conditions which can be mapped out and described using a phase diagram. An example phase diagram for a typical polymer-salt ATPS is displayed in **Figure 1-8**. The binodal curve (also called the coexistence curve) separates the one phase region from the two phase region.[52] Concentrations of polymer and salt above the binodal curve will give rise to phase separation, while those below it will remain a homogeneous, single-phase solution. The composition represented by point A will phase separate, where the equilibrium compositions of the resulting polymer-rich and salt-rich phases are represented by points B and C, respectively. B_P represents the polymer concentration and B_S

represents salt concentration in the polymer-rich phase, while C_P represents the polymer concentration and C_S represents salt concentration in the salt-rich phase for the ATPS with an initial composition represented by point A. Pairs of points such as B and C which represent the composition of the separated phases are called nodes, and the line connecting them which passes through point A is called a tie line. All initial compositions which lie on the same tie line will result in equilibrium phases of the same composition represented by B and C, but with different volumes of the respective phases. The ratio of the lengths of line segments AC to AB describe the mass ratio of the polymer-rich phase to salt-rich phase for the system with an initial composition represented by point A, which is approximately a 1:1 mass ratio. In the case of an initial composition represented by point D, the ratio of line segments DC to DB describe the mass ratio of the polymer-rich phase to salt-rich phase for the system, which is approximately a 3:1 mass ratio. In the case of many polymer-polymer or micellar ATPSs, the densities of the two equilibrium phases are often roughly equal so the mass ratio can often be simplified to the volume ratio. For most polymer-salt systems however, the salt-rich phase is significantly denser than the polymer-rich phase so this simplification cannot be made and the density must be considered to accurately calculate the ATPS volume ratio from the phase diagram. By altering the initial composition while changing tie lines, such as going from point A to A', it is possible to change the composition of the equilibrium phases, from B and C, to B' and C', while maintaining the same 1:1 mass ratio. Phase diagrams are often determined experimentally using the cloud point method,[53] however they can also be predicted using thermodynamic modeling.[54]

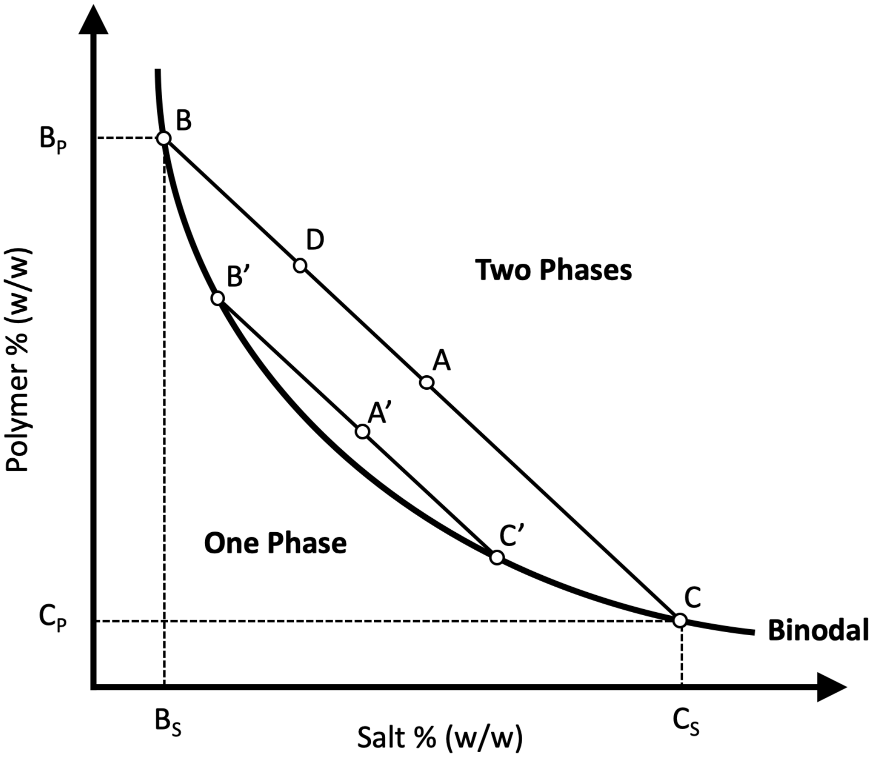

Figure 1-8 A general phase diagram for a polymer-salt ATPS system.
Points A and A' represent initial compositions that will yield two-phase systems with equal volume polymer-rich and salt-rich phases on different tie lines. The pairs of points B and C, as well as B' and C', are nodes, representing the equilibrium concentrations of phase forming components in the polymer-rich and salt-rich phases, respectively, for the different tie lines. Point D represents a two-phase system on the same tie line as point A but with a larger polymer-rich (top) phase volume relative to the salt-rich (bottom) phase volume.

1.5. Integration of ATPSs with Rapid Diagnostic Tests

Our research group was the first, and to our knowledge, still remains the only group to combine ATPSs with the LFA to improve biomarker detection by concentrating the biomarkers into one of the two phases of an ATPS.[48,49,55–59] Our methodology provides an unconventional yet simple approach as much of the work in paper-based diagnostics has focused on improving antibody affinity and creating channels in paper to resemble microfluidics. Our approach is also unique because ATPSs have been more commonly used in the biotechnology industry for large-scale purification of proteins and not for small-scale applications.

Initial proof-of-concept studies involved improving the LFA detection limit for the model virus bacteriophage M13 and the model protein transferrin using the Triton X-114 micellar ATPS.[55,56] Using the Triton X-114 micellar ATPS, the detection limits of bacteriophage M13 and transferrin were improved by 10-fold. In separate studies, the polyethylene glycol (PEG)-salt system was also investigated and successfully resulted in a 10-fold improvements in detection limits for bacteriophage M13 and transferrin.[57,58] With regard to the bacteriophage M13, a large model virus, it partitioned extremely into the micelle-poor/ PEG-poor phase due to experiencing greater steric, excluded-volume interactions with the greater number of micelles/PEG polymers in the micelle-rich/PEG-rich phase. The model hydrophilic protein transferrin partitioned rather evenly between the two phases of the ATPS, due to its small size, resulting in a poor concentrating ability on its own. In order to enhance the ability of the ATPS to concentrate proteins, antibody-conjugated gold nanoprobes (GNPs) were utilized, which captured the target protein, drove them into the desired micelle-poor (PEG-poor) phase for concentration, and simultaneously served as a colorimetric indicator for LFA. Due to the repulsive, steric, excluded-volume interactions experienced by the large GNP-transferrin complexes, they were excluded from the micelle-rich/PEG-rich phase and partitioned extremely to the micelle-poor/PEG-poor phase. By altering the ATPS composition, the volume ratio (volume of top phase divided by the volume of the bottom phase) could be controlled (**Figure 1-9**).[48] By using a volume ratio of 1:9 for the Triton X-114 ATPS or 9:1 for a PEG-salt ATPS, the biomarker could be forced into 1/10th the original volume of the ATPS solution, effectively concentrating it by 10-fold, resulting in the observed 10-fold improvements in LFA detection limit.

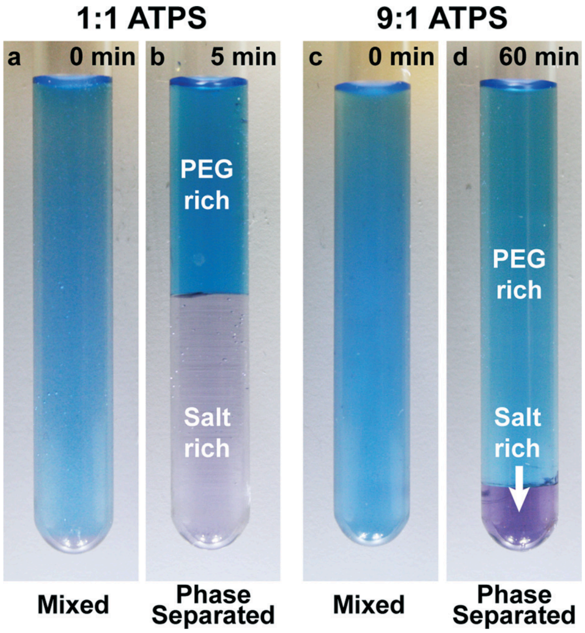

Figure 1-9 PEG-Salt aqueous two-phase systems with volume ratios of 1:1 and 9:1. Brilliant Blue FCF dye and gold nanoparticles, which serve as colorimetric indicators, partition extremely into the top PEG-rich and bottom salt-rich phases, respectively. (a) The mixed 1:1 volume ratio ATPS separated to form (b) two equal phases. (d) The mixed 9:1 volume ratio ATPS separated to form (d) a larger top PEG-rich phase and a smaller, bottom PEG-poor phase. Because the same amount of dye and gold nanoparticles was added to each system, the darker purple color of the 9:1 salt-rich phase is due to the gold nanoparticles being concentrated in the much smaller volume compared to the 1:1 ATPS. Reproduced from ref. 48, with permission from RSC Publishing.

In addition, our group demonstrated that adding an ATPS directly onto a paper membrane can greatly enhance and accelerate the phase separation process. This discovery allowed for the seamless incorporation of the concentration and detection steps into one fully-integrated paper-based device.[48] Although this phenomenon has not been fully elucidated, it is hypothesized that size-exclusion effects due to the pores of the membranes, the influence of viscosity on fluid flow, and favorable interactions with the porous paper material, all features that do not take effect in the traditional test tube, allow for the enhanced separation of the two phases within the paper membrane. This device demonstrated similar improvements in detection when compared to previous studies involving extracting a phase from the ATPS and applying it to LFA, but the fully-integrated device was more rapid and also reduced user interaction by eliminating the time required for phase separation to occur in a tube as well as the phase extraction step. In order to further enhance this concentration in paper phenomenon, a 3D well was added (**Figure 1-10A**). The improvement in the phase separation process when using the 3D paper well can be explained by the following: the greater cross-sectional area normal to the direction of flow allows (1) the less viscous salt-rich domains to more easily coalesce and become the concentrated leading phase, (2) more interactions between the paper and PEG-rich phase, where the PEG-rich phase is retained longer within the 3-D well, and (3) more volume of sample to wick through the paper at the same time. A detection step can be seamlessly incorporated by applying a 3D well directly upstream from a traditional LFA strip, which will allow for the simultaneous concentration and detection of biomarkers (**Figure 1-10B**). A 10-fold improvement in the detection limit of transferrin was achieved using the ATPS and 3D paper architecture.[48] The Triton X-114 ATPS was also integrated with 3D paper architecture and the LFA test strip, resulting in a 10-fold improvement in detection limit for plasmodium lactate dehydrogenase in fetal bovine serum.[49]

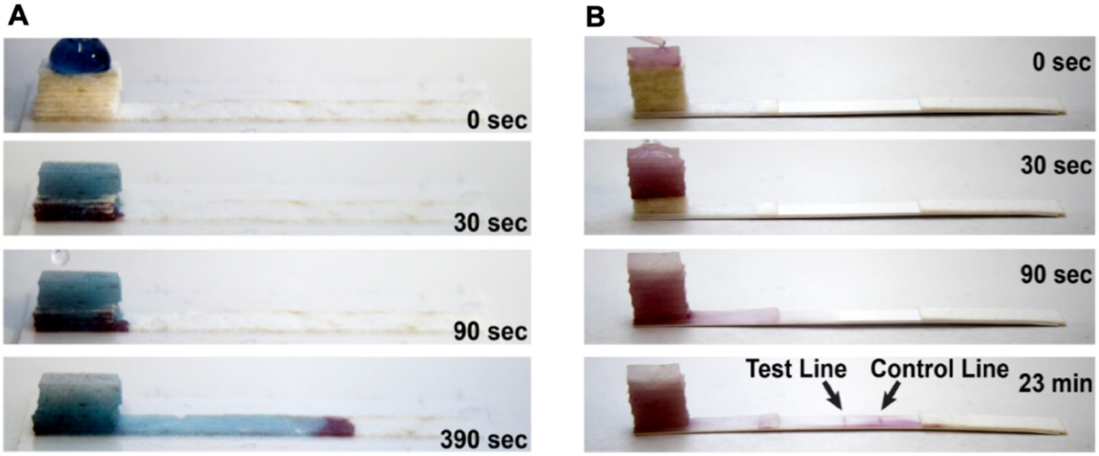

Figure 1-10 Two phase separation on paper and integration with the lateral-flow immunoassay
(A) The 3D paper well improved macroscopic phase separation and enabled separation of a 9:1 ATPS to occur in under 4 min. (B) The integrated ATPS + LFA consisted of the 3D paper well and LFA test strip. Target biomolecule transferrin was captured by gold nanoparticles and concentrated in the leading front allowing seamless transition into the LFA for 10-fold improved detection. Reproduced from ref. 48, with permission from RSC Publishing.

1.6. Overview of Signal Enhancement Methods

1.6.1. Review of readouts and reactions for enhancing LFA signal enhancement

Besides biomarker preconcentration, many researchers have attempted to improve the detection limit of the LFA through signal enhancement. LFA signal enhancement techniques tend to fall in two categories: those using electronic readout devices, and the application of novel particles or color-producing reactions with improved visible signal. The same electronic readout devices mentioned in *Section 1.2* which provide quantitative measurements can be used to improve the detection limit of the LFA, but they can be cost prohibitive for at-home screening or use in resource-limited settings.

Techniques that focus on improving the visible output of the LFA in a way that can be interpreted by the naked-eye are ideal for POC devices that may be used in resource-limited settings. One general approach involves the development of novel plasmonic nanoparticle labels which exhibit higher extinction coefficients than the typical spherical gold nanoparticles that are used on the LFA. Some examples include the use of flower-like and popcorn-like gold nanoparticles,[60] dual-gold nanoparticles[61], and gold-decorated silica nanorods[62]. The application of color producing reactions to the LFA often revolves around methods analogous to the ELISA. The ELISA is a sensitive, laboratory-based immunoassay that utilizes antibodies to capture a target biomarker, and enzymes (e.g., horseradish peroxidase or alkaline phosphatase) to convert substrates into colored or fluorescent products. As an example of integrating color producing reactions with the LFA, a sample solution can be applied to an LFA strip that contains gold nanoparticles conjugated with primary antibodies and enzymes. After a certain period of time, a substrate solution can be applied to the LFA strip, initiating an enzymatic reaction that produces a dark colored precipitate that deposits on the test and control lines, thereby enhancing the visible signal. A variety of different reactions have been incorporated into paper-based diagnostics such as the LFA which use this multistep procedure including enzyme-based,[63] nanozyme-based,[64,65] gold and silver enhancement[66], and polymerization-based reactions.[67]

1.6.2. Automation of signal enhancement on paper-based devices

While these signal enhancement reactions have proved effective at improving the LFA detection limit, they typically require multiple user steps, making them not ideal for a POC setting.[63,68] To eliminate the need for multiple user steps, the Yager group has developed 2D paper networks (2DPNs) to control fluid flow and perform timed delivery of reagents to a detection zone with minimal user intervention. While successful at automating gold enhancement and enzymatic enhancement reactions, 2DPNs have thus far demonstrated limited improvements in detection limit over their unenhanced counterparts.[69,70] Additionally, 2DPNs are geometrically more complex than the conventional LFA test strip, which could increase cost and limit their adaptability for high volume manufacturing.[71]

1.7. Concluding Remarks and Thesis Overview

While many rapid diagnostic tests utilizing the LFA format have be successfully been developed and brought to market, many exhibit poor analytical performance (low sensitivity and specificity). Those that utilize technological developments for improving sensitivity and quantitative capabilities beyond what the conventional test strip can achieve rely heavily on electronic readers which may not be suitable for resource-limited settings. Therefore, this thesis aims to develop new technologies that improve the performance of the LFA without the need for electronic readers. In Chapter 2 we describe the development of a barcode-style LFA for the semi-quantitative detection of beta-trace protein used to detect for cerebrospinal fluid leaks. It is a version of A.E. Kita, D.W. Bradbury, Z.D Taylor, D.T Kamei, and M.A. St. John, *Point-of-care cerebrospinal fluid detection.* Otolaryngology Head and Neck Surgery, 2018. In Chapter 3, the first standalone rapid diagnostic test kit for the detection of cerebrospinal fluid leaks was assembled, utilizing the barcode-style LFA developed in Chapter 2, which demonstrated excellent sensitivity and specificity when tested with clinical cerebrospinal fluid leak samples. It is a version of D.W. Bradbury, A.E. Kita, K. Hirota, M.A. St. John, and D.T Kamei. *Rapid diagnostic test kit for point-of-care cerebrospinal fluid leak detection.* SLAS Technology: Translating Life Sciences, 2019. To improve the quantitative capabilities of the LFA beyond what the barcode-style LFA could achieve, and without the need for electronic readers we then developed a new technique which integrated the LFA with the anisotropic etching of gold nanorods. This work, described in Chapter 4, allowed for the naked-eye multicolor quantification of the cardiac glycoside digoxin for therapeutic drug monitoring.

We then shifted to the development of technologies to improve the analytical sensitivity and detect limit of the LFA. Our lab previously discovered that ATPSs can rapidly separate into their bulk phases as the flow though paper, which allowed seamless concentration and detection of biomarkers on the LFA. In Chapter 5, we describe our efforts in expanding upon this work and improving the detect limit beyond the 10-fold improvements previously achieved. Specifically, we extended the functionality of an ATPS separating on paper to automate the sequential delivery of nanozyme signal enhancement reagents in addition to concentrating biomarkers which resulted in up to a 30-fold improvement in detection limit. It is a version of D.W. Bradbury, M. Azimi, A.J. Diaz, A.A. Pan, C.H. Falktoft, B.M. Wu, and D.T. Kamei. *Automation of biomarker* *preconcentration, capture, and nanozyme signal enhancement on paper-based devices*. Analytical Chemistry, 2019.

In late 2019, a new virus known as SARS-CoV-2 began to sweep across the globe, leading to the COVID-19 pandemic. The development of highly sensitive and easily deployable rapid diagnostic tests is a vital aspect of managing this pandemic. In Chapter 6, we discuss ongoing efforts to develop a highly sensitive, nanozyme signal enhanced LFA for the rapid detection of the SARS-CoV-2 nucleocapsid protein. A 3D printed casing was designed to store the test strip and all reagents in a way that maintains user friendly operation by eliminating liquid handling steps. The work described in Chapter 7 highlights the integration of novel fibronectin-based antibody mimetics, called monobodies, into the LFA for the detection of the nucleocapsid protein of SARS-CoV-2. These monobodies have the potential to be advantageous over monoclonal antibodies in that they are quick to develop using an mRNA display method, and are produced recombinantly in *Escherichia coli* which is more affordable and scalable when compared with hybridoma antibody production.

Chapter 2. Point-of-Care Cerebrospinal Fluid Detection

2.1. Introduction

A communication between the fluid surrounding the brain and the outside world, also known as a cerebrospinal fluid or CSF leak, is a known complication of numerous procedures in Otolaryngology. The risk in endoscopic skull base surgery has been estimated at 13.8%, in endoscopic sinus surgery at 0.17%, and in cochlear implantation at 0.4%.[72–74] Almost all procedures involving the sinuses, skull base, or ear have some risk of a leak. Individuals who have not undergone procedures are at risk as well. Trauma patients may have leaks from facial and skull base fractures, while some individuals are even unfortunate enough to present with rare spontaneous conditions such as middle cranial fossa CSF otorrhea.[75]

In the acute setting, imaging modalities such as magnetic resonance imaging or computed tomography are used for assessment. If there is high enough clinical suspicion (obvious facial or skeletal deformities or copious clear rhinorrhea or otorrhea), patients may be taken directly to the operating room for management. This involves identifying the site of the leak and using either native tissue or biocompatible materials to patch the affected site.

Identifying a CSF leak in the outpatient or postoperative hospital setting is often more difficult. It is not unusual for postoperative patients to have secretions, and therefore, distinguishing normal secretions from those containing CSF may be a challenging task. When physicians are concerned about a CSF leak, no proven diagnostic modalities exist that allow them to rapidly and non-invasively rule out the presence of a leak. Physicians must then turn to the same imaging techniques that are used in more acute settings, the cost of which may be difficult to justify in a patient who seems otherwise well. Alternative methods of identifying CSF have been developed. The current laboratory gold standard for CSF detection involves identification of beta-

2 transferrin through either electrophoresis or the enzyme-linked immunosorbent assay. These tests are 94-100% sensitive and 98-100% specific in detecting CSF; however, they typically require samples to be sent off to a central laboratory where days to weeks pass before results return.[76] Despite the promising role of beta-2 transferrin testing in published guidelines, this test is often not useful to guide clinical decision making due to the time it takes for results to return. Other methods of CSF detection have been explored. These include glucose testing, cisternography, and spotting the CSF to look for a "halo" or "ring" sign. Unfortunately, literature has not found these methods to be sensitive or specific.[77] As an alternative, researchers have looked at beta-trace protein (βTP) also known as prostaglandin D2 synthase lipocalin-type. βTP is a ubiquitous protein present at various concentrations in different body compartments, but notably one to two orders of magnitude higher in CSF than in nasal secretions and serum (**Table 2-1**).

Table 2-1 Mean concentrations of βTP found in various bodily fluids as reported in the literature

	Nasal Secretion (mg/L)	**Serum (mg/L)**	**Lumbar CSF (mg/L)**	**Proposed Cut-off (mg/L)**
Arrer et al.[78]	0.39	0.59	19.6	1.31
Reiber et al.[79]	0.016	0.59	18.4	0.35[a]
Schabel et al.[80]	< 0.25		16.3	1

Abbreviation: CSF, cerebrospinal fluid
[a] If nasal secretion sample contains blood, use 1 mg/L instead of 0.35 mg/L.

As a result, studies have demonstrated that nasal secretions with βTP concentrations measured above a certain threshold are suggestive of a CSF leak and need immediate operative intervention.[78–82] In a recent study by Bernasconi and coworkers using the nephelometric assay, it was determined that concentrations of βTP ≥1.3 mg/L indicate the presence of a CSF leak, whereas concentrations of βTP <0.7 mg/L indicate the absence of a CSF leak. βTP concentrations between 0.7 and 1.29 mg/L (denoted the "gray zone") required further analysis and comparison with the patient's βTP serum level to confirm the presence or absence of a CSF leak. This approach showed a sensitivity and specificity of 98.3% and 96%, respectively.[83] While the nephelometric assay is more rapid than electrophoresis, it still requires centralized laboratory equipment that may not be available in every clinical setting. To address this issue, here we describe the development of a semi-quantitative, barcode-style lateral-flow immunoassay (LFA) for the detection of βTP. By classifying a sample as having a concentration of either <0.7, between 0.7 and 1.29, or ≥1.3 mg/L βTP, we predict that our equipment-free and disposable device, will allow clinicians to more rapidly and affordably identify the presence of a CSF leak.

2.2. Materials and Methods

2.2.1. Preparation of the barcode-style lateral-flow immunoassay (LFA)

All reagents and materials were purchased from Sigma-Aldrich (St. Louis, MO) unless noted otherwise. First, to form antibody functionalized gold nanoprobes (GNPs), 35 μL of a 0.1 M sodium borate (pH 9) solution was added to 1 mL of a 40 nm citrate-capped gold nanoparticle suspension (Nanocomposix, San Diego, CA). Subsequently, 8 μg of anti-βTP antibodies were added and the mixture was allowed to react for 30 min. To prevent nonspecific binding of other proteins to the gold nanoparticles, 100 μL of a 10% w/v bovine serum albumin (BSA) solution was added to the mixture and allowed to react for 10 min. To purify unbound antibodies from the nanoparticles, the mixture was centrifuged three times at 9000 RCF for 6 min with the resulting pellets of the first two cycles being resuspended in 200 µL of 1% BSA in filtered ultrapure water and the final pellet resuspended in 100 µL of a 0.1 M sodium borate (pH 9) solution.

The LFA test strip is composed of overlapping pads secured to an adhesive backing (**Figure 2-1**). These pads include a sample pad, a conjugate pad, a nitrocellulose membrane, and an absorbent pad. The sample pad consists of a 3 x 10 mm fiberglass paper treated with a 0.1 M Tris (pH 9) solution containing 1% BSA. GNPs were dehydrated onto a 3 x 10 mm fiberglass paper along with 1% BSA in diH_2O to form the conjugate pad. Both the sample and conjugate pads were dehydrated under very low pressure using a Labconco FreeZone 4.5 lyophilizer (Fisher Scientific, Hampton, NH) for 2 h.

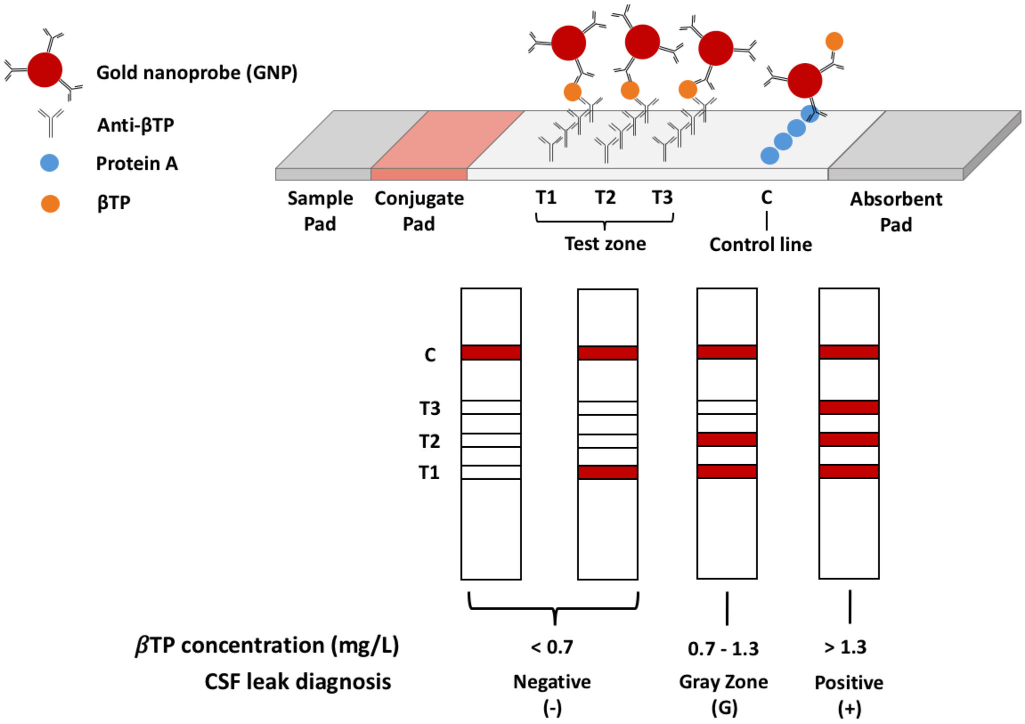

Figure 2-1 Schematic representation of our barcode-style lateral-flow immunoassay for the detection of beta-trace protein (βTP) and cerebrospinal fluid (CSF) leaks.

Anti-βTP antibodies were printed and immobilized on a nitrocellulose membrane at three different test line locations (T1, T2, and T3) to form the test zone. The antibodies at the T1, T2, and T3 locations were immobilized at 2, 0.5, and 0.35 mg/mL, respectively. These concentrations were experimentally determined to give the desired detection cutoffs. Protein A was immobilized at a concentration of 0.2 mg/mL on the nitrocellulose membrane downstream of the test zone to form the control line. Test and control line printing was performed using an Automated Lateral Flow Reagent Dispenser (Claremont BioSolutions, Upland, CA) and a Fusion 200 syringe pump (Chemyx, Stafford, TX) with a flow rate of 250 μL/min. The printed membrane was left in a vacuum-sealed desiccation chamber overnight. After protein immobilization, membranes were immersed in a 0.1 M Tris (pH 9) solution containing 1% BSA for 1 h and dehydrated under very low pressure overnight using a lyophilizer.

To assemble the test strip, the absorbent pad was first adhered at the far end of the test strip, downstream of the control line, overlapping the nitrocellulose membrane. The conjugate pad was placed at the opposite end of the strip, upstream of the test zone, overlapping the nitrocellulose membrane. Lastly, the sample pad was placed on the test strip overlapping the conjugate pad. After assembly, the LFA strips were placed in bags containing drierite desiccant (Fisher Scientific, Hampton, NH), which were then placed inside an auto-desiccant chamber (Fisher Scientific, Hampton, NH) for storage.

2.2.2. Detection of βTP with the barcode-style LFA

To demonstrate the ability of the barcode-style LFA to detect and quantify βTP, we tested it with a variety of samples including recombinant βTP (Mybiosource, San Diego, CA), human serum, and human CSF mixed with human serum. These samples were first diluted in various amounts in phosphate-buffered saline (PBS) in order to adjust the βTP concentration to find the optimal detection range of the barcode-style LFA. Briefly, samples containing known concentrations of recombinant βTP in PBS (0.3-90 mg/L) were diluted 150-fold in PBS. Pooled human serum (Sigma-Aldrich, St. Louis, MO), which served as human βTP-containing samples that were negative for CSF, were diluted by 50-, 150-, and 500-fold in PBS. Lastly, varying dilutions of CSF in human serum (2-fold, 5-fold, 10-fold), which served to simulate nasal drip samples that contain varying amounts of CSF, were diluted by 150-fold in PBS.

Prior to running the assay, the above PBS-diluted samples were further diluted by 2-fold by mixing 25 μL of the samples with 25 μL of running buffer (0.4% BSA, 0.6% Tween 20, 0.2% polyethylene glycol, 0.1 M Tris buffer, pH 9) in a test tube. The LFA test strip was dipped vertically into the tube with the sample pad submerged. After 20 min, the test strips were imaged by a Canon EOS 1000D camera (Canon U.S.A., Inc., Lake Success, NY) in a controlled lighting environment. Three different CSF samples were tested with our assay. Representative images from one of these samples are shown.

2.3. Results

In our barcode-style LFA, the presence of the target biomarker would produce one to three visible test lines as the GNPs would first bind to the βTP in the sample and then be captured at the test lines (**Figure 2-1**). Each test line has a cut-off, which is the minimum concentration of βTP in the sample that is necessary for that test line to become visible, and these cut-offs can be adjusted by varying the density of the capture antibody immobilized. Regardless of the presence of βTP in the sample, Protein A at the control line would bind to the antibodies on the GNPs resulting in the formation of a visible red control line, indicating successful sample flow through the strip and thus valid test results.

We aimed to design our barcode-style LFA to have test line cut-off values that correspond to the threshold values established by Bernasconi and coworkers.[83] At βTP concentrations of <0.7 mg/L, zero or one test line should appear indicating no CSF leak. βTP concentrations between 0.7 and 1.3 mg/L, which are in the "gray zone", should result in two test lines appearing. Samples classified within the gray zone cannot confidently be diagnosed and should undergo further testing before a clinical decision is made. Samples containing concentrations greater than 1.3 mg/L should result in the formation of three test lines, which would indicate the presence of a CSF leak.

Initial range of detection and cut-off values of the LFA were determined using known concentrations of recombinant βTP in PBS. In all cases, pink control lines were visible indicating valid test results. βTP was accurately detected at all concentrations tested indicated by the formation of visible pink test lines on all strips. More specifically, when the original sample contained 0.3 mg/L of βTP, one visible test line at the T1 position was present, at 0.9 mg/L two visible test lines at the T1 and T2 position were present, and at 3 mg/L three visible test lines at the T1, T2, and T3 position were present (**Figure 2-2**). These results correctly correspond with the desired cut-off values.

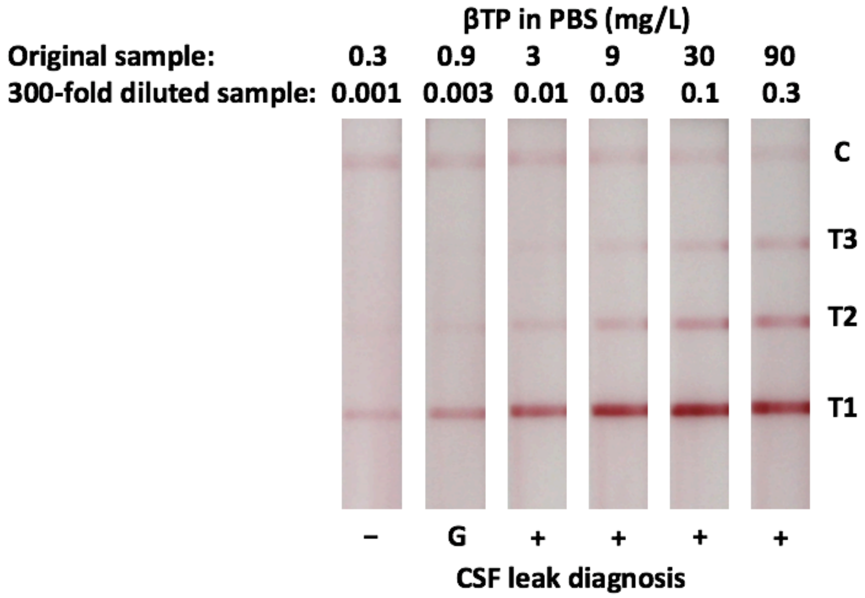

Figure 2-2 Barcode-style LFA results for the detection of recombinant βTP in PBS. Negative (-), Gray Zone (G), and Positive (+) results are indicated.

Next, the LFA was tested with samples of pooled human serum. It was able to detect native βTP for all dilutions tested, indicated by the appearance of a visible line at the T1 location on all strips (**Figure 2-3**). For the 300-fold and 1000-fold preanalytical sample dilutions of pooled human serum, T1 was the only visible line. These samples were thus classified as negative for the presence of CSF using our assay. In contrast, when the serum was diluted by only 100-fold, there were visible test lines at the T1 and T2 locations, which corresponds to the gray zone.

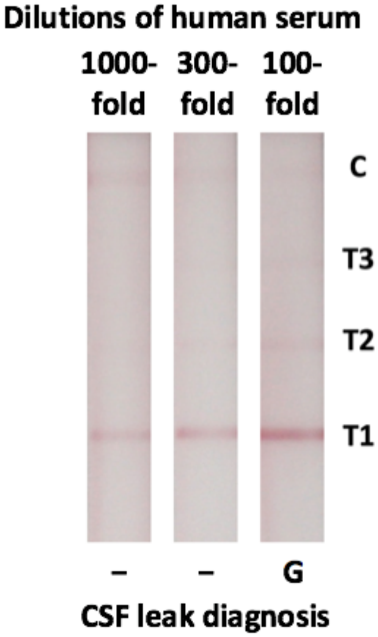

Figure 2-3 Barcode-style LFA results for the detection of native βTP from human serum. Negative (-), Gray Zone (G), and Positive (+) results are indicated.

Finally, multiple samples of CSF obtained from de-identified lumbar drains were mixed with human serum to simulate patient nasal drip samples containing varying amounts of CSF. These samples were then diluted by 300-fold prior to application to the LFA (**Figure 2-4**). When tested on the LFA, CSF that was not mixed in serum (CSF only) produced visible lines at all three test line locations. Three visible test lines were also visible down to the 5-fold dilution of CSF in human serum, correctly indicating these samples were positive for CSF. The 10-fold dilution of CSF in human serum produced two visible test lines, classifying this sample as in the gray zone where further testing is recommended. Lastly, human serum without any CSF produced only one test line, correctly indicating the sample is negative for CSF.

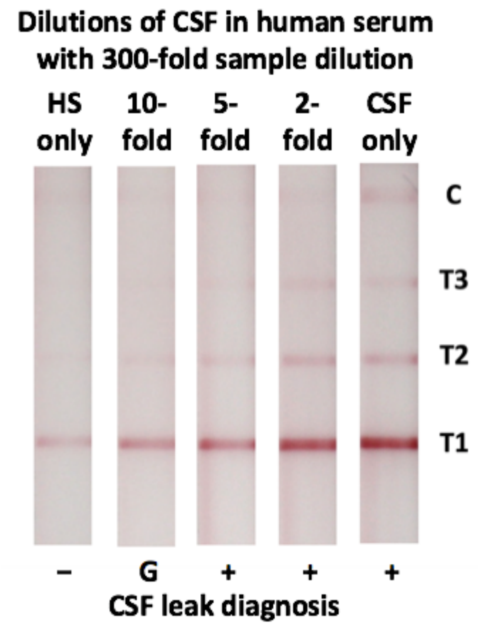

Figure 2-4 Detection of CSF diluted in human serum (HS) with our barcode-style LFA. Negative (-), Gray Zone (G), and Positive (+) results are indicated.

2.4. Discussion

There is a need for a point-of-care test that would allow for rapid detection of skull base violation at the bedside and in clinics. The implications of a device capable of detecting CSF also extend beyond the field of Otolaryngology. Such a device could be used to identify injuries to the spinal cord or globe and may have a role in ruling out CSF leaks in postoperative neurosurgical patients with a low pretest probability of having a leak. One biomarker for detecting CSF leaks is βTP which has shown excellent sensitivity and specificity in a research setting. Unfortunately, it has not been widely accepted as a target in clinical detection, partly due to the current assays requiring expensive and centralized equipment that is not readily available in many clinical settings. This makes it an excellent candidate for novel translational advances. Therefore, we have created a barcode-style LFA that quantifies the βTP concentration in a sample for the rapid detection of CSF leaks.

Initial testing demonstrated that our LFA was able to detect concentrations of recombinant βTP much lower than the desired cut-offs, so it was determined that a 300-fold preanalytical sample dilution would be required to adjust the range of detection and reduce the instance of false positives (**Figure 2-2**). When moving to patient samples, this preanalytical sample dilution also had the added benefit of reducing viscosity to enable better flow. Next, dilutions of human serum were tested with the LFA to confirm its ability to detect native human βTP. The βTP concentration of the serum is expected to be close to the previously reported average of 0.59 mg/L.[80,82] This is below the 0.7 mg/L cut-off for a negative result and so we expect one test line to be visible on the LFA strip with the appropriate dilution. The results shown in **Figure 2-3** support the use of the previously determined 300-fold preanalytical sample dilution to ensure this true negative result (one test line). While we acknowledge that the βTP concentration in serum is different (and greater) than that in nasal secretions, this was an important negative control as serum is a possible contaminant in nasal secretions.

Lastly, when a sample of CSF from lumbar drains (CSF only) was diluted by 300-fold and tested with the LFA, it was correctly identified as positive (**Figure 2-4**). In addition to being able to detect pure CSF, it is important that our assay can correctly detect CSF that has been diluted in serum, as it is common for CSF to be diluted in nasal or otologic secretions prior to collection. When the sample to be tested containing CSF was diluted in the human serum, positive detection was observed down to the 5-fold dilution of CSF in serum, while the 10-fold dilution was classified as in the gray zone. While the gray zone is not a confirmatory result and future laboratory testing should be performed in a clinical setting, it does suggest that our device has the ability to identify leaks that have been diluted up to 10-fold by nasal or otologic secretions. This is comparable to previously reported values for beta-2 transferrin electrophoresis.[84,85]

Note that the absence of a visible control line on all tests containing human serum (**Figure 2-3** and **Figure 2-4**) was not due to inadequate flow of the sample solution through the test, as all of the sample was wicked out of the test tube. We attributed this weak control line to endogenous antibodies in the human serum outcompeting the antibodies on the GNPs for Protein A on the control line. In the future version of our test strip, we will adjust this by replacing Protein A with a species specific secondary antibody.

Limitations of this device may include the detection of very dilute (<10%) samples and detection of intermittent leaks. These limitations, however, both similarly apply to samples analyzed electrophoretically for beta-2 transferrin.[84,85] Also, while the stratified barcode readout makes interpretation simple, further testing and evaluation may still be required when samples test within the “gray zone”, limiting its use as a standalone test.

Other important considerations include contamination of samples with other body fluids known to contain βTP. It has been shown that individuals with end-stage renal disease, cardiovascular disease, and bacterial meningitis may have serum concentrations of βTP in the range of positive detection by our device.[86,87] In the instance of cardiovascular disease, this has been cited as 1.33 +/- 0.63 mg/L, well within the range of positive detection by our device.[86] These findings emphasize the importance of ensuring that samples do not have blood contamination and may cause clinicians to more carefully consider patient co-morbidities when a positive result is obtained.[88,89] Furthermore, concentrations of βTP in nasal secretions are much lower than those in serum, and in the absence of serum contamination, should be one to two orders of magnitude lower than the βTP concentrations in CSF.[82] A negative result is thus unlikely to contain CSF or have serum contamination. These findings highlight the importance of pre-test clinician suspicion for a CSF leak and suggest that this device may have a powerful role in excluding CSF leaks in appropriately selected patient populations. Future work will involve the testing of healthy human nasal secretions to ensure true negative test results in this population. Additionally, equivocal samples from patients with suspected CSF leaks will be tested to evaluate the sensitivity and specificity of our device.

2.5. Conclusion

Cerebrospinal fluid leaks are an excellent target for point-of-care testing in Otolaryngology. The ability of a simple device to accurately detect cerebrospinal fluid will help diagnose these devastating leaks more rapidly and rule them out less expensively. Here we describe the creation of a barcode-style, lateral-flow immunoassay that detects beta-trace protein and classifies the concentration of detected protein in a semi-quantitative fashion into three ranges which allow for ease of clinical interpretation. In initial studies, this device has been able to detect resuspended beta-trace protein as well as cerebrospinal fluid samples diluted in serum up to 10%. This device shows that bedside cerebrospinal fluid identification is feasible and has the potential to influence decision-making without additional expensive diagnostic workup.

Chapter 3. Rapid Diagnostic Test Kit for Point-of-Care Cerebrospinal Fluid Leak Detection

3.1. Introduction

Cerebrospinal fluid (CSF) leaks occur when there is a defect in the dura mater which results in a communication between the intracranial cavities and the external environment. CSF leaks are a common complication of numerous procedures in otolaryngology where the risk in endoscopic skull base surgery has been estimated at 13.8%, endoscopic sinus surgery at 0.17%, and cochlear implantation at 0.4%.[72–74] In fact, almost all procedures involving the sinuses, skull base, or ear carry some risk of a leak. Individuals who have not undergone surgical procedures are also at risk for CSF leaks. Approximately 80% of all leaks occur as a result of nonsurgical traumatic injuries, such as facial and skull bone fractures.[90] While rare, some individuals even present with spontaneous CSF leaks such as CSF otorrhea from an encephalocele.[75] Persistent CSF leaks can result in chronic headaches and discomfort, as well as increase a patient's risk of developing life-threatening complications such as bacterial meningitis and brain abscess.[91,92] Therefore, early diagnosis and subsequent repair of CSF leaks is imperative to prevent these complications.

In the acute setting, assessment is performed using imaging modalities such as magnetic resonance imaging or computed tomography.[93] If there is high enough clinical suspicion, such as obvious facial or skeletal deformities, or copious clear rhinorrhea or otorrhea, patients may be taken directly to the operating room for management. This involves first identifying the site of the leak and then using either native tissue or biocompatible materials to patch the affected site.

In an outpatient or postoperative hospital setting, diagnosing a CSF leak can be much more difficult. It is not uncommon for patients to exhibit heighted secretions after surgery and thus distinguishing normal secretions from those containing CSF can be difficult. Physicians could turn toward the imaging techniques used in the acute hospital settings; however, the cost is often difficult to justify for patients who otherwise seem healthy. Laboratory-based techniques for the detection of CSF may also be implemented. The laboratory gold standard technique involves the identification of the CSF-specific protein beta-2 transferrin using immunofixation electrophoresis.[85,94–97] While proven to have excellent sensitivity and specificity in detecting CSF leaks, electrophoretic assays tend to be time-consuming, expensive, and labor-intensive. Additionally, these assays may not be readily available in some clinical laboratories, and thus, a sample must be sent to a tertiary site for analysis where days to weeks may pass before results return.[98]

As an alternative, researchers have investigated beta-trace protein (βTP), also known as lipocalin-type prostaglandin D2-synthase, as an indicator of CSF leaks. βTP is a ubiquitous protein present at various concentrations throughout the body, but is notably 1 to 2 orders of magnitude more concentrated in CSF than in serum and nasal secretions.[99] As a result, numerous studies have demonstrated that nasal secretions with βTP concentrations (measured using laser nephelometry) above a certain threshold are highly likely to be contaminated with CSF.[78–82] A recent study by Bernasconi *et al.* demonstrated that concentrations of βTP in nasal secretions ≥1.3 mg/L indicate the presence of a CSF leak, whereas concentrations of βTP <0.7 mg/L indicate the absence of a leak. βTP concentrations between 0.7 and 1.29 mg/L (denoted the "gray zone") required further analysis and comparison with the patient's βTP serum level to confirm the presence or absence of a CSF leak. Overall, this approach showed a sensitivity and specificity of 98.3% and 96%, respectively.[83] While the nephelometric assay is more rapid than electrophoresis, it still requires centralized laboratory equipment that may not be available in every clinical setting. In fact, there are still no proven, widely available diagnostic techniques that allow physicians to rule out the presence of a CSF leak in a rapid, affordable, and non-invasive manner.

To address this, our lab has previously developed a semi-quantitative, barcode-style lateral-flow immunoassay (LFA) for the detection of βTP.[100] Using this LFA, we demonstrated the ability to identify serum samples containing trace amounts of CSF from those that did not. In the work presented here, we have developed a rapid diagnostic test kit containing our semi-quantitative LFA for detecting βTP, a collection swab, diluent buffers, and disposable quantitative transfer pipettes. We have validated this kit by testing a variety of different patient samples collected from regions surrounding the brain, and demonstrated the kit's ability to serve as a rapid, low-cost screening tool for the detection of CSF leaks.

3.2. Materials and Methods

3.2.1. Formation of anti-βTP antibody-conjugated gold nanoprobes (GNPs)

All reagents and materials were purchased from Sigma Aldrich (St. Louis, MO) unless otherwise noted. Gold nanoprobes for the detection of βTP were prepared according to our previously reported protocol.[100] Briefly, anti-βTP gold nanoprobes (GNPs) were formed by first mixing 35 μL of a 0.1 M sodium borate solution (pH 9) with a 1 mL suspension of 40 nm citrate-capped gold nanoparticles (Nanocomposix, San Diego, California). Subsequently, 8 μg of anti-βTP detection antibodies were added and incubated for 30 min at room temperature to allow the formation of dative bonds between the antibodies and the surface of the gold nanoparticles. The surface of the gold nanoparticles was then passivated to prevent the nonspecific binding of other proteins by adding 100 μL of a 10% w/v bovine serum albumin (BSA) solution and allowing the mixture to react for 10 min. Lastly, free antibodies were removed from the suspension by three centrifugation steps at 9000 RCF for 6 min, followed by a final resuspension in 100 μL of a 0.1 M sodium borate buffer (pH 9).

3.2.2. Preparation of barcode-style LFA test strips

LFA test strips were constructed by overlapping and securing different functional paper pads on an adhesive backing. Each LFA test strip included a sample pad, conjugate pad, nitrocellulose membrane, and absorbent pad. Each sample pad was made by dehydrating 12 μL of 1% w/v BSA in 0.1 M Tris buffer (pH 9) onto a 3 x 10 mm fiber glass paper pad. Each conjugate pad was made by dehydrating a 12 μL suspension containing 2.5 μL GNPs and 1% w/v BSA overall onto a 3 x 10 mm fiber glass paper pad. Both the sample pads and conjugate pads were dehydrated under very low pressure using a Labconco FreeZone 4.5 lyophilizer (Fisher Scientific, Hampton, New Hampshire) for 2 h.

The nitrocellulose membrane was prepared by immobilizing antibodies at three different test line locations (T1, T2, and T3) and a control line location. The concentrations of the anti-βTP detection antibodies immobilized at T1, T2, and T3, were 2, 0.5, and 0.35 mg/mL, respectively. The control line was composed of an anti-mouse IgG secondary antibody immobilized at 0.5 mg/mL. The antibody immobilization process was performed by printing solutions of antibodies in 25% w/v sucrose onto a nitrocellulose membrane using an Automated Lateral Flow Reagent Dispenser (Claremont BioSolutions, Upland, California) and a Fusion 200 syringe pump (Chemyx, Stafford, Texas) at a flow rate of 250 μL/min. The printed membrane was then left in a vacuum-sealed desiccant chamber overnight. After antibody immobilization, the nitrocellulose membrane was blocked by immersing it in a solution of 1% w/v BSA in 0.1 M Tris buffer for 1 h followed by dehydration overnight at low pressure with a lyophilizer.

To assemble the LFA test strip, the nitrocellulose membrane was first mounted onto the adhesive backing. The absorbent pad was adhered onto the adhesive backing just downstream of the control line, where it overlapped the nitrocellulose membrane by 2 mm. Next, the conjugate pad was adhered onto the backing just upstream of the test lines, where it overlapped the nitrocellulose membrane by 1 mm. Lastly, the sample pad was adhered to the region of adhesive backing upstream of the conjugate pad while also overlapping the conjugate pad by 2 mm.

3.2.3. Preparation of diagnostic kit for CSF leak detection

A rapid diagnostic test kit was assembled containing one barcode-style LFA test strip, one Flexible Minitip Flocked Swab (Becton, Dickinson and Company, Franklin Heights, NJ), two disposable Samco Exact Volume Transfer pipettes (Thermo Scientific, Waltham, MA) with a capacity of 100 μL, diluent buffers, and user instructions. Tube A contained 2,320 μL of phosphate-buffered saline (PBS). Tube B contained 450 μL of PBS mixed with 450 μL of running buffer (0.4% BSA, 0.6% Tween 20, 0.2% polyethylene glycol, 0.1M Tris buffer pH 9). Tube C was supplied empty. All components were placed in a resealable bag with desiccant for storage.

3.2.4. Operation and validation of rapid diagnostic test kit for CSF leak detection

The schematic representation of the user steps for our diagnostic test kit is shown in **Figure 3-1**. To determine whether a sample fluid contained CSF, the fluid was first absorbed into the collection swab. The swab was then inserted into the buffer in tube A and twirled around the edge of the tube for 10 s at 2 rotations per s in order to release the sample from the swab into the buffer. Tube A was then inverted 5 times to ensure the released sample was well-mixed. Next, 100 μL of the liquid in tube A was transferred to tube B using one of the provided disposable transfer pipettes.

Tube B was then inverted 5 times to ensure complete mixing. The release of the sample from the swab into tube A and the subsequent transfer into tube B resulted in an overall 300-fold dilution of the original sample. Lastly, 100 μL of the solution in tube B was transferred into tube C where the barcode-style LFA test strip was also inserted. After 20 min, the results were interpreted where the formation of 0 and 1, 2, or 3 visible test lines indicated a diagnosis of negative, gray zone, or positive, respectively. Photographs of the test strips were taken by a Nikon D3400 digital camera (Nikon, Tokyo, Japan) in a controlled lighting environment.

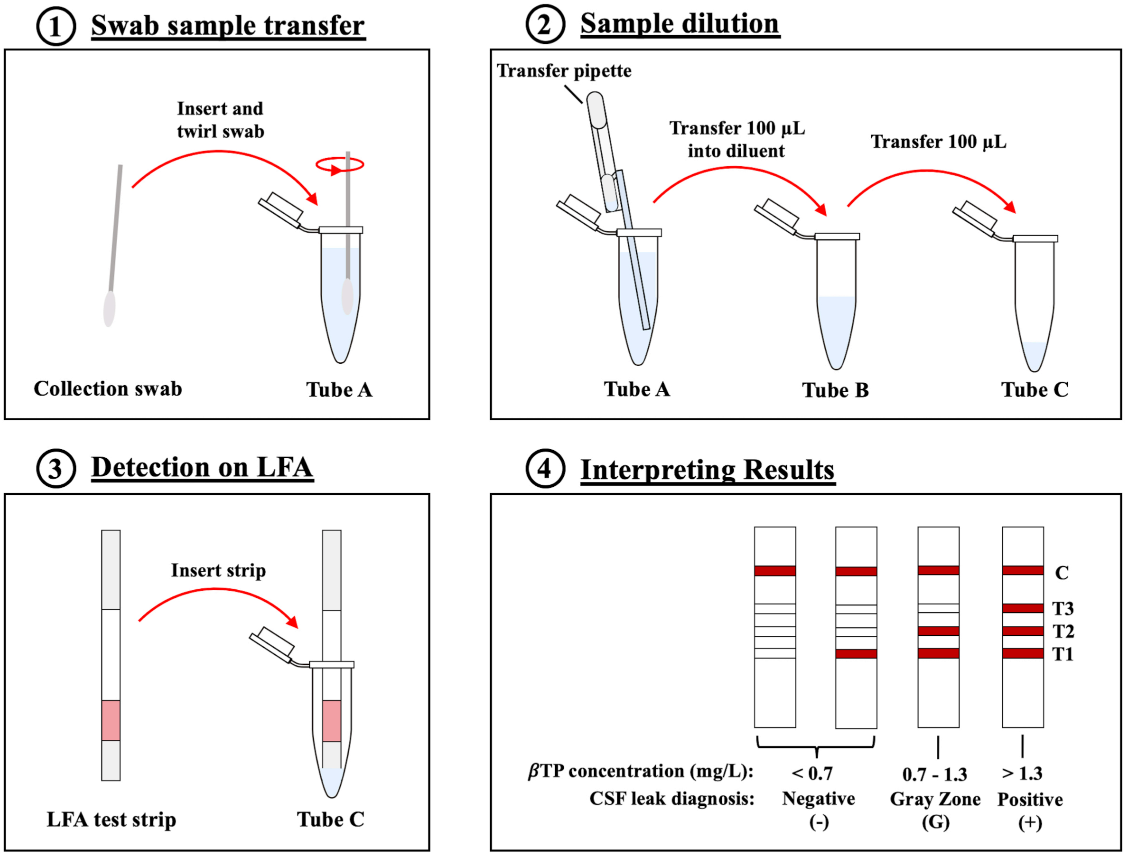

Figure 3-1 Schematic representation of the procedure for operating our rapid diagnostic test kit for the detection of CSF leaks. (1) Swab with collected sample is dipped and twirled in tube A buffer to release sample. (2) Released sample from tube A is further diluted in tube B using disposable transfer pipettes and then transferred to tube C. (3) Barcode-style LFA test strip is inserted into the fluid in tube C for 20 min. (4) Test results are interpreted by the user.

We first evaluated the ability of our diagnostic test kit to detect for βTP by testing samples containing purified, recombinant βTP in PBS. Then we evaluated a variety of different patient samples collected at the Ronald Reagan UCLA Medical center which were either negative or positive for the presence of CSF. These included fluids collected from skull base sites during endoscopic transnasal transsphenoidal (TNTS) surgeries, superior semicircular canal dehiscence (SSCD) repair surgeries, and brain tumor resection surgeries. Rhinorrhea and otorrhea specimens from healthy volunteers and patients with suspected CSF leaks were also included (University of California Los Angeles [UCLA] Institutional Review Board approval 17-001065).

3.3. Results

3.3.1. Barcode-style LFA principle and interpretation

Similar to our previous work, the barcode-style LFA used in our kit was designed such that the presence of the target biomarker, βTP, would produce 1 to 3 visible test lines, because the βTP would become sandwiched between the GNPs and the test line antibodies. Each test line has a cutoff value, which is the minimum concentration of βTP required for that line to become visible to the user. In designing a barcode-style LFA, the cutoff value for each line could be adjusted by varying the concentrations of the immobilized antibodies. Regardless of the presence of βTP, the anti-mouse IgG secondary antibodies immobilized at the control line would bind to the primary antibodies on the GNPs, capturing them. This would result in the formation of a visible red control line to indicate successful flow of the sample solution through the LFA test strip and thus valid test results.

The cutoff values for each test line of our barcode-style LFA were adjusted to correspond with the threshold values proposed by Bernasconi *et al.*[83] βTP concentrations <0.7 mg/L would result in the appearance of 0 or 1 test line and indicate no CSF leak. Between 0.7 and 1.3 mg/L of βTP, 2 test lines would appear and classify the sample as in the "gray zone." Samples that fall within the gray zone cannot be confidently diagnosed as negative or positive for the presence of CSF and therefore should undergo further testing before a clinical decision is made. Lastly, samples with βTP concentrations >1.3 mg/L would result in the appearance of 3 visible test lines, indicating the presence of a CSF leak.

3.3.2. Detection of purified βTP

The performance of our rapid diagnostics test kit for the detection of CSF leaks was first evaluated by testing samples of purified, recombinant βTP in PBS. Solutions containing different concentrations of βTP were collected on a swab, transferred into diluent solutions, and then applied to the barcode-style LFA test strip. For all experiments, pink control lines became visible on the LFA test strips indicating valid test results. βTP was also able to be detected at all concentrations tested, indicated by the formation of at least one pink test line on each LFA strip. More specifically, when the concentration of βTP was 0.3 mg/mL, a visible test line appeared at the T1 location. At a βTP concentration of 0.9 mg/mL, test lines appeared at the T1 and T2 locations. Lastly, at ≥3 mg/mL of βTP, test lines appeared at the T1, T2, and T3 locations (**Figure 3-2**).

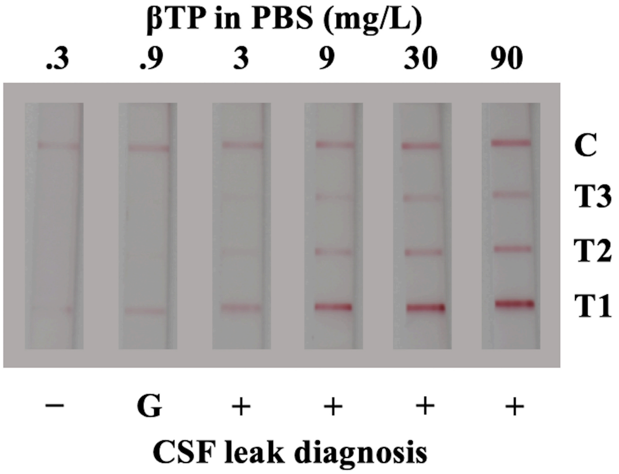

Figure 3-2 Diagnostic test kit results for the detection of recombinant βTP in PBS. Negative (-), Gray Zone (G), and Positive (+) results are indicated.

3.3.3. Detection of clinical samples

Next we evaluated the performance of our diagnostic test kit with clinical samples. To do this, we tested 22 samples from 21 patients. Of these samples, 8 contained CSF from the periphery of the brain and 14 did not contain CSF. The demographics of the study population as well as the sample origins are summarized in **Table 3-1**. 13 samples were collected from the site of surgical procedures, 8 were rhinorrhea specimens, and 1 was an otorrhea specimen.

Table 3-1 Patient characteristics

Characteristic	Data
Patient number (female/male)	21 (13/8)
Age, years (mean ± SD)	45±14
Age range, y	18-70
Sample number	22
Surgical specimen, *n*	13
Rhinorrhea specimen, *n*	8
Otorrhea specimen, *n*	1

Each clinical specimen was collected on a swab, transferred into diluent solutions, and applied to the barcode-style LFA test strip. The results that were obtained are shown in **Figure 3-3** and summarized in **Table 3-2**. Of the 4 surgical specimens containing CSF, 3 produced true positive results, and 1 produced a gray zone result. On the other hand, of the 9 surgical specimens that did not contain CSF, 7 produced true negative results, and 2 produced gray zone results. Rhinorrhea specimens were also examined, where all 3 specimens containing CSF resulted in true positive results, and all 5 specimens that did not contain CSF resulted in true negative results. An otorrhea specimen containing CSF was also tested and it produced a true positive result.

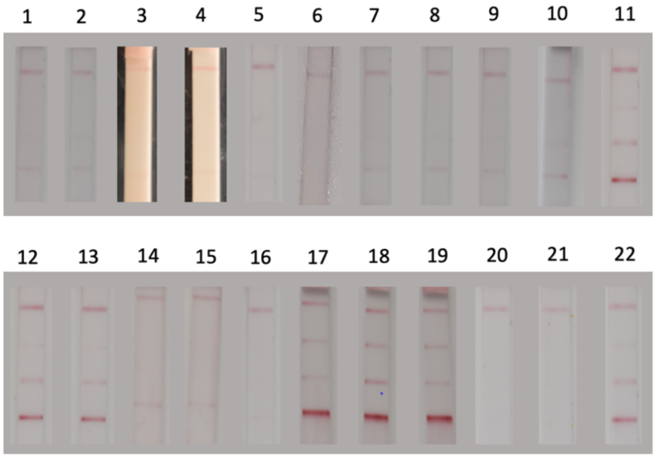

No.	Sample type – CSF status	Test kit results
1	TNTS – no CSF	–
2	TNTS – no CSF	–
3	TNTS – no CSF	–
4	TNTS – no CSF	–
5	TNTS – no CSF	–
6	TNTS – no CSF	–
7	TNTS – no CSF	G
8	SSCD – no CSF	–
9	SSCD – no CSF	G
10	SSCD – CSF present	G
11	Under dura – CSF present	+
12	Subarachnoid cistern fluid – CSF present	+
13	Tumor resection – CSF present	+
14	Rhinorrhea – no CSF	–
15	Rhinorrhea – no CSF	–
16	Rhinorrhea – no CSF	–
17	Rhinorrhea – no CSF	–
18	Rhinorrhea – no CSF	–
19	Rhinorrhea – CSF present	+
20	Rhinorrhea – CSF present	+
21	Rhinorrhea – CSF present	+
22	Otorrhea – CSF present	+

Figure 3-3 Diagnostic kit test strip results for clinical specimens. Negative (-), Gray Zone (G), and Positive (+) results are indicated.

Table 3-2 Summarized diagnostic test kit results

Clinical samples	Diagnostic test kit results Negative	 Gray	 Positive	Total
Surgical specimen with CSF	0	1	3	4
Surgical specimen without CSF	7	2	0	9
Rhinorrhea specimen with CSF	0	0	3	3
Rhinorrhea specimen without CSF	5	0	0	5
Otorrhea specimen with CSF	0	0	1	1
Total	12	3	7	22

Three different strategies for interpreting the diagnostic test kit results were evaluated. In the first method, the gray zone results were interpreted as negative. For the second strategy, the gray zone results were interpreted as being positive. Lastly, in the third strategy, gray zone results were interpreted as being equivocal and ambiguous. The first two interpretation strategies allowed us to simplify the obtained results to provide the user with a binary answer as to whether the tested sample does or does not contain CSF. Ultimately this allowed us to collapse the obtained results onto a 2x2 contingency table to characterize the diagnostic test kit performance (**Table 3-3**). In the first method, where the gray zone was interpreted as a negative result, we obtained a sensitivity of 87.5%, specificity of 100%, positive predictive value (PPV) of 100%, negative predictive value (NPV) of 93.3%, positive likelihood ratio (+LR) of ∞, and negative likelihood ratio (-LR) of 0.125. In the second method, where the gray zone was interpreted as positive, we obtained a sensitivity of 100%, specificity of 85.7%, PPV of 80%, NPV of 100%, +LR of 7, and -LR of 0. In the third interpretation method, where gray zone results are considered equivocal and ambiguous, the results were not binary so they could not be analyzed using a 2x2 contingency table and thus sensitivity, specificity, PPV, and NPV could not be calculated. However, the likelihood ratio (LR) for each detection region could be calculated, where a negative result (0 or 1 test line) had an LR of 0, a gray zone result had an LR of 0.88, and a positive result had an LR of ∞ (**Table 3-4**).

Table 3-3 Diagnostic performance using binary assay interpretation

Interpretation	Sensitivity	Specificity	PPV	NPV	+LR	-LR
Gray zone as negative	87.5%	100%	100%	93.3%	∞	0.125
Gray zone as positive	100%	85.7%	80%	100%	7	0

Table 3-4 Diagnostic performance using non-binary assay interpretation

Assay result	n (%) with CSF	n (%) without CSF	% with CSF/ % without CSF	Likelihood ratio
Negative	0 (0%)	12 (85.7%)	0/85.7	0
Gray zone	1 (12.5%)	2 (14.3%)	12.5/14.3	0.88
Positive	7 (87.5%)	0 (0%)	87.5/0	∞
Total	8 (100%)	14 (100%)	-	-

3.4. Discussion

The early and accurate diagnosis of CSF leaks is vital for the prevention of life-threatening complications such as meningitis. The quantification of βTP in rhinorrhea and otorrhea specimens using nephelometry has previously been reported as an effective method of diagnosing CSF leaks. While it is more rapid than the gold standard laboratory technique of beta-2 transferrin electrophoresis, the nephelometry assay does require the use of expensive, centralized laboratory equipment that is not widely available in all clinical settings. In this work, we created a rapid diagnostic test kit that utilized a barcode-style LFA, and validated its use for the equipment-free collection, dilution, and detection of CSF.

We first tested the rapid diagnostic test kit with purified, recombinant βTP in PBS. Our results demonstrate that the diagnostic test kit can detect for βTP in a semi-quantitative manner, as seen by the increase in the number of red test lines visible on the LFA test strip with an increase in the concentration of βTP. More specifically, positive results were observed at ≥3 mg/L, a gray zone result was observed at 0.9 mg/L of βTP, and a negative result was observed at 0.3 mg/L of βTP. These results correspond relatively well with the cutoff values proposed by Bernasconi *et al.*[83] Additionally, these test results obtained with swabs and disposable transfer pipettes were comparable to that of our previous work which used no swabs and high quality laboratory pipettes for collection and dilution. This is significant because it demonstrates that the samples could be collected, released, and diluted in a quantitative manner using low cost and disposable materials.

All clinical specimens produced true negative and true positive test results, with the exception of three surgical specimens that produced results in the gray zone. One of these specimens contained CSF while the other two did not. All three were collected at the sites of endoscopic surgeries, where a significant amount of blood was collected on the swab. The mean concentration of βTP in human serum has previously been reported as 0.59 mg/L with a range of 0.38 – 0.86 mg/L.[79] Recall that our diagnostic test kit produced gray zone results (two test lines) at 0.9 mg/L of recombinant βTP. Thus, it is possible that the gray zone results obtained for the two surgical specimens without CSF is a result of contamination with blood that has a βTP concentration at the upper end of the reported range. It is worth noting that the other seven surgical specimens with true negative detection also contained blood; however, the blood could have been more dilute or at the lower end of the reported βTP concentration range for serum. Regarding the surgical specimen containing CSF which produced gray zone results, it is likely that the CSF was significantly diluted in other secretions to below the positive detection threshold of our diagnostic kit.

We evaluated three different strategies for interpreting and analyzing our diagnostic test kit results. The first two methods involved simplifying our results of negative, gray zone, or positive to a binary readout of negative or positive. The performance of the first method, where gray zone results were interpreted as negative, is conducive for a rule-in test, because it was highly specific where false positive results are extremely unlikely, and thus a positive result could be used to confidently confirm the presence of the CSF leak. For the second method, where gray zone results are interpreted as positive, our diagnostic test kit became an effective rule-out test, because it has high sensitivity where false negatives are extremely unlikely and thus it can be used to confidently send healthy patients home.

In the case that we designed our diagnostic test kit to only provide binary results, such as if the LFA test strip was printed with one test line as opposed to three test lines, a rule-out test would be desired. From a clinical perspective, a rule-out test is advantageous because it would allow clinicians to more confidently send healthy patients home who were suspected of having a CSF leak and otherwise would have been scanned and admitted into the hospital for observation or further invasive procedures. This would ultimately save hospital resources and minimize the number of healthy patients who would undergo unnecessary and costly workups such as MRI or CT imaging. While the rule-out test would be the most useful binary test for the detection of CSF leaks, it is not without its disadvantages. Note that the rule-out test has a very high sensitivity (100%) at the cost of a slightly lower specificity (85.7%). The PPV was calculated as 80% meaning that 20% of the positive test results were actually false positives. Therefore, further testing would have to be performed for all patients with positive test results prior to intervention in order to confirm the presence of a leak.

To avoid having to choose between a binary test with either high sensitivity or high specificity, a non-binary third interpretation strategy is presented, where the gray zone results are treated as their own category indicating equivocal and ambiguous test results. In the case that the pre-test odds for some unhealthy condition are known, likelihood ratios (LRs) multiply the pre-test odds to determine the post-test odds which then can be converted to the post-test probability that a patient has some condition of interest.[101] Thus, the LR values of 0 for negative and ∞ for a positive test indicates that, regardless of the pre-test probability, a negative test result confirms that the patient does not have a CSF leak, and a positive test result confirms a CSF leak. This is an improvement over the previously discussed second strategy, where 20% of positive results were false positives. Lastly, gray zone results had an LR of 0.88, which provides very little useful information to influence the clinical diagnosis because it is close to 1. Therefore, patients who appear healthy but test within the gray zone would be identified as being at risk of having a CSF leak, and further non-invasive testing, such as beta-2 transferrin electrophoresis, should be performed prior to clinical decision making. It is worth noting that in our study, only 14% of patient samples produced gray zone results which would require further confirmatory testing. This is a significant improvement over the 45% of patients that would be required to receive further testing if the binary rule-out test format was implemented.

Altogether, the diagnostic test kit developed in this study costs under $4 to produce at the laboratory scale and produces results in approximately 20 min. Using our kit, clinicians would be able to rapidly and accurately identify healthy individuals from a pool of patients with suspected CSF leaks. Ultimately, this would save hospital resources by minimizing the number of healthy patients who would otherwise be admitted to the hospital for multiday observation while waiting for beta-2 transferrin electrophoresis results, as well as minimize the number of unnecessary and costly workups such as MRI or CT imaging.

3.5. Conclusion

In summary, we have developed a rapid diagnostic test kit for the detection of CSF leaks. Every step from sample collection through results interpretation can be performed with minimal training and requires only the provided disposable materials which make this kit well suited for use as a point-of-care diagnostic. Validation studies from testing clinical samples that either did or did not contain CSF demonstrated excellent predictive capabilities. Overall our test kit has the potential to influence the clinical decision-making process by preventing unnecessary workups for healthy patients and rapidly confirming the presence of leaks in unhealthy patients. Ultimately this will lead to the improved management and treatment of CSF leaks. This kit has the potential to transform patient outcomes.

Chapter 4. Equipment-Free, Therapeutic Drug Monitoring of Digoxin Through Integration of the Lateral-Flow Immunoassay with Gold Nanorod Etching

4.1. Introduction

Heart disease remains the leading cause of death for adults in the United States. It is estimated that about 5.7 million adults in the United States live with heart failure (HF) and that number is expected to increase to >8 million by 2030.[102] Each year, HF costs the nation $30.7 billion in healthcare services, medications, and missed days of work.[103] In addition, cardiovascular disease disproportionally affects underrepresented populations, which are often in areas with reduced healthcare access.[2] One commonly used drug for the treatment of heart failure, as well as some types of cardiac arrhythmias, is the cardiac glycoside digoxin.

Despite being the oldest and one of the most well-known drugs for the treatment of HF, digoxin remains one of the most challenging cardiovascular therapies to prescribe and administer properly. This is due to its narrow therapeutic window and the small difference between its therapeutic and toxic doses.[104] To address this issue, therapeutic drug monitoring is often employed to measure the blood plasma concentration of the drug and ensure that the trough level is within the therapeutic range of 1-2 ng/mL as opposed to the toxic concentration (>2.8 ng/mL).[105] If the measured concentration of digoxin in the blood is not within the desired range, the patient's next dose can be adjusted, thus providing a method of individualizing treatment. Typically, highly quantitative techniques such as the enzyme-linked immunosorbent assay (ELISA), high performance liquid chromatography or automated immunoassay systems are utilized for monitoring cardiac drugs.[106–108] Despite their success in a large hospital setting, these tests are not feasible for use in small/mobile clinics which reside in underserved communities due to the requirement of very expensive equipment, trained laboratory personnel, and a long time to result, especially if the sample has to be sent away to an offsite laboratory.[109]

One effort to make the ELISA more suitable for use in resource-limited settings was the development of the plasmonic enzyme-linked immunosorbent assay (pELISA).[27,110] In the pELISA, traditional chromogenic substrates were replaced with plasmonic nanoparticles. One mechanism involved coupling analyte capture with a reaction that controlled the anisotropic etching of gold nanorods (GNRs).[44,47] Different concentrations of the target analyte would result in different sized GNRs, and thus different colored suspensions. This produced a multicolor readout with a full spectrum of colors. The results were easily interpreted with the naked eye by comparing the color development with a provided reference card (much like litmus pH test strips). While effective at introducing a quantitative naked-eye readout to the ELISA, the pELISA still had a long time to result and required trained personnel to perform the many binding and washing steps which made it not ideal for use at the point of care. Therefore, there is still a need for a point-of-care device that can perform quantitative therapeutic drug monitoring for underserved communities.

A point-of-care device should be small and lightweight, require minimal power, training and equipment and also be low in cost. One device that satisfies these criteria is the lateral-flow immunoassay (LFA). The LFA is a paper-based device that transports a sample via capillary action and uses colorimetric indicators conjugated with antibodies to visually detect the presence or absence of a target analyte. The most successful version of the LFA is the over-the-counter pregnancy test which has achieved widespread success in today’s market due to its ease of use and accurate, rapid results. Despite its success, the LFA still suffers from a few disadvantages which limit its ability to completely replace laboratory-based assays.[3] One of these is that the conventional LFA only provides the user with a qualitative “yes” or “no” readout. For this reason, the traditional LFA is not appropriate in situations such as therapeutic drug monitoring where a quantitative answer is required. Various approaches have been developed in order to introduce a more quantitative readout to the LFA, such as the barcode-style LFA[16,111,112] and electronic readers.[7,113,114] While these approaches have been useful, the barcode-style LFA has a relatively poor quantitative resolution, while the requirement of electronic readers can increase the cost and complexity of an assay. Thus, there is still a need for inexpensive, easy-to-use, rapid assays that allow for naked-eye quantification of biomarkers at the point of care.

In this work, we develop a technique which combines the LFA with the signal generation capabilities of the pELISA to improve the naked-eye quantitative capabilities of the LFA. Digoxin capture and binding occurs on our modified LFA test strip which utilizes platinum nanozyme probes with catalase-like activity. This test strip is combined with a reaction that controls the oxidative, anisotropic etching of GNRs to produce a wide range of visible colors dependent on the initial digoxin concentration in the sample. We demonstrated the ability of this technique to be used for the naked-eye quantification of digoxin in human serum samples within the relevant concentration range of 0.25-4.0 ng/mL. To our knowledge, this is the first reported integration of the lateral-flow immunoassay with gold nanorod etching, as well as the first multicolor LFA readout where the color produced is dependent on the concentration of the antigen analyte.

4.2. Materials and Methods

4.2.1. Synthesis of gold nanorods (GNRs)

GNRs were synthesized using a modified version of the seeded growth method reported by Murray and coworkers.[115] This method requires the preparation of both gold nanoparticle seeds and a growth solution. To make the seed solution, 5 mL of a 0.2 M solution of cetyltrimethylammonium bromide (CTAB) was first prepared by stirring and heating on a hot plate until fully dissolved, followed by cooling to 30 °C. Next, under continuous, vigorous stirring at 30 °C, 2.5 mL of filtered ultrapure water and 2.5 mL of 1 mM $HAuCl_4$ were added into the CTAB solution. This was followed by the addition of 1 mL of freshly prepared 6 mM sodium borohydride. The solution was stirred for 2 min, upon which the color changed from yellow to brownish-yellow indicating the formation of small gold nanoparticle seeds of approximately 3-4 nm. The seed suspension was left to age for 30 min.

The growth solution was prepared by mixing 1.08 g of CTAB and 0.132 g of 5-bromosalicylic acid (Tokyo Chemistry Industry America, Portland, OR) in 30 mL of filtered ultrapure water which was heated and stirred on a hot plate until fully dissolved. This solution was cooled to 30 °C, then 1.44 mL of a 4 mM silver nitrate solution was added to the growth solution, quickly mixed, and then left undisturbed for 15 min at 30 °C. Next, 30 mL of 1 mM $HAuCl_4$ was added and the solution was stirred with a magnetic stir bar at 800 RPM. After 15 min of stirring, 240 µL of a 64 mM ascorbic acid solution was vigorously stirred into the solution for 30 s until it became colorless, indicating the reduction of Au(III) to Au(I).

Finally, 24 µL of the previously made gold seed solution was added and stirred for another 30 s. The solution was then left to sit undisturbed for at least 12 h before the purification and concentration steps. After this time period, the solution was centrifuged for 15 min each at 8600

RCF and 30 °C, after which the supernatant was discarded and the pellet of gold nanorods was resuspended in filtered ultrapure water. This centrifugation was then repeated and the final pellet was resuspended 2 mL of filtered ultrapure water. All reagents and materials were purchased from Sigma-Aldrich (St. Louis, MO) unless otherwise noted.

4.2.2. Demonstration of gold nanorod etching for multicolor signal generation

The GNR etching precursor solution for one reaction was made by mixing 50 µL of a solution containing 20 mM cetyltrimethylammonium bromide (CTAB) and 20 mM Tween 20, with 10 µL of synthesized GNRs, 10 µL of 1.4 M NaBr in 0.1 M citrate buffer (pH 4), 5 uL of 100 µM horseradish peroxidase (HRP) in 0.1 M phosphate buffer (pH 6), and 5 uL of Milli-Q water in a well of a 96-well plate. To perform the etching reaction, 20 µL of varying concentrations of hydrogen peroxide in 5 mM NaOH were mixed into each well containing the GNR etching precursor solution. After 10 min, photographs were taken with a Nikon D3400 digital camera (Nikon, Tokyo, Japan) in a controlled lighting environment and the UV-Vis spectra were observed using a Synergy H1 Hybrid Multi-mode reader (BioTech, Winooski, VT).

4.2.3. Preparation of anti-digoxin antibody-decorated porous platinum-shell gold-core nanozyme probes (PtNPs)

Gold nanoparticles (GNs) were synthesized according to Turkevich *et al.*[31] Briefly, 9.9 mL of ultrapure water in a scintillation vial was heated to a boil on a 350 ºC hot plate with magnetic stirring at 1200 RPM. Once boiling, the heat setting was turned down to 200 ºC. Then, 100 µL of a 1% w/v gold (III) chloride solution was added to the vial. After 1 min, 90 µL of a 2% trisodium citrate w/v solution was also added and allowed to react for 10 min. The hydrodynamic diameter of the resulting gold nanoparticles was measured to be 19 nm using dynamic light scattering (DLS) with a Zetasizer Nano SZ particle analyzer (Malvern Instruments Inc., Westborough, MA). Subsequently, the concentration was calculated to be 1.14 nM using Beer's law, where the peak absorbance was measured using a UV-Vis spectrophotometer and the molar extinction coefficients were determined from a datasheet provided by BBInternational Life Sciences.

Porous platinum-shell gold-core nanozymes (PtNs) were synthesized using a protocol modified from Loynachan *et al.*[116] In a 20 mL glass scintillation vial, 200 µL of a 20% w/w polyvinylpyrrolidone (PVP, 10 kDa) solution was mixed with 7.4 mL of ultrapure water and 2.6 mL of GNs (1.14 nM, 19 nm hydrodynamic diameter) and allowed to incubate for 5 min. 400 µL of a 100 mM platinum chloride solution and 400 µL of a 100 mg/mL L-ascorbic acid solution were then added and immediately mixed. The solution was then allowed to react in a 70 ºC oil bath under magnetic stirring at 1200 RPM. During this reaction the platinum ions would be reduced by the L-ascorbic acid and deposited onto the surface of the GNs resulting in the formation of a thick, porous platinum shell. The resulting suspension was cooled in a 25 ºC water bath for 1 h. To purify the particles from excess reagents, the suspension was split into 1 mL aliquots in microcentrifuge tubes, centrifuged at 8600 RCF for 12 min and the resulting pellets were resuspended in 1 mL ultrapure water. The original supernatants were recentrifuged at 8600 RCF for 12 min and the resulting pellets also resuspended in 1 mL ultrapure water. Lastly, the supernatants resulting from the centrifugation of the original supernatants were recentrifuged at 8600 RCF for 12 min and the resulting pellet resuspended in 1 mL ultrapure water. Each of these resuspended pellets were centrifuged a final time at 8600 RCF for 12 min and resuspended in 1 mL of ultrapure water.

To create anti-digoxin antibody-functionalized porous platinum-shell gold-core nanozyme probes (anti-digoxin PtNPs), 83 µL of purified PtNs were first diluted in 917 µL of Milli-Q water.

Next, 8 μL of a 0.1 M sodium borate (pH 9) solution was added to adjust the platinum-shell gold-core nanozyme (PtN) suspension pH to 7. Subsequently, 1 μg of anti-digoxin monoclonal antibody (Fitzgerald Industries International, Acton, MA) was added and the mixture was allowed to react for 30 min to allow the antibodies to adsorb and conjugate onto the surface of the PtNs through a combination of electrostatic interactions, hydrophobic interactions, and dative bonds. This was followed by the addition of 100 μL of a 10% (w/v) bovine serum albumin (BSA) solution in filtered ultrapure water in order to passivate the surface of the PtNs. After reacting for 10 min, the suspension was purified of free antibodies using three centrifugation cycles. The pellets resulting from the first two cycles were resuspended in 200 μL of 1% BSA in filtered ultrapure water, while the pellet from the final centrifugation cycle was resuspended to a total volume of 50 μL in a 0.1 M sodium borate (pH 9) solution.

4.2.4. Preparation of test strip for detection of digoxin

Proteins were printed and immobilized on the nitrocellulose membrane using an Automated Lateral Flow Reagent Dispenser (Claremont BioSolutions LLC, Upland, CA) with the voltage setting at 4.5 V and a Fusion 200 syringe pump (Chemyx Inc, Stafford, TX) with a flow rate of 250 μL/min. The test line was formed by printing a solution of 0.5 mg/mL digoxin-BSA (Fitzgerald Industries International, Acton, MA) in 25% (w/v) sucrose at two locations that were 1 mm apart with two print cycles each, such that the solution printed merged into one thick test line. The control line was formed by printing a solution of 0.5 mg/mL Rabbit anti-goat IgG secondary antibody with two print cycles. The printed membrane was left in a vacuum-sealed desiccation chamber overnight.

To assemble the test strip, the nitrocellulose membrane was first adhered to an adhesive backing and cut into 5 mm wide strips. A 5 × 15 mm fiberglass sample pad was placed on the adhesive upstream of the test line and overlapping the nitrocellulose membrane by 2 mm. A 5 × 22 mm cotton linter absorbent pad was placed on the adhesive backing downstream of the control line and overlapping the nitrocellulose membrane by 2 mm.

This LFA test strip was then modified and placed in a custom-made, 3D-printed casing which allowed for the test line region to be removed after the assay was complete by simply pulling on a plastic tab. To assemble the device, this test strip was first cut into three segments. The segments containing the sample pad and the absorbent pad were fit into the bottom piece of the casing (**Figure 4-1**). The cut-out LFA test line was adhered to the test line pull tab which slid into the bottom piece of the casing. In order to allow a sample fluid to flow from one segment to the next, 5 × 3 mm fiberglass pads were adhered to the top piece of the casing at two locations which bridged the gaps between the test strip segments. The flexible middle piece of the casing provided a seal between the top and bottom pieces so that no liquid could flow in the gaps between them. All casing components were 3D printed using an Ultimaker 3 (Ultimaker B.V., Geldermalsen, Netherlands). The test line pull tab, bottom, and top pieces of the casing were printed from Ultimaker CPE filament (Co-polyester), while the middle seal was printed from Ultimaker TPU 95A filament (thermoplastic polyurethane).

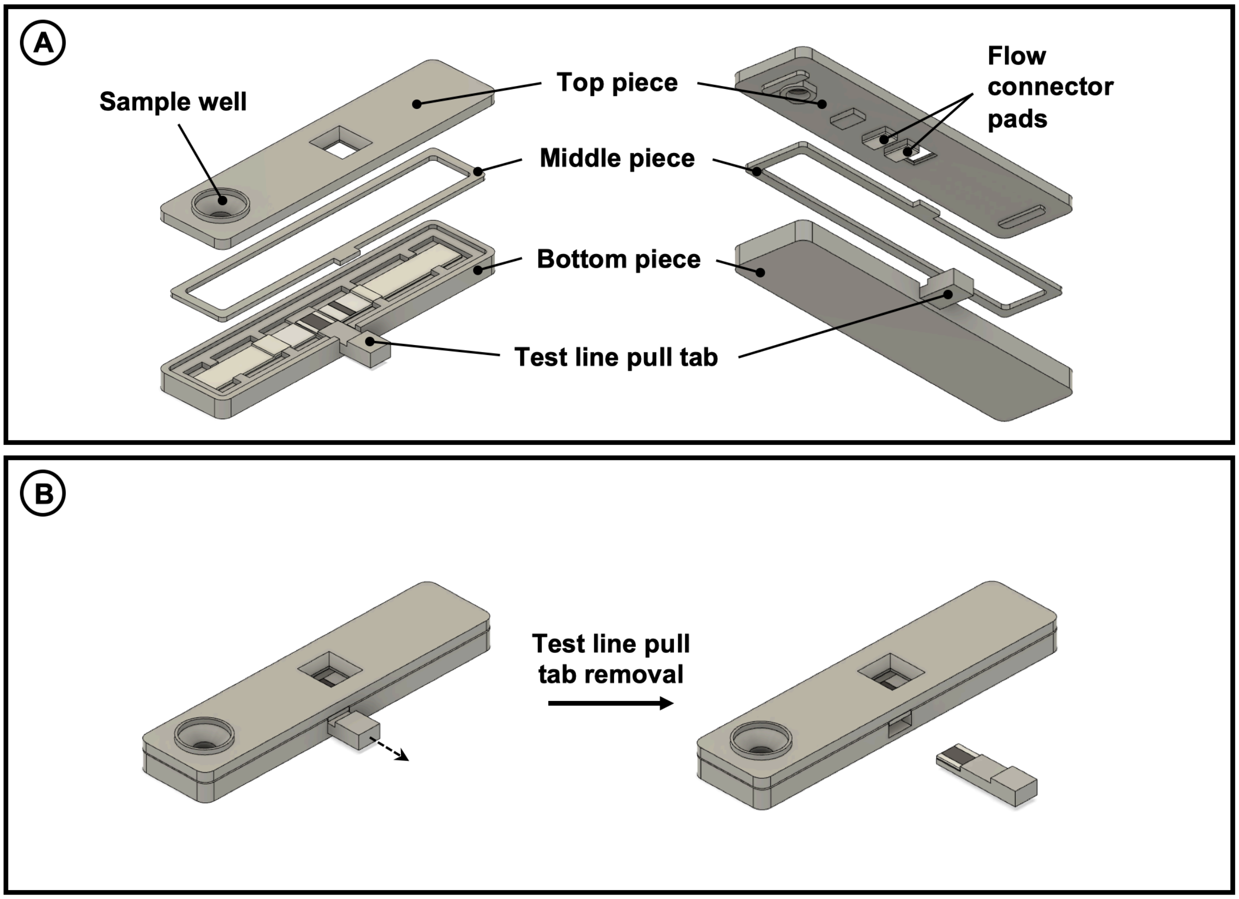

Figure 4-1 Schematic of test strip for integration with the multicolor reaction
(A) Design of 3D printed casing and assembly for the LFA test strip with flow connector pads
(B) Removal of the test line region using the test line pull tab

4.2.5. *Quantitative detection of digoxin using the LFA with a multicolor readout*

An 80 µL sample containing digoxin spiked into pooled human serum (Innovative Research Inc, Novi, MI) was mixed with 4 µL of anti-digoxin PtNPs and 16 µL of running buffer (1% w/w 10 kDa polyvinylpyrrolidone, 0.1 % BSA, 0.1% casein, and 0.1% Tween 20 in 10 mM potassium phosphate buffer pH, 7.4). This solution was then applied to the sample well of the casing which housed the LFA test strip. After 5 min, 50 µL of chase buffer (0.5% w/w 10 kDa polyvinylpyrrolidone, 0.05 % BSA, 0.05% casein, and 0.05% Tween 20 in 5 mM potassium phosphate buffer pH, 7.4) was applied to the sample well in which the assay was allowed to run for another 5 min. Following this antigen capture/detection step, the pull tab containing the immobilized test strip was removed and inserted into a 3D printed holder above a 96-well plate. This holder positioned the pull tab in the center of the well with the test line region completely submerged in the peroxide incubation solution (100 µL of 4 mM H_2O_2 in 5 mM NaOH) within the well. The 96-well plate with pull tab was placed on a microplate shaker at 600 RPM for 20 min. 20 µL of the peroxide incubation solution was then transferred into a separate 96-well plate containing the GNR etching precursor solution discussed previously in *Section 4.2.2*. After reacting for 10 min, photographs were taken with a Nikon D3400 digital camera in a controlled lighting environment and the UV-Vis spectra were measured using a Synergy H1 Hybrid Multi-mode reader.

4.3. Results and Discussion

4.3.1. Mechanism of the proposed LFA with a quantitative, multicolor readout

In this work, we propose that the lateral-flow immunoassay (LFA) could be combined with platinum nanozymes possessing catalase-like activity and the anisotropic etching of gold nanorods (GNRs) to produce a multicolor readout which is dependent on the concentration of the target analyte digoxin in a human serum sample. This would allow for naked-eye biomarker quantification without the need for electronic readers or complex and expensive laboratory equipment. The general assay procedure and mechanism is detailed in **Figure 4-2**. The serum sample is first mixed with the anti-digoxin PtNPs. The anti-digoxin antibodies conjugated onto the surface of the nanozymes capture any digoxin in the serum sample. Increasing concentrations of digoxin in the serum result in increased capture and thus greater saturation of the antibodies on the nanozyme surface.

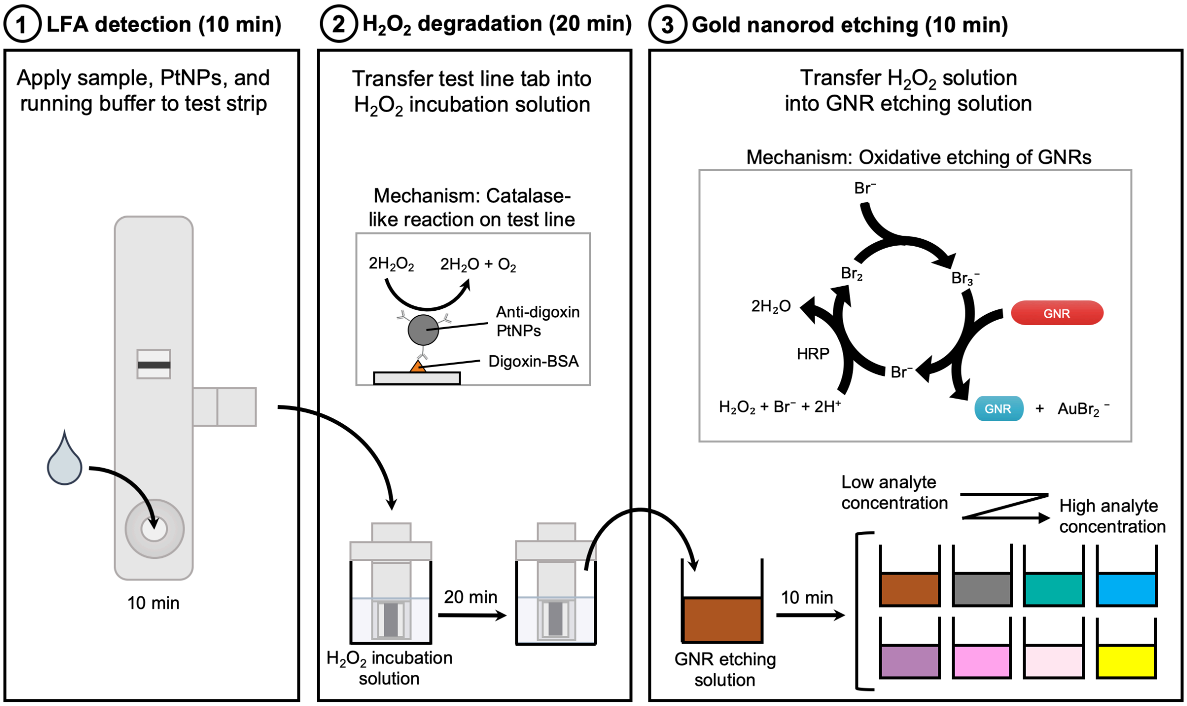

Figure 4-2 Schematic representation of user steps and mechanism for integrating the LFA with GNR etching for digoxin quantification

(1) Serum sample, PtNPs, and running buffer are applied to the LFA test strip, where antigen capture and binding occurs at the test line. (2) Test line is transferred using the pull tab to the incubation solution containing H_2O_2 in NaOH, where the PtNPs bound at the test line catalyze the degradation of H_2O_2. (3) The incubation solution is transferred to the GNR etching solution, where any H_2O_2 remaining oxidizes bromide to produce tribromide, which etches GNRs to produce a quantitative multicolor output.

After the sample is applied to the LFA test strip, it will flow from the sample pad segment to the test line segment and finally into the absorbent pad segment, with the fiberglass flow connector pads bridging the gaps between these pieces (**Figure 4-3**). Because digoxin is a small molecule with very few unique binding epitopes, a competitive assay LFA format was utilized. As the sample flows past the test line that is composed of immobilized digoxin-BSA, the anti-digoxin antibodies on the PtNPs which are not saturated with digoxin from the serum sample will be able to bind to the test line. Thus, a low concentration of digoxin in the serum results in high binding of PtNPs to the test line, while a high concentration of digoxin results in low binding of PtNPs to the test line.

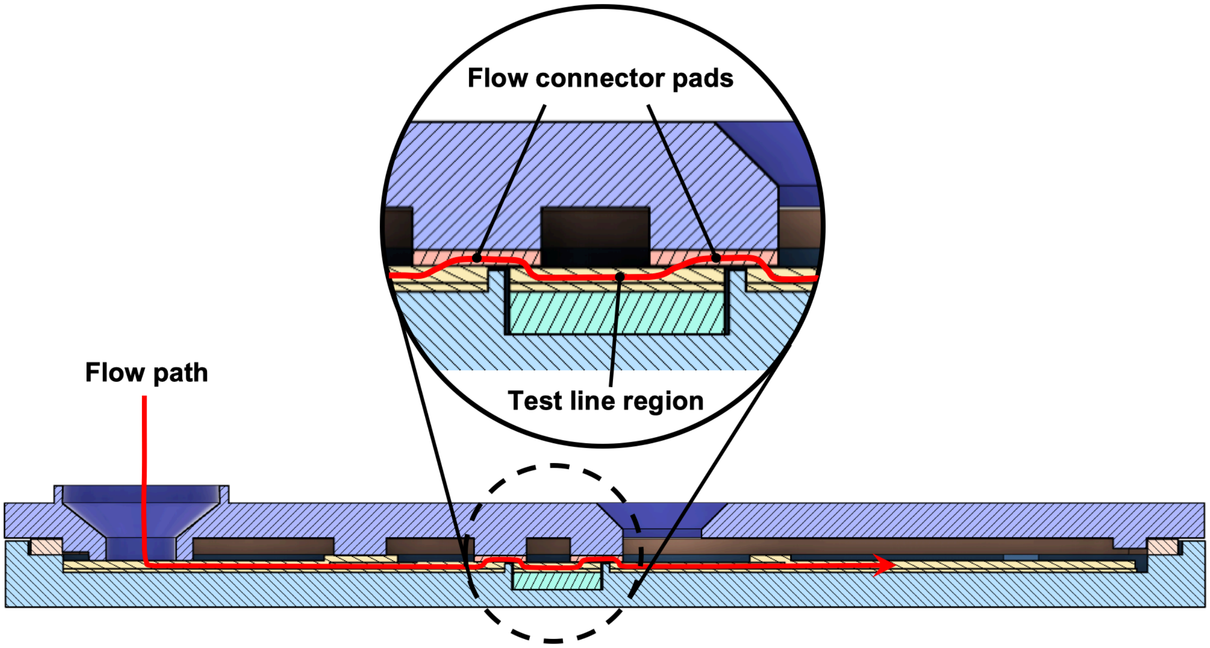

Figure 4-3 Cross-sectional view of the LFA test strip in casing and sample flow path
Liquid is applied to the sample well, where it flows from left to right through the modified LFA strip. The zoomed-in picture shows the fluid flow between segments through the flow connector pads.

The pull tab containing the test line segment is then transferred into a holder above a 96-well plate, where the test line itself is submerged in a hydrogen peroxide incubation solution. It has previously been demonstrated that noble metal nanoparticles such as those composed of gold, silver, platinum and palladium, possess pH-switchable catalytic activities.[117] In acidic conditions, they possess peroxidase-like activities where they catalyze the breakdown of hydrogen peroxide into free radicals which can oxidize chromogenic substrates.[118] In basic conditions, the nanoparticles possess catalase-like activities, where they catalyze the degradation of hydrogen peroxide into water and oxygen.[119] Therefore we chose to use a basic pH hydrogen peroxide solution so that the breakdown of hydrogen peroxide into water and oxygen would be catalyzed by any PtNPs bound to the test line. After this incubation, the concentration of hydrogen peroxide remaining in the solution would be directly related to the initial digoxin concentration in the original serum sample. A low concentration of digoxin results in a high amount of PtNPs bound to the test line, fast degradation of the hydrogen peroxide and thus less peroxide remaining. A high concentration of digoxin on the other hand results in a low amount of PtNPs bound to the test line, slow degradation of hydrogen peroxide and thus, more peroxide remaining.

To convert the hydrogen peroxide concentration of the incubation solution to the final visible multicolor readout, an oxidative GNR etching reaction is utilized. The user would transfer the peroxide solution into a separate suspension containing GNRs, HRP, CTAB, Tween 20, and NaBr in a citrate buffer. The HRP would catalyze the oxidation of bromide ions to molecular bromine (Br_2), which in the presence of excess bromide would be converted the reactive species tribromide. The tribromide ions complexes with CTA^+ micelles and CTA^+ micelles associated with some bromide ions due to strong electrostatic interactions. It has been suggested that this interaction both stabilizes the reactive tribromide ion and also facilitates transport of the tribromide to the surface of the GNRs which are coated with a CTA^+ bilayer.[42] The tribromide will oxidize the gold atoms on the tips of GNRs, resulting in the anisotropic etching and shortening of the gold nanorods. By adding different concentrations of hydrogen peroxide into the GNR etching reaction, the GNRs would be etched to varying degrees, resulting in different sized GNRs being produced. It has been well known that due to localized surface plasmon resonance, the optical properties of GNR suspensions are highly depended on the particle aspect ratio (length/width), allowing for the production of a wide range of different colored suspensions. Ultimately, differences in the initial concentration of digoxin in the serum sample, would result in GNRs being etched to different degrees and therefore produce distinct differences in the visible color of the suspension that are easily interpreted by the naked-eye.

4.3.2. Demonstration of GNR etching for multicolor quantification of hydrogen peroxide

While the oxidative anisotropic etching of GNRs has previously been reported to produce a wide spectrum of visible colors, studies that specifically etch GNRs using hydrogen peroxide and HRP without TMB have reported limited ranges in color production.[45,120] Prior to integrating this reaction with LFA, it was necessary to characterize the importance of each reagent, determine the feasibility of using this reaction to produce a wide color spectrum, and determine the concentration range of hydrogen peroxide necessary.

Initial GNR etching experiments without Tween 20 had inconsistent results due to the precipitation of CTAB out of solution at room temperature. To address this, we evaluated different additives to the reaction mixture for their ability to improve CTAB solubility. Both Tween 20 and TX-114 were found to dramatically improve the solubility of CTAB when introduced at an equal concentration to that of CTAB, with solutions remaining stable at 4 ºC. Additionally, including Tween 20 and TX-114 had a negligible impact on the end color of the GNR etching reaction (not shown).

The importance of other major reaction components was evaluated in **Figure 4-4**. Reaction condition A contained all reaction components except HRP. After 10 min, there was no observed etching, as the color remained red with a longitudinal peak wavelength of 788 nm, which is identical to the original synthesized GNRs. Unexpectedly, reaction condition B, which contained all components except H_2O_2, did result in a small amount of GNR etching indicated by a slightly more brown suspension and the small blue-shift of the longitudinal peak wavelength. We suspect this could be a result of the a HRP active site already being occupied and complexed with a small amount of H_2O_2 from the vendor. Thus upon the introduction of the HRP to the GNR etching suspension without additional H_2O_2, a small amount of reactive tribromide is formed that can etch the GNRs. Condition C did not contain the any NaBr and resulted in substantial etching indicated by the resulting greenish-grey colored suspension and a blue-shifted peak wavelength value of 645 nm. Even though there were no bromide ions added in the form of NaBr, the bromide ions from the CTAB allowed for the generation of the reactive tribromide species which etches the GNRs. Lastly, condition D which contained all assay components resulted in the greatest amount of etching as seen by the blue colored suspension and the lowest peak wavelength for the longitudinal band of 602 nm. Despite both containing 1 mM of H_2O_2, reaction D etched further than reaction C which did not contain additional NaBr. The additional bromide ions from the NaBr allow for the production of a greater amount of tribromide which can ultimately etch the GNRs further.

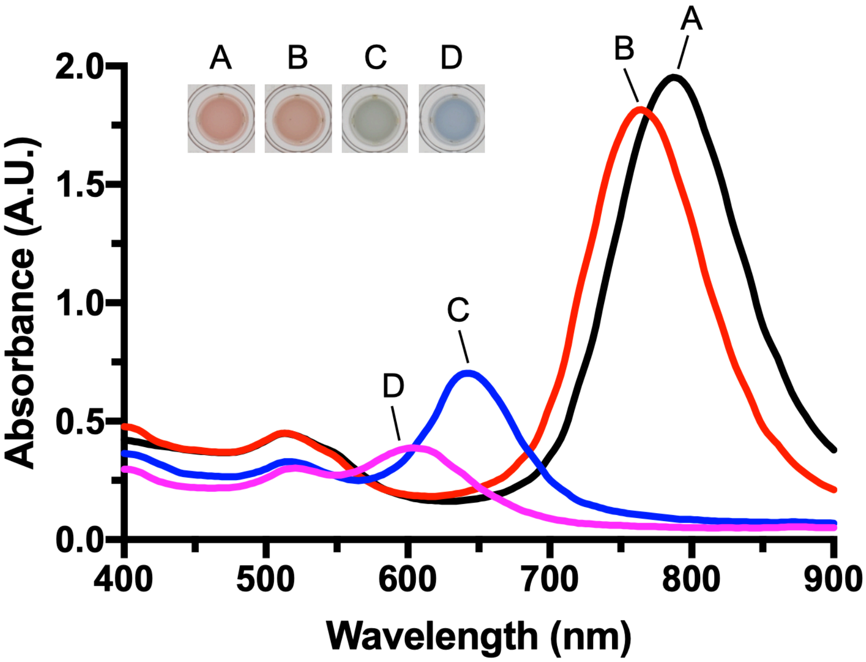

Figure 4-4 Photographs and UV-Vis spectra of GNR etching suspension with different reagents GNR etching reactions were performed for 10 min. Reaction A contains GNR + CTAB + NaBr + H_2O_2. Reaction B contains GNR + CTAB + NaBr + HRP. Reaction C contains GNR + CTAB + HRP + H_2O_2. Reaction D contains GNR + CTAB + NaBr + HRP + H_2O_2.

To determine the full range of colors that could be produced from the GNR etching reaction, the hydrogen peroxide concentration added was varied from 0 to 4 mM. After reacting for 10 min, a wide spectrum of colors was produced (**Figure 4-5**). Our experiment demonstrated that at least 12 different colors could be produced which are easily distinguishable by the naked-eye. The resulting UV-Vis spectra confirmed that the GNRs are being etched, indicated by the progressive blue-shift in the longitudinal plasmon band that corresponds to a decreasing GNR aspect ratio. The change in the longitudinal plasmon band peak wavelength was linear as a function of H_2O_2 concentration until 1.5 mM of H_2O_2 (**Figure 4-6**). The resulting suspensions at 1.5 and 2 mM are pink and also the UV-Vis spectrum no longer has the longitudinal plasmon band that is characteristic of a gold nanorod. It is at this point that the GNRs have become spherical gold nanoparticles and begin to etch evenly from all sides until no nanoparticles are left in the suspension. The yellow color of the solution from etching with 4 mM H_2O_2 can be attributed to the further oxidation of the GNR etching reaction product $AuBr_2^-$ into $AuBr_4^-$, once all GNRs and spherical particles are completely degraded.[44] It is worth noting that the GNR etching reaction is extremely reproducible as shown in **Figure 4-6**, where most error bars are not visible due to being so small.

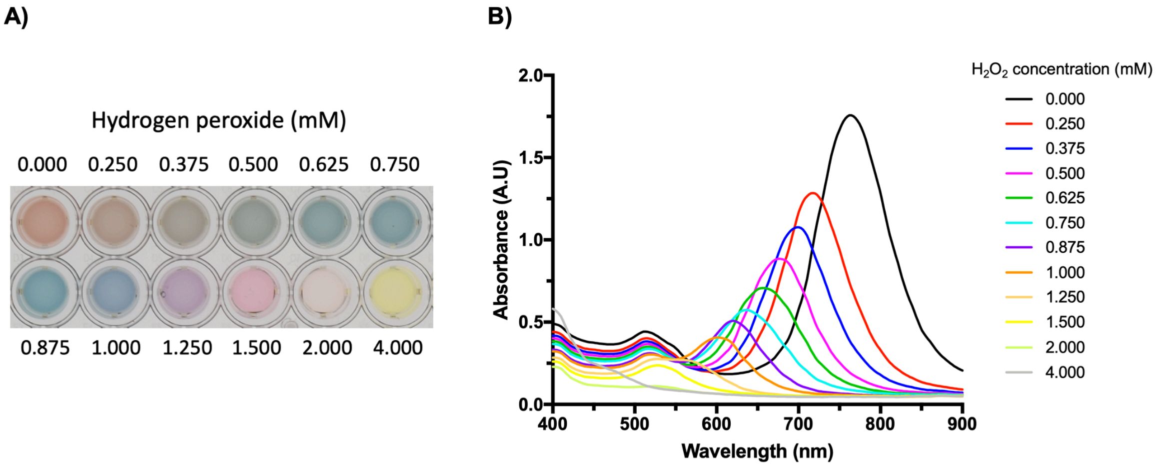

Figure 4-5 Signal generation from hydrogen peroxide induced GNR etching
(A) Photographs and (B) UV-Vis spectra of suspensions resulting from GNR etching reactions in the presence of varying concentrations of H_2O_2.

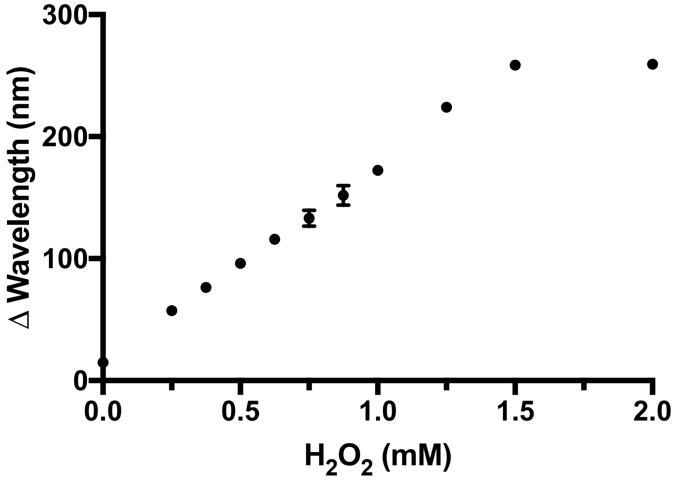

Figure 4-6 Change in peak of the UV-Vis longitudinal wavelength of the suspension from GNR etching
Difference in the peak wavelength value of the longitudinal plasmon band before and after the GNR etching reaction for varying concentrations of H_2O_2. All data presented as mean ± SD (n = 3).

4.3.3. *Quantitative detection of digoxin using the LFA with a multicolor readout*

We then moved on to evaluate whether our proposed assay could produce easily distinguishable colored results with small changes in digoxin concentration within the clinically relevant range of 0.25 to 4 ng/mL. The test lines produced after running the serum samples containing digoxin on the LFA for 10 min are shown in the top of **Figure 4-7**. As expected for a competitive assay format of the LFA, the darkest test line is observed for the negative, and that test line intensity decreases as the concentration of digoxin increases. This indicates that there are differences in the amount of PtNPs bound to each test line for varying concentrations of digoxin, which is required for the peroxide incubation step to produce different amounts of peroxide to ultimately etch GNRs to varying degrees. It is important to note that while most the test lines are distinguishable by intensity, it would be difficult for a user to reliably match the intensity of each line with a concentration of digoxin, especially the lower digoxin concentration range of 0.00-0.50 ng/mL where the test line intensity differences between each condition are minor.

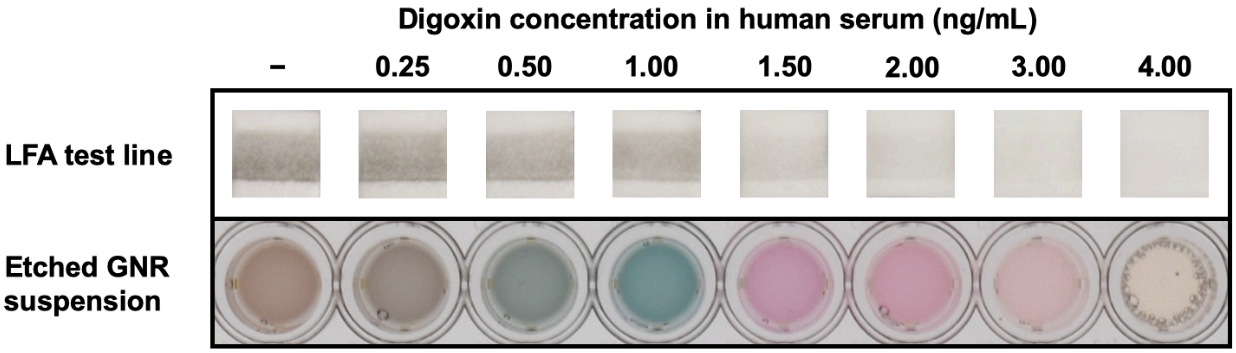

Figure 4-7 LFA test lines and GNR etching results when detecting digoxin in human serum
LFA test line intensity decreases with increase in digoxin concentration. The GNR suspensions resulting from the integrated LFA and GNR etching test show a wide range of distinguishable colors allowing for accurate digoxin quantification.

After running the LFA, the test lines were placed in the peroxide incubation solution for 20 min to degrade the hydrogen peroxide through the catalase-like activity of the PtNPs bound to the test lines. The incubation solution was then transferred into the GNR etching solution and allowed to react for 10 min, where HRP would catalyze the oxidation of bromide into tribromide by the hydrogen peroxide, which would lead to the etching of the GNRs. The resulting GNR suspensions are shown in the bottom of **Figure 4-7**. It can be observed that very distinct and easily distinguishable colors were produced by the GNR etching reaction and the colors produced were dependent on the concentration of digoxin in the serum sample. This is in contrast to interpreting the test lines by intensity, where the visible differences can be slight and may be difficult to interpret quantitatively without the aid of an electronic reader. The color trend produced was also consistent with **Figure 4-5**, where increasing concentrations of hydrogen peroxide added to the GNR etching reaction resulted in the production of GNR suspension colors in the order of brown to blue to pink to yellow. This confirms that the increased amount of PtNPs bound to the test line with the lower digoxin concentrations degraded more of the hydrogen peroxide in the incubation solution when compared to the higher digoxin concentrations. Ultimately, our assay is able to quantitatively detect for digoxin in human serum below, within, and above the therapeutic window. Further, not only can our assay be used to classify samples within these three categories but it also provides more accurate measurements that have the potential to be used to calculate adjustments in dosage for individualized therapy.

This technology could be useful in the quantitative detection of other many other targets besides digoxin. Other therapeutic drug monitoring (TDM) applications that our assay could be adapted to address include the quantitative monitoring of other therapeutic drugs such as levofloxacin for tuberculosis treatment, infliximab for inflammatory bowel diseases, antiepileptic drugs, and immunosuppressants to prevent organ rejection following transplant.[121] Besides TDM, we believe the multicolor, quantitative assay developed here could find applications in environmental contaminant testing.[122] We acknowledge that this technique in its current stage is more complex than the conventional LFA because it requires additional liquid handling steps, which could limit its use in an at home or in-field setting. However, it could serve to bridge the gap between the simple one step, qualitative LFA and the more complex quantitative, plasmonic ELISA. It is also the starting point for future work in the development of a fully paper-based version of this technology which will minimize user steps and eliminate the need for any laboratory equipment such as pipettes or microplate shakers.

4.4. Conclusion

In summary, we have developed a new method for the quantification of digoxin using the LFA combined with a gold nanorod etching reaction. To our knowledge, this is the first integration of the LFA with a gold nanorod etching reaction, as well as the first quantitative LFA with a multicolor readout that is dependent on the initial analyte concentration. We believe this work serves as a starting point for the development of a new generation of highly quantitative, lateral-flow assays which can be operated without the need for expensive laboratory equipment and electronic devices. Ultimately, this could lead to more effective patient management and treatment in resource-limited settings.

Chapter 5. Automation of Biomarker Preconcentration, Capture, and Signal Enhancement on Paper-Based Devices

5.1. Introduction

Infectious diseases are among the leading causes of deaths in developing countries. Many of these deaths could be prevented if the diseases were detected in their early stages, allowing for better patient management, faster administration of appropriate treatment, and more effective outbreak prevention.[1,123] However, the current gold standard diagnostic technologies capable of providing rapid and accurate detection are not suitable for use in developing countries which lack access to electricity, laboratory equipment, and trained personnel. The World Health Organization has provided the ASSURED criteria to aid in the development of point-of-care (POC) diagnostic tests specifically for use in developing countries. It states that such tests must be affordable, sensitive, specific, user-friendly, rapid and robust, equipment-free, and deliverable to the end-user.[1] Recently, paper has emerged as an excellent material for developing POC devices due to its low cost, ease of functionalization, and ability to passively transport fluid via capillary flow.[5] One common paper-based device is the lateral-flow immunoassay (LFA), a rapid antibody-based test that has achieved widespread commercial success in the form of the over-the-counter pregnancy test. Despite this success, the LFA does suffer from having a low sensitivity relative to laboratory-based tests, such as the enzyme-linked immunosorbent assay and the polymerase chain reaction, which limits its effectiveness in the detection of infectious diseases.[3]

To improve the sensitivity of the LFA, our group previously developed equipment-free methods which utilize liquid-liquid extraction techniques to concentrate the target biomarker prior to detection. This was achieved by using aqueous two-phase systems (ATPSs), which separate into two distinct phases, where the target biomarker would partition extremely into one of those phases, effectively concentrating it. The first method we developed required the ATPS to macroscopically separate, followed by the manual extraction of the phase containing the concentrated biomarker and then application to the LFA. While effective at improving the LFA detection limit by 10-fold for both large viruses[55,57] and small protein targets,[56,58] this approach was limited by its long time-to-result and requirement of multiple user-steps. To address these limitations, a second method was developed which involved the direct application of a mixed ATPS to a paper device. Our lab discovered that a well-mixed ATPS rapidly separated into its macroscopic phases as it flowed through a paper membrane, producing distinct leading and lagging phases. Integration of this ATPS separation on paper phenomenon with the LFA allowed for simultaneous analyte concentration and detection, while reducing the overall time-to-result.[48,49]

In addition to biomarker preconcentration, another equipment-free method to improve the sensitivity of the LFA involves chemical signal enhancement. Chemical signal enhancement typically requires the user to manually apply enhancement reagents to the LFA test strip in a sequential manner. Although these methods are effective at improving LFA sensitivity, the requirement of multiple user steps renders them not ideal for a POC device.[63,68] To eliminate the need for multiple user steps, the Yager group developed 2D paper networks, which utilize carefully designed 2D paper geometries to control fluid flow and perform timed delivery of reagents to a detection zone.[124–127] Other paper-based automation techniques include the use of controlled porosity,[128] paper shunts,[129] valves,[130–133] and dissolvable sugar delays.[134,135] While successful at automating enhancement reactions, many of the devices using these techniques have thus far demonstrated limited improvements in detection limit over their unenhanced counterparts. Additionally, many of these devices are significantly more complex than the conventional LFA test strip, which could increase cost and limit their adaptability for high volume manufacturing.[71]

In this work, we introduce a new technique to automate both biomarker concentration and signal enhancement which is easy to use, low in cost, tunable without complex changes in device design, and easily manufacturable. We have called this technique the **A**TPS-automated **C**oncentration and **E**nhancement of the **L**ateral-**F**low immuno**A**ssay (ACE-LFA). The ACE-LFA takes advantage of both the selective partitioning of biomarkers and reagent molecules between the phases of the ATPS, as well as our lab's ATPS separation on paper technology to sequentially deliver the concentrated target biomarker and signal enhancement reagents across the LFA test strip. We demonstrated that the delivery time of reagents is tunable by simply changing the initial composition of the ATPS. A mathematical model that predicts the delivery time was also developed, which can aid in assay design.

Using our ACE-LFA technology we demonstrated the ability to automate two different signal enhancement reaction on the LFA: (1) An enzyme-based reaction utilizing alkaline phosphatase (ALP) and the colorimetric substrate nitro blue tetrazolium/5-bromo-4-chloro-3-indolyl-phosphate (NBT/BCIP) when detecting for the model bacteria inactivated *Chlamydia trachomatis* (CT), and (2) a peroxidase-mimicking nanozyme-based reaction utilizing the platinum-coated gold nanoparticles, hydrogen peroxide, and the colorimetric substrate 3,3',5,5'-tetramethylbenzidine (TMB) when detecting for the model bacteria *Escherichia coli* (*E. coli*). In each of these applications, the automation of biomarker preconcentration and signal enhancement ultimately resulted in up to a 30-fold improvement in detection limit over the conventional LFA. To our knowledge, this is the first reported use of the ATPS to automate sequential reagent delivery, as well as the first integration of automated biomarker concentration, capture, and signal enhancement on a paper-based device.

5.2. Theoretical Modeling

5.2.1. Overview of modeling approach

Capillary imbibition in porous media, such as paper membranes, has been modeled using a variety of approaches that vary significantly in complexity. Capillary-based models, which treat the porous media as a bundle of capillaries with an equivalent radius, have often been used to provide a way to develop simple analytical expressions for one-dimensional flow. The Lucas-Washburn equation, based on the Hagen-Poiseuille equation and its assumptions, is the most common capillary-based model for predicting flows of fluids in porous media, including paper.[71,136] It has been shown to be reasonably predictive for one-dimensional, single phase, capillary-driven laminar flow of a Newtonian fluid with a non-limiting source.

Here, we have developed our own piecewise, capillary-based model to predict the behavior of two immiscible phases flowing back-to-back through a paper strip with a 3D paper wick. In this model, a bundle containing n_s capillaries of radius R_s represents the long paper strip. An additional bundle containing n_w capillaries of radius R_w and length $l_{w,tot}$ is incorporated before $z = 0$, which represents the 3D paper wick. We have allowed for the effective radius to be different between the strip and the wick, because previous research has demonstrated that fluid flows faster through layered sheets of paper when compared to a single sheet as a result of the additional space between the sheets increasing the effective radius in the layered setup.[137] The flow is assumed to be fully developed throughout the entire geometry and time frame, thus allowing for an instantaneous velocity change between the capillaries representing the paper strip and the 3D paper wick. This problem was split into two different stages of flow; stage I flow occurs when only a single phase is present in the long capillary, and stage II flow corresponds to the situation where two phases are present in the long capillary (**Figure 5-1**).

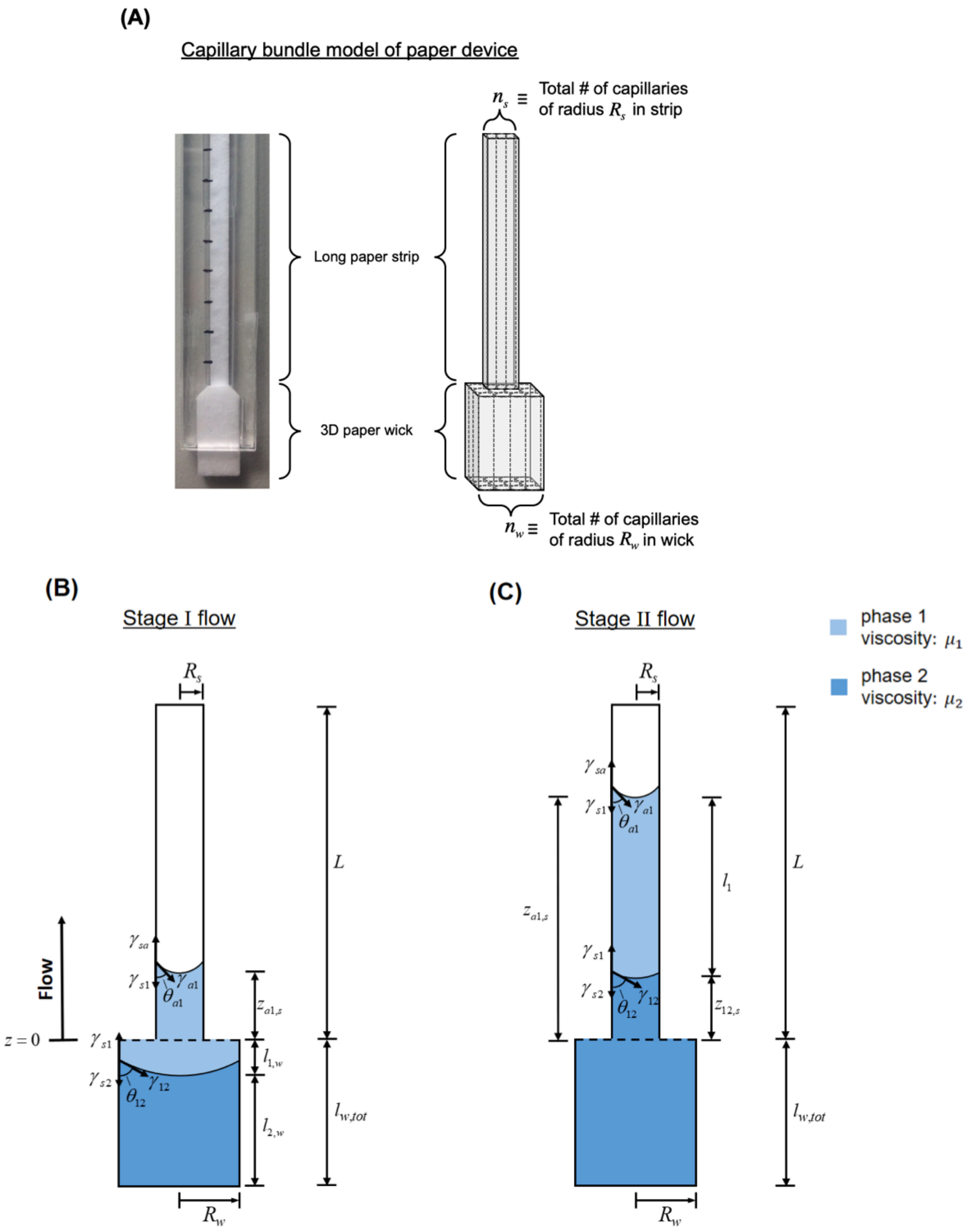

Figure 5-1 Schematic of modeling two-phase flow in paper as bundles of capillaries.
(A) Overview of geometric breakdown for capillary bundle modeling with strip and wick. (B) Stage I flow for a single strip and wick capillary. (C) Stage II flow for a single strip and wick capillary.

5.2.2. Derivation of the governing equation for stage I flow

To derive the governing equation for stage I flow, we performed a force balance on the capillary bundles shown in **Figure 5-1**. The change in momentum, i.e., the mass m multiplied by the fluid velocity in the strip $\frac{dz_{s,I}}{dt}$ is balanced by the capillary driving force $F_{cap,I}$, the external hydrostatic pressure $F_{ext-press,I}$, the force of gravity $F_{grav,I}$, and the total viscous force $F_{visc,total,I}$:

$$\frac{d}{dt}\left(m\frac{dz_{s,I}}{dt}\right)=F_{cap,I}+F_{ext-press,I}-F_{grav,I}-F_{visc,total,I} \tag{1}$$

Assuming a negligible effect of the change in momentum, hydrostatic pressure, and gravity leads to:

$$0=F_{cap,I}-F_{visc,total,I} \tag{2}$$

The total viscous force is calculated in Eq. (3) by adding together the viscous force contributions of each phase α, where $\alpha=1 \text{ or } 2$, in each capillary bundle δ, where $\delta=s$ represents the strip and $\delta=w$ represents the wick.

$$F_{visc,total,I}=\sum_{\alpha}\sum_{\delta}F_{visc,\alpha,\delta,I} \tag{3}$$

which leads to:

$$F_{visc,total,I}=F_{visc,1,s,I}+F_{visc,1,w,I}+F_{visc,2,w,I} \tag{4}$$

To calculate $F_{visc,1,s,I}$, we assume a Hagen-Poiseuille velocity profile, $u_{s,I}(r)$, across a capillary of radius R_s representing the paper strip, where $\frac{dz_{s,I}}{dt}$ is the average fluid velocity within the capillary:

$$u_{s,I}(r)=2\frac{dz_{s,I}}{dt}\left(1-\frac{r^2}{R_s^{\,2}}\right) \tag{5}$$

This velocity profile was substituted into an expression for the viscous shear stress, shown below in Eq. (6), where the viscosity of phase 1 is denoted as μ_1:

$$-\mu_1 \left. \frac{du_{s,I}}{dr} \right|_{r=R_s} = \frac{4\mu_1 \frac{dz_{s,I}}{dt}}{R_s} \tag{6}$$

Equation (6) was then multiplied by the number of capillaries in the strip n_s and the surface area of the interface between phase 1 and the capillary that the viscous shear stress acts upon, $2\pi R_s z_{1a,s}$ to yield:

$$F_{visc,1,s,I} = 2\pi R_s z_{a1,s} \left(\frac{4\mu_1 \frac{dz_{s,I}}{dt}}{R_s} \right) n_s \tag{7}$$

To calculate $F_{visc,1,w,I}$ and $F_{visc,2,w,I}$, we also assumed a Hagen-Poiseuille velocity profile except now across a capillary of radius R_w which represents the wick with an average velocity of $\frac{dz_{w,I}}{dt}$:

$$u_{w,I}\left(r\right) = 2\frac{dz_{w,I}}{dt}\left(1 - \frac{r^2}{R_w^{\ 2}}\right) \tag{8}$$

To conserve the volumetric flow rate, the fluid velocities in the strip and wick are related to one another by Eqs. (9) and (10):

$$\frac{dz_{s,I}}{dt} c = \frac{dz_{w,I}}{dt} \tag{9}$$

$$c = \frac{\pi R_s^{\ 2} n_s}{\pi R_w^{\ 2} n_w} \tag{10}$$

where c is equal to the ratio of the available cross-sectional areas normal to the direction of flow in the capillaries representing the paper strip to that of the 3D wick.

The velocity profile was substituted into an expression for the viscous shear stress for each phase α in the wick:

$$-\mu_\alpha \left.\frac{du_{w,I}}{dr}\right|_{r=R_w} = \frac{4\mu_\alpha \frac{dz_{s,I}}{dt} c}{R_w} \tag{11}$$

Equation (11) was then multiplied by the number of capillaries in the wick n_w and the surface area of the interface between the respective phase and the cylindrical capillary that the viscous shear stress acts upon to obtain the following expressions:

$$F_{visc,1,w,I} = 2\pi R_w l_{1,w} \left(\frac{4\mu_1 \frac{dz_{s,I}}{dt} c}{R_w} \right) n_w \tag{12}$$

$$F_{visc,2,w,I} = 2\pi R_w l_{2,w} \left(\frac{4\mu_2 \frac{dz_{s,I}}{dt} c}{R_w} \right) n_w \tag{13}$$

where the lengths of phase 1 and phase 2 in the wick are denoted as $l_{1,w}$ and $l_{2,w}$, respectively. They can be calculated as:

$$l_{1,w} = c\left(l_1 - z_{a1,s}\right) \tag{14}$$

$$l_{2,w} = \left(l_{w,tot} - l_1 c\right) + z_{a1,s} c \tag{15}$$

where l_1 is the maximum length of phase 1 in the long strip after it has completely flowed out of the 3D wick and $l_{w,tot}$ is the distance from the top of the 3D wick to the fluid source. $l_{1,w}$ and $l_{2,w}$ are functions of $z_{a1,s}$, because as phase 1 flows up the strip, increasing $z_{a1,s}$, the amount of phase 1 remaining in the wick will decrease while the amount of phase 2 in the wick increases. Additionally, because the flow is assumed to be fully developed, during stage I flow:

$$\frac{dz_{s,I}}{dt} = \frac{dz_{a1,s}}{dt} \tag{16}$$

where $\frac{dz_{a1,s}}{dt}$ represents the average velocity that the air - phase 1 interface moves along the capillary of radius R_s.

The capillary driving force was obtained using the interfacial free energy method, in which the total interfacial Gibbs free energy of the system is given by:

$$G_{T,I} = \gamma_{sa} A_{s_s a,I} n_s + \gamma_{a1} A_{a1,I} n_s + \gamma_{s1} A_{s_s 1,I} n_s + \gamma_{s1} A_{s_w 1,I} n_w + \gamma_{s2} A_{s_w 2,I} n_w + \gamma_{12} A_{12,I} n_w \tag{17}$$

where γ_{sa}, γ_{a1}, γ_{s1}, γ_{s2}, and γ_{12} are the surface or interfacial tensions (free energies per area) of the solid - air interface, air - phase 1 interface, solid - phase 1 interface, solid - phase 2 interface, and phase 1 - phase 2 interface, respectively. $A_{s_s a,I}$, $A_{a1,I}$, $A_{s_s 1,I}$, $A_{s_w 1,I}$, $A_{s_w 2,I}$, and $A_{12,I}$ represent the stage I interfacial areas per capillary of the solid - air interface, air - phase 1 interface, solid - phase 1 interface in the strip, solid - phase 1 interface in the wick, solid - phase 2 interface in the wick, and phase 1 - phase 2 interface, respectively.

The surface and interfacial tensions can be related to the contact angles through Young's equation:

$$\gamma_{sa} = \gamma_{a1} \cos(\theta_{a1}) + \gamma_{s1} \tag{18}$$

$$\gamma_{s2} = \gamma_{s1} - \gamma_{12} \cos(\theta_{12}) \tag{19}$$

where θ_{a1} is the contact angle between the air - phase 1 surface tension and the solid - phase 1 interfacial tension, and θ_{12} is the contact angle between the phase 1 - phase 2 interfacial tension and the solid - phase 2 interfacial tension. Substituting Eqs. (18) and (19) into Eq. (17) yields:

$$G_{T,I} = \gamma_{s1} \left(A_{s_s a,I} n_s + A_{s_s 1,I} n_s + A_{s_w 1,I} n_w + A_{s_w 2,I} n_w \right) + \ldots$$

$$\ldots \gamma_{a1} \left(\cos(\theta_{a1}) A_{s_s a,I} n_s + A_{a1,I} n_s \right) + \gamma_{12} \left(A_{12,I} n_w - \cos(\theta_{12}) A_{s_w 2,I} n_w \right) \tag{20}$$

Note that $\gamma_{s1}\left(A_{s_s a,I}n_s + A_{s_s 1,I}n_s + A_{s_w 1,I}n_w + A_{s_w 2,I}n_w\right)$ is constant because the total area of the system shown below in Eq. (21) is constant.

$$A_{total,I} = A_{s_s a,I}n_s + A_{s_s 1,I}n_s + A_{s_w 1,I}n_w + A_{s_w 2,I}n_w \tag{21}$$

Additionally, given:

$$A_{s_s a,I}n_s = 2\pi R_s\left(L - l_{w,tot} - z_{a1,s}\right)n_s \tag{22}$$

$$A_{s_w 2,I}n_w = 2\pi R_w\left(\left(l_{w,tot} - l_1 c\right) + z_{a1,s}c\right)n_w \tag{23}$$

and assuming that

$$\frac{dA_{a1,I}}{dz_{a1,s}} = 0,\ \frac{dA_{12,I}}{dz_{a1,s}} = 0,\ \frac{d\cos(\theta_{a1})}{dz_{a1,s}} = 0,\ \frac{d\cos(\theta_{12})}{dz_{a1,s}} = 0,$$

the capillary driving force for stage I can be expressed as:

$$F_{cap,I} = -\frac{dG_{T,I}}{dz_{a1,s}} = -\left(-2\pi R_s\gamma_{a1}\cos(\theta_{a1})n_s - 2\pi R_w\gamma_{12}\cos(\theta_{12})n_w c\right) \tag{24}$$

since the force is equal to the negative gradient of the potential energy. For a typical aqueous two-phase system, $\gamma_{a1} >> \gamma_{12}$ and therefore the capillary driving force can be simplified to:

$$F_{cap,I} = 2\pi R_s\gamma_{a1}\cos(\theta_{a1})n_s \tag{25}$$

Substituting Eqs. (7), (12), (13), (16), and (25) into Eqs. (2) and (4) results in

$$0 = 2\pi R_s \gamma_{a1} \cos(\theta_{a1}) n_s - 2\pi R_s z_{a1,s} \left(\frac{4\mu_1 \frac{dz_{a1,s}}{dt}}{R_s} \right) n_s \ldots$$

$$\ldots - 2\pi R_w c\left(l_1 - z_{a1,s}\right) \left(\frac{4\mu_1 \frac{dz_{a1,s}}{dt} c}{R_w} \right) n_w - 2\pi R_w \left[\left(l_{w,tot} - l_1 c\right) + z_{a1,s} c \right] \left(\frac{4\mu_2 \frac{dz_{a1,s}}{dt} c}{R_w} \right) n_w \tag{26}$$

which simplifies to:

$$R_s \gamma_{a1} \cos(\theta_{a1}) n_s dt = 4\mu_1 z_{a1,s} n_s dz_{1,s} + 4\mu_1 \left(l_1 - z_{1a,s}\right) c^2 n_w dz_{a1,s} + 4\mu_2 \left[\left(l_{w,tot} - l_1 c\right) + z_{a1,s} c \right] c n_w dz_{a1,s} \tag{27}$$

Integration of Eq. (27) yields:

$$R_s \gamma_{a1} \cos(\theta_{a1}) n_s t = 4\mu_1 \frac{{z_{a1,s}}^2}{2} n_s + 4\mu_1 \left(l_1 z_{a1,s} - \frac{{z_{a1,s}}^2}{2} \right) c^2 n_w + 4\mu_2 \left[\left(l_{w,tot} - l_1 c\right) z_{a1,s} + \frac{{z_{a1,s}}^2}{2} c \right] c n_w + B_1 \tag{28}$$

where B_1 is a constant of integration. Application of the initial condition $t(z_{a1,s} = 0) = 0$ results in $B_1 = 0$, and after solving for time t, Eq. (28) can be rearranged to:

$$t = \frac{4\mu_1 \frac{{z_{a1,s}}^2}{2} n_s + 4\mu_1 \left(l_1 z_{a1,s} - \frac{{z_{a1,s}}^2}{2} \right) c^2 n_w + 4\mu_2 \left[\left(l_{w,tot} - l_1 c\right) z_{a1,s} + \frac{{z_{a1,s}}^2}{2} c \right] c n_w}{R_s \gamma_{a1} \cos(\theta_{a1}) n_s} \tag{29}$$

which describes the time it takes for the air - phase 1 interface to reach a distance $z_{a1,s}$ and is valid for $0 \le z_{a1,s} \le l_1$ which corresponds to time $0 \le t \le t^*$ where t^* is equal to:

$$t^* = t\left(z_{a1,s} = l_1\right) = \frac{4\mu_1 \frac{l_1^2}{2} n_s + 4\mu_1 \frac{l_1^2}{2} c^2 n_w + 4\mu_2 \left(l_{w,tot} l_1 - \frac{l_1^2}{2} c \right) c n_w}{R_s \gamma_{a1} \cos(\theta_{a1}) n_s} \tag{30}$$

At time $t = t^*$, stage I flow ends and stage II flow begins.

5.2.3. Derivation of the governing equation for stage II flow

To derive the governing equation for stage II flow, we performed a similar force balance. The change in momentum, i.e., the mass m multiplied by the fluid velocity $\frac{dz_{s,II}}{dt}$ in the paper strip, is balanced by the capillary driving force $F_{cap,II}$, the external hydrostatic pressure $F_{ext-press,II}$, the force of gravity $F_{grav,II}$, and the viscous force $F_{visc,total,II}$.

$$\frac{d}{dt}\left(m\frac{dz_{s,II}}{dt} \right) = F_{cap,II} + F_{ext-press,II} - F_{grav,II} - F_{visc,total,II} \tag{31}$$

Assuming a negligible effect of the change in momentum, hydrostatic pressure, and gravity leads to:

$$0 = F_{cap,II} - F_{visc,total,II} \tag{32}$$

The total viscous force is calculated in Eq. (33) by adding together the viscous force contributions of each phase α, where $\alpha = 1$ or 2, in each capillary bundle δ, where $\delta = s$ represents the strip and $\delta = w$ represents the wick.

$$F_{visc,total,II} = \sum_{\alpha}\sum_{\delta} F_{visc,\alpha,\delta,II} \tag{33}$$

which leads to:

$$F_{visc,total,II} = F_{visc,1,s,II} + F_{visc,2,s,II} + F_{visc,2,w,II} \tag{34}$$

For $F_{visc,1,s,II}$ and $F_{visc,2,s,II}$, we assume a Hagen-Poiseuille velocity profile across a capillary of radius R_s:

$$u_{s,II}\left(r\right)=2\frac{dz_{s,II}}{dt}\left(1-\frac{r^2}{R_s{}^2}\right) \tag{35}$$

This velocity profile was substituted into an expression for the viscous shear stress for each phase α in the strip:

$$-\mu_\alpha \frac{du_{s,II}}{dr}\bigg|_{r=R_s}=\frac{4\mu_\alpha \frac{dz_{s,II}}{dt}}{R_s} \tag{36}$$

The shear stress for each phase is then multiplied by the number of capillaries in the strip, n_s, and the surface area of the interface between the respective phase and the capillary that the viscous shear stress acts upon to yield Eqs. (37) and (38):

$$F_{visc,1,s,II}=2\pi R_s l_1\left(\frac{4\mu_1 \frac{dz_{s,II}}{dt}}{R_s}\right)n_s \tag{37}$$

$$F_{visc,2,s,II}=2\pi R_s z_{12,s}\left(\frac{4\mu_2 \frac{dz_{s,II}}{dt}}{R_s}\right)n_s \tag{38}$$

For $F_{visc,2,w,II}$, we also assumed a Hagen-Poiseuille flow velocity profile except now across a capillary of radius R_w with a velocity of the fluid within the 3D wick, $\frac{dz_{w,II}}{dt}$:

$$u_{w,II}\left(r\right)=2\frac{dz_{w,II}}{dt}\left(1-\frac{r^2}{R_w{}^2}\right) \tag{39}$$

To conserve volumetric flow rate, the fluid velocities in the strip and wick are related to one another by Eqs. (40) and (41):

$$\frac{dz_{s,II}}{dt}c = \frac{dz_{w,II}}{dt} \tag{40}$$

$$c = \frac{\pi R_s^{\,2} n_s}{\pi R_w^{\,2} n_w} \tag{41}$$

where c is equal to the ratio of the available cross-sectional areas normal to the direction of flow in the strip to that of the 3D wick. After combining Eqs. (39) and (40), the resulting velocity profile was substituted into an expression for the viscous shear stress for phase 2 in the wick:

$$-\mu_2 \left.\frac{du_{w,II}}{dr}\right|_{r=R_w} = \frac{4\mu_2 \dfrac{dz_{s,II}}{dt} c}{R_w} \tag{42}$$

Equation (42) was then multiplied by the number of capillaries in the wick, n_w, and the surface area of the interface between phase 2 and the cylindrical capillary that the viscous shear stress acts upon to yield Eq. (43):

$$F_{visc,2,w,II} = 2\pi R_w l_{w,tot} \left(\frac{4\mu_2 \dfrac{dz_{s,II}}{dt} c}{R_w} \right) n_w \tag{43}$$

Additionally, because the flow is assumed to be fully developed, during stage II flow:

$$\frac{dz_{s,II}}{dt} = \frac{dz_{12,s}}{dt} = \frac{dz_{a1,s}}{dt} \tag{44}$$

where $\frac{dz_{12,s}}{dt}$ represents the average velocity that the phase 1 - phase 2 interface moves along the capillary of radius R_s.

The capillary driving force was obtained using the interfacial free energy method, in which the total interfacial Gibbs free energy of the system is given by:

$$G_{T,II} = \gamma_{sa} A_{s_s a,II} n_s + \gamma_{a1} A_{a1,II} n_s + \gamma_{s1} A_{s_s 1,II} n_s + \gamma_{s2} A_{s_s 2,II} n_s + \gamma_{12} A_{12,II} n_s + \gamma_{s2} A_{s_w 2,II} n_w \tag{45}$$

where γ_{sa}, γ_{a1}, γ_{s1}, γ_{s2}, and γ_{12} are the surface or interfacial tensions (free energies per area) of the solid - air interface, air - phase 1 interface, solid - phase 1 interface, solid - phase 2 interface, and phase 1 - phase 2 interface, respectively. $A_{s_s a,II}$, $A_{a1,II}$, $A_{s_s 1,II}$, $A_{s_s 2,II}$, $A_{12,II}$, and $A_{s_w 2,II}$ represent the stage II interfacial areas per capillary of the solid - air interface, air - phase 1 interface, solid - phase 1 interface in the strip, solid - phase 2 interface in the strip, phase 1 - phase 2 interface, and solid - phase 2 interface in the wick, respectively.

The surface and interfacial tensions can be related to the contact angles through Young's equation in Eqs. (18) and (19), which when substituted into Eq. (45) yields:

$$G_{T,II} = \gamma_{s1} \left(A_{s_s a,II} n_s + A_{s_s 1,II} n_s + A_{s_s 2,II} n_s + A_{s_w 2,II} n_w \right) \ldots$$

$$\ldots + \gamma_{a1} \left(\cos(\theta_{a1}) A_{s_s a,II} n_s + A_{a1,II} n_s \right) + \gamma_{12} \left(A_{12,II} n_s - \cos(\theta_{12}) A_{s_s 2,II} n_s - \cos(\theta_{12}) A_{s_w 2,II} n_w \right) \tag{46}$$

Note that $\gamma_{s1} \left(A_{s_s a,II} n_s + A_{s_s 1,II} n_s + A_{s_s 2,II} n_s + A_{s_w 2,II} n_w \right)$ is constant because the total area shown below in Eq. (47) is constant.

$$A_{total,II} = A_{s_s a,II} n_s + A_{s_s 1,II} n_s + A_{s_s 2,II} n_s + A_{s_w 2,II} n_w \tag{47}$$

Additionally, given:

$$A_{s_s a,II} n_s = 2\pi R_s \left(L - l_{w,tot} - l_1 - z_{12,s} \right) n_s \tag{48}$$

$$A_{s_s 2,II} n_s = 2\pi R_s z_{12,s} n_s \tag{49}$$

and assuming that

$$\frac{dA_{a1,II}}{dz_{12,s}} = 0,\ \frac{dA_{12,II}}{dz_{12,s}} = 0,\ \frac{dA_{s_w 2,II}}{dz_{12,s}} = 0,\ \frac{d\cos(\theta_{a1})}{dz_{12,s}} = 0,\ \frac{d\cos(\theta_{12})}{dz_{12,s}} = 0,$$

the capillary driving force for stage II can be expressed as:

$$F_{cap,II} = -\frac{dG_{T,II}}{dz_{12,s}} = 2\pi R_s \gamma_{a1} \cos(\theta_{a1}) n_s + 2\pi R_s \gamma_{12} \cos(\theta_{12}) n_s \tag{50}$$

since the force is equal to the negative gradient of the potential energy. For a typical aqueous two-phase system, $\gamma_{a1} >> \gamma_{12}$ and therefore the capillary driving force can be simplified to:

$$F_{cap,II} = 2\pi R_s \gamma_{a1} \cos(\theta_{a1}) n_s \tag{51}$$

Substituting Eqs. (37), (38), (43), and (51) into Eqs. (32) and (34) yields:

$$0 = 2\pi R_s \gamma_{a1} \cos(\theta_{a1}) n_s - 2\pi R_s l_1 \left(\frac{4\mu_1 \frac{dz_{12,s}}{dt}}{R_s} \right) n_s - 2\pi R_s z_{12,s} \left(\frac{4\mu_2 \frac{dz_{12,s}}{dt}}{R_s} \right) n_s - 2\pi R_w l_{w,tot} \left(\frac{4\mu_2 \frac{dz_{12,s}}{dt} c}{R_w} \right) n_w \tag{52}$$

which simplifies to:

$$R_s \gamma_{a1} \cos(\theta_{a1}) n_s dt = 4\mu_1 l_1 n_s dz_{12,s} + 4\mu_2 z_{12,s} n_s dz_{12,s} + 4\mu_2 l_{w,tot} c n_w dz_{12,s} \tag{53}$$

Integration of Eq. (53) yields:

$$R_s \gamma_{a1} \cos(\theta_{a1}) n_s t = 4\mu_1 l_1 n_s z_{12,s} + 4\mu_2 \frac{z_{12,s}^{\ 2}}{2} n_s + 4\mu_2 l_{w,tot} c n_w z_{12,s} + B_2 \tag{54}$$

where B_2 is a constant of integration. Recall that stage II begins at time $t = t^*$ which is when stage I flow ends. Application of the initial condition for stage II flow $t(z_{12,s} = 0) = t^*$ yields:

$$B_2 = 4\mu_1 \frac{l_1^2}{2} n_s + 4\mu_1 \frac{l_1^2}{2} c^2 n_w + 4\mu_2 \left(l_{w,tot} l_1 - \frac{l_1^2}{2} c \right) c n_w \tag{55}$$

Combination and rearrangement of Eqs. (54) and (55) yield:

$$t = \frac{4\mu_1 l_1 n_s z_{12,s} + 4\mu_2 \frac{z_{12,s}^{\;2}}{2} n_s + 4\mu_2 l_{w,tot} c n_w z_{12,s} + 4\mu_1 \frac{l_1^2}{2} n_s + 4\mu_1 \frac{l_1^2}{2} c^2 n_w + 4\mu_2 \left(l_{w,tot} l_1 - \frac{l_1^2}{2} c \right) c n_w}{R_s \gamma_{a1} \cos(\theta_{a1}) n_s} \tag{56}$$

which predicts the time it takes for the phase 1 - phase 2 interface to reach a distance $z_{12,s}$. Similarly, the time it takes for the air - phase 1 interface to reach a distance $z_{a1,s}$ during stage II flow can be calculated by substituting $z_{a1,s} - l_1$ into $z_{12,s}$ in Eq. (56) to yield:

$$t = \frac{4\mu_1 l_1 n_s (z_{a1,s} - l_1) + 4\mu_2 \frac{(z_{a1,s} - l_1)^2}{2} n_s + 4\mu_2 l_{w,tot} c n_w (z_{a1,s} - l_1) + 4\mu_1 \frac{l_1^2}{2} n_s + 4\mu_1 \frac{l_1^2}{2} c^2 n_w + 4\mu_2 \left(l_{w,tot} l_1 - \frac{l_1^2}{2} c \right) c n_w}{R_s \gamma_{a1} \cos(\theta_{a1}) n_s}$$

(57)

Equations (56) and (57) are valid when $z_{a1,s} \geq l_1$ and $z_{12,s} \geq 0$. This corresponds to time, $t \geq t^*$.

5.2.4. *Calculation of time delay*

The time delay, t_{delay}, between when phase 1 and phase 2 reach a particular distance, l, can be expressed as:

$$t_{delay}(l) = t(z_{12,s} = l) - t(z_{a1,s} = l) \tag{58}$$

where $t(z_{12,s} = l)$ is calculated using Eq. (56) and $t(z_{a1,s} = l)$ is calculated using Eq. (29) if $l \leq l_1$ or Eq. (57) if $l > l_1$.

5.3. Materials and Methods

5.3.1. Preparation and characterization of ATPSs for flow studies

All reagents and materials were purchased from Sigma-Aldrich (St. Louis, MO) unless noted otherwise. Poly(ethylene glycol-*ran*-propylene glycol) (12 kDa) (EOPO) and sodium citrate salt (2.6:1 trisodium citrate:citric acid to maintain pH 5) were dissolved in diH_2O to create EOPO-citrate ATPSs. Similarly, EOPO and sodium sulfate salt were dissolved in 0.1M tris(hydroxymethyl)aminomethane (Tris) buffer (pH 9) to create EOPO-sulfate ATPSs. For both the EOPO-citrate and EOPO-sulfate ATPSs, three different 3:1 equilibrium volume ratios (volume of the top phase divided by the volume of the bottom phase) were found by varying the initial % w/w compositions of EOPO and respective salt. For individual phase characterization, 10 g ATPSs were made. Each solution was vortexed and allowed to phase separate overnight. After phase separation was completed, the solution was centrifuged for 5 min at 2000 rpm, and the immiscible phases were extracted using a pipette and collected in separate tubes for characterization. The viscosity of each phase was measured in triplicate using a Brookfield LVDV-I Prime digital viscometer (AMETEK Brookfield, MA). The surface tension of each phase was measured using a Krüss K6 force tensiometer (Krüss USA, NC). For the flow studies, 0.5 g ATPSs were made with 5 μL of brilliant blue FCF dye to aid in visualization of the phases.

5.3.2. Demonstration of automated and tunable reagent delivery on paper using ATPS

Flow studies were conducted to measure the speeds of ATPS phases as they separated and flowed through fiberglass paper via capillary action. The fiberglass paper was mounted onto an adhesive backing and cut into 3 mm × 67 mm strips. A three-dimensional (3D) paper wick was placed at the lower end of the strip which aided in the separation of the ATPS as it flowed through the paper. This wick was composed of five stacked sheets of 7 mm x 15 mm fiberglass paper. The paper setup was enclosed in a custom-made acrylic cassette to hold the wick together and minimize effects of evaporation. The top piece of the acrylic cassette was marked every 5 mm along the length of the strip. To run the flow studies, the wick end of the paper setup was dipped into a 24 well plate containing a 0.5 g well-mixed ATPS with blue dye (**Figure 5-2**). The wicking process was recorded using a Nikon D3400 digital camera (Nikon, Tokyo, Japan). Experiments were performed in triplicate and analyzed using QuickTime Player (Apple, Cupertino, CA) to track the locations of each phase as they flowed through the paper setup.

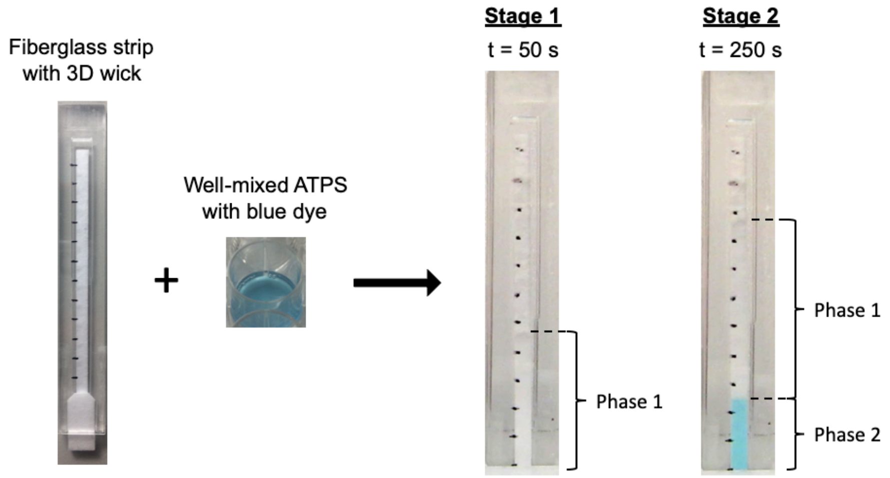

Figure 5-2 Experimental setup for ATPS flow studies.

5.3.3. *Preparation of anti-C. trachomatis antibody- and alkaline phosphatase-decorated gold nanoparticle probes*

To create anti-*C. trachomatis* antibody- and alkaline phosphatase (ALP)-decorated gold nanoprobes (*C. trachomatis* ALP-GNPs), 35 μL of a 0.1 M sodium borate solution (pH 9) was first added to 1 mL of 40 nm citrate-capped gold nanoparticles (nanoComposix, San Diego, CA). Then, 20 μg of alkaline phosphatase was added to the gold suspension and allowed to incubate for

5 min at room temperature. Subsequently, 8 μg of anti-*C. trachomatis* antibodies were added and incubated for 25 min at room temperature. 100 μL of a 10% (w/v) bovine serum albumin (BSA) solution was then added to the suspension and incubated for 10 min. Free antibodies and ALP were removed by centrifugation and the pellet was resuspended in 100 μL of a 0.1 M sodium borate (pH 9) solution.

5.3.4. Detection of C. trachomatis using the conventional LFA

The conventional LFA strips were composed of overlapping pads secured to an adhesive backing. These pads included a sample pad, a conjugate pad, a nitrocellulose membrane, and an absorbent pad. The sample pad consisted of a 3 x 10 mm fiberglass paper treated with a 1% BSA in 0.1 M Tris (pH 9) solution. Anti-*C. trachomatis* ALP-GNPs were dehydrated onto a 3 x 10 mm fiberglass paper along with a 1% BSA in H_2O solution to form the conjugate pad. Both the sample and conjugate pads were dehydrated under very low pressure using a Labconco FreezeZone 4.5 lyophilizer (Fisher Scientific, Hampton, NH) for 2 h. LFA strips in these experiments utilized the sandwich assay format, and antibodies specific to *C. trachomatis* were immobilized on backed nitrocellulose membrane by striping a solution of the antibodies containing 25% (w/v) sucrose. This constituted the test line of the test strip. Protein A was similarly immobilized to constitute the control line of the test. The membrane was left in a vacuum-sealed desiccation chamber overnight. The nitrocellulose membrane was cut into strips 3 mm in width. The LFA test strip was placed in a custom-made acrylic cassette to protect it from environmental factors.

To determine the LFA detection limit for *C. trachomatis*, the test strip was inserted vertically into 50 μL of a sample suspension containing *C. trachomatis* where the suspension wicked through the strip *via* capillary action towards the absorbent pad. In this format, the presence of the target bacteria *C. trachomatis* in sufficient quantities will produce a red test line, as the gold nanoprobes will first bind to the biomarker, which will then be captured by the immobilized antibodies at the test line. An absence or insufficient quantity of *C. trachomatis* will result in no visible test line. Regardless of the presence or absence of *C. trachomatis*, the control line will appear, indicating that fluid has flowed up the entire strip and that the test is therefore valid. Time-lapse videos of the test strips were taken using a digital camera (Canon, Tokyo, Japan). Additionally, images of the test strips were taken after 30 min in a controlled lighting environment.

5.3.5. Detection of C. trachomatis using the ACE-LFA with enzyme signal enhancement

For the ACE-LFA, the test strip design was modified to include a 3D paper wick instead of the sample pad. This wick was composed of four stacked sheets of 7 mm x 15 mm fiberglass paper connected to the nitrocellulose membrane. The ACE-LFA test strip was also enclosed in a custom-made acrylic cassette to hold the wick together and protect the strip from evaporation. Additionally, the top of the cassette applies light pressure to the conjugate pad, ensuring complete and even release of the dehydrate nanoprobes (**Figure 5-3**).

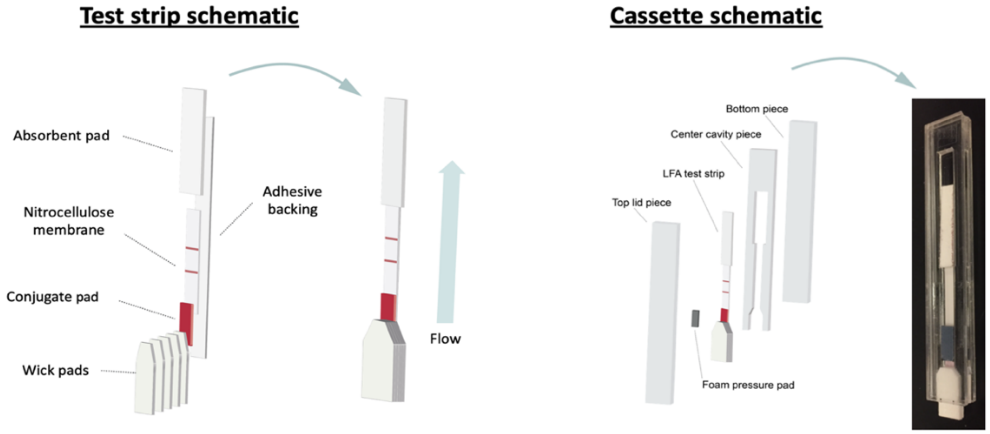

Figure 5-3 Schematics of the ACE-LFA paper test strip setup and the acrylic cassette

For detection of *C. trachomatis* using the ACE-LFA, 500 μL of a well-mixed 3:1 volume ratio ATPS containing 6.6 μL of a 50 mg/mL nitroblue tetrazolium (NBT) solution, 3.3 μL of a 50 mg/mL 5-bromo-4-chloro-3-indolyl-phosphate (BCIP) (Promega Corporation, Madison, WI) solution, and a known concentration of *C. trachomatis* were added into a 24 well plate. The 3D wick-modified LFA strip was then placed into the mixed ATPS, and the solution was allowed to pass through the 3D wick towards the absorbent pad. Videos of the test strips were taken to monitor the signal development over time. Additionally, images of the resulting test strips were taken after 30 min in a controlled lighting environment. To quantify the test line intensities, images of the LFA test strips, as well as the video frames (1 frame per 30 sec), were processed using a custom MATLAB script developed by our lab.[57]

5.3.6. Preparation of E. coli *bacteria cell cultures*

Escherichia coli O157:H7 (*E. coli)* (ATCC® 700728™) were cultured according to manufacturer protocol (ATCC, Manassas, VA) and plated onto Difco Nutrient Agar (Becton, Dickson and Company, Sparks, MD) plates. The plated cells were incubated at 37ºC aerobically overnight and then the plate was sealed with Parafilm and stored at 4ºC until use. To prepare liquid bacterial cultures, single colonies were picked from the agar plate and cultured in 5 mL of Difco Nutrient Broth (Becton, Dickson and Company, Sparks, MD). The cells were incubated at 37ºC and 250 rpm on a shaking incubator for 16 h. To quantify the bacteria concentrations within the original liquid suspension, serial dilutions of bacteria were plated and colonies were counted after overnight incubation.

5.3.7. Measuring the partitioning of E. coli and TMB in ATPS

To measure the partitioning of both *E. coli* and 3,3’,5,5’-tetramethylbenzidine (TMB) in the EOPO-salt ATPS, either ~10^7 cells or 10 μL of an 816 mM TMB solution in dimethylformamide (DMF) were added to an ATPS with a total final mass of 0.5 g. The ATPSs were vortexed and allowed to phase separate at room temperature (22°C) for 2 h. Each phase of the ATPS was carefully withdrawn using a micropipette and diluted in water. For the *E. coli* partitioning studies, the EOPO-rich top phase and EOPO-poor bottom phases were diluted by 2-fold. A hemocytometer (Thermo Fisher Scientific, Waltham, MA) was used to count the total number of cell entities in each phase. The partition coefficient for *E. coli*, which is defined as the concentration of *E. coli* in the top phase divided by the concentration in the bottom, was then calculated. The hemocytometer was used in these experiments instead of counting colonies to avoid possible error caused by the ATPS components inhibiting bacteria growth. For the TMB partitioning studies, the EOPO-rich top phase was diluted by 100-fold, while the EOPO-poor bottom phase was diluted by 10-fold to reduce interference cause by the phase forming components during analysis. The absorbance at the peak wavelength for reduced TMB ($\lambda_{max} = 286$ nm) was then measured for each diluted phase using a GENESYS 10S UV-Vis spectrophotometer (Thermo Fisher Scientific, Waltham, MA). The partition coefficient for TMB was calculated by multiplying the measured absorbances by the dilution factor and then taking the ratio of the resulting values for the top and bottom phases. Each partitioning experiment was performed in triplicate.

5.3.8. *Preparation of anti-E. coli antibody-decorated nanoparticle probes*

First, platinum-coated gold nanozymes (PtGNs) were synthesized using a protocol derived from Gao *et. al.*[65] Briefly, 4 mL of 40 nm citrate-capped gold nanoparticles (GNs) (Nanocomposix, San Diego, CA) and 1827 µL of filtered ultrapure water were preheated to 90°C in an oil bath under magnetic stirring for 20 min. Following the preheating, 173 µL of a 0.82 mM chloroplatinic acid hydrate solution and 2 mL of a 3.3 mM ascorbic acid solution were injected separately into the gold nanoparticle suspension using a syringe pump at rates of 0.6 and 1.2 mL/h, respectively. The reaction was allowed to proceed for 30 min after the injection was complete.

To create anti-*E. coli* platinum-coated gold nanozyme probes (anti-*E. coli* PtGNPs), 20 µL of a 0.1 M sodium borate solution (pH 9) was first added to 1 mL of PtGNs. Then, 4 µg of primary Bactrace anti-*E. coli* O157:H7 antibody (Seracare, Milford MA) was added to the suspension and incubated for 30 min at room temperature (22°C). 50 µL of a 10% (w/v) bovine serum albumin (BSA) solution was then added to the suspension and incubated for 10 min. Free antibodies were removed by centrifugation and the pellet was resuspended in 50 µL of a 0.1 M sodium borate (pH 9) solution. Anti-*E. coli* gold nanoprobes (Anti-*E. coli* GNPs) were made using the same procedure; however, 40 nm GNs were used in place of PtGNs at the same concentration.

5.3.9. *Detection of E. coli using the conventional LFA*

The conventional LFA strips for the detection of *E. coli* were assembled similar to those used for the detection of CT, with a few key modifications. For these strips, the sample pad consisted of a 3 mm × 10 mm Standard 17 fiberglass paper (GE Healthcare Bio-Sciences) treated with a running buffer (0.4% BSA, 0.6% Tween 20, and 0.2% polyethylene glycol 8kDa in phosphate-buffered saline, pH 7.4). Anti-*E. coli* GNPs were dehydrated onto a 3 mm x 10 mm fiberglass paper along with a 1% BSA in diH_2O solution to form the conjugate pad. Both the sample and conjugate pads were dehydrated under very low pressure using a Labconco FreezeZone 4.5 lyophilizer (Thermo Fisher Scientific, Waltham, MA) for 2 h. LFA strips in this study utilized the sandwich assay format where Bactrace anti-*E. coli* antibody were immobilized on a Unistart CN95 nitrocellulose membrane (Sartorius, Göttingen, Germany) at 0.5 mg/mL. This constituted the test line of the test strip. Anti-goat antibodies (Bethyl, Montgomery, TX) were immobilized at 0.25 mg/mL to constitute the control line of the test strip. Test and control line printing was performed by dispensing 50 μL of antibody solution per 30 cm of nitrocellulose membrane using an Automated Lateral Flow Reagent Dispenser (Claremont BioSolutions, Upland, CA) and a Fusion 200 syringe pump (Chemyx, Stafford, TX) with a flow rate of 300 μL/min. The membrane was left in a vacuum-sealed desiccation chamber overnight. The nitrocellulose membrane was placed on the adhesive backing and cut into strips 3 mm in width prior to assembly with the sample pad, conjugate pad, and absorbent pad. The LFA test strip was placed in a custom-made acrylic cassette to limit evaporation while running the assay. The top of the cassette also applied light pressure to the conjugate pad, aiding in the uniform flow through the conjugate pad and uniform release of the dehydrated anti-*E. coli* GNPs.

To detect for *E. coli* in buffer using the conventional LFA, the test strip was inserted vertically into 125 μL of a sample suspension containing a known concentration of *E. coli* in phosphate-buffered saline (PBS). To detect for *E.* coli in Surine^{TM} Negative Urine Control (Cerilliant, Round Rock, TX), the test strip was inserted into 165 μL of *E. coli* in Surine. Videos of the test strips were taken using a Nikon D3400 digital camera (Nikon, Tokyo, Japan). Additionally, photos were taken after 30 min in a controlled lighting environment. To quantify the test line intensities, images of the LFA test strips, as well as the video frames (1 frame per 3 min), were processed using a custom MATLAB script developed by our lab.[57]

5.3.10. Detection of E. coli using the ACE-LFA with nanozyme signal enhancement

The ACE-LFA setup was composed of a test strip as well as an ATPS solution with signal enhancement reagents. For the test strip, the conventional LFA strip design was modified to include a 3D paper wick instead of the sample pad. Our lab has previously found the 3D wick to aid in ATPS separation on paper, because more volume can enter the paper at the same time, and there is more room for the domains of each phase to migrate, find like-phase domains, and coalesce. This wick was composed of five stacked sheets of 7 mm × 15 mm fiberglass paper with the top corners cut at a 45° angle (**Figure 5-2**). PtGNPs were dehydrated onto the conjugate pad in place of the GNPs. The ACE-LFA test strip was enclosed in a custom-made acrylic cassette to hold the wick together and to limit evaporation while running the assay. This cassette also includes a foam pressure pad to apply light pressure to the conjugate pad, which aids in uniform conjugate release.

To detect *E. coli* in PBS using the ACE-LFA, a 0.5 g well-mixed 12.9% EOPO – 10% salt 3:1 volume ratio ATPS containing 10 μL of an 816 mM TMB solution in DMF, 10 μL of a 30% w/v hydrogen peroxide solution, 50 μL of a TMB stabilizing solution (Vector Laboratories, Burlingame, CA), and 5 μL *of E. coli* in PBS were added into a well of a 24 well plate. The 3D wick-modified test strip was then placed into the mixed ATPS, and the solution was allowed to pass through the wick towards the absorbent pad. To detect *E. coli* with the LFA + ATPS, the above ACE-LFA procedure was modified by replacing the TMB with 10 μL of DMF. To detect *E. coli* in Surine™ using the ACE-LFA, a 0.5 g well-mixed 12.9% EOPO – 8.2% salt ATPS containing 15 μL of an 816 mM TMB solution in DMF, 10 μL of a 30% w/v hydrogen peroxide solution, 100 µL of a TMB stabilizing solution, and 165 µL of *E. coli* in Surine™ were added into a well of a 24 well plate followed by the addition of the test strip. Videos of the test strips were taken to monitor the signal development over time. Images of the resulting test strips were also taken after 30 min in a controlled lighting environment. To quantify the test line intensities, the video frames (1 frame per 3 min) and images were processed using a custom MATLAB script developed by our lab.

5.4. Results and Discussions

5.4.1. Demonstration of tunable flow behavior and reagent delivery on paper using ATPSs

In this work, we hypothesized that the separation and flow of an ATPS through a paper membrane can be used to automate both biomarker preconcentration and the delivery of signal enhancement reagents on a paper-based device. Many varieties of ATPS exist; however, here we will be discussing the use of a polymer-salt system composed of EOPO and sodium citrate, as well as one composed of EOPO and sodium sulfate. When salt is added to an aqueous solution of EOPO, the salt will disrupt the hydrogen bonds between the water and the oxygen atoms of the EOPO polymer chains. This will decrease the EOPO-water interactions and increase the EOPO-EOPO interactions, ultimately leading to phase separation where immiscible microscopic EOPO-rich and salt-rich (EOPO-poor) domains are formed to minimize the Gibbs free energy of the system.

To utilize this ATPS to sequentially deliver reagents as they flow through a paper device, the reagents to be delivered are first added to the mixed ATPS where they must partition or localize extremely into microdomains of the opposite phases. Subsequently, the ATPS is applied to a paper device where it will rapidly separate into its two bulk, macroscopic phases as it flows via capillary action. The reagents localized in the leading EOPO-poor phase of the ATPS will be delivered first to the region of interest on the paper device. This is then followed by the lagging EOPO-rich phase, which will deliver the reagents localized in that phase in an automated fashion. Note that, in this work, the "extreme" localization of reactive reagents into opposite macroscopic phases, means that the reagents are separated from one another to a great enough degree to prevent premature interactions that could result in undesired visible signal development.

When designing a system to automate reagent delivery, it is important to have tunable fluidic control. We hypothesized that we could achieve this fluidic control by changing the equilibrium state of the ATPS. By altering the initial concentrations of the phase forming components added to the ATPS, the properties such as the equilibrium volume ratio and concentrations of phase forming components in the equilibrium phases, can be changed, which will affect the physical properties that dictate flow behavior. For a polymer-salt ATPS system (such as the EOPO-salt systems used in this study) with a fixed volume ratio, an increase in the initial concentration of polymer results in an increase in the concentration of polymer in the polymer-rich phase and a decrease in the concentration of polymer in the polymer-poor phase at equilibrium.[138] We anticipated that this increase in the equilibrium concentration of polymer in the polymer-rich phase would result in an increase in the viscosity of that phase, which in turn, would result in slower flow and a greater reagent delivery time. To confirm this, we experimentally found conditions for three different EOPO-citrate ATPS and four different EOPO-sulfate ATPS compositions that all yielded a 3:1 volume ratio. The measured viscosities of the EOPO-rich and EOPO-poor phases for these systems are shown in **Figure 5-4** and **Figure 5-5**.

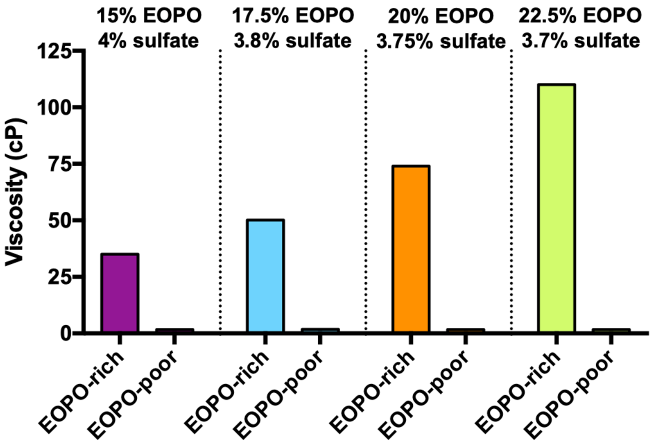

Figure 5-4 Viscosity measurements for the extracted phases from the EOPO-sulfate ATPS.

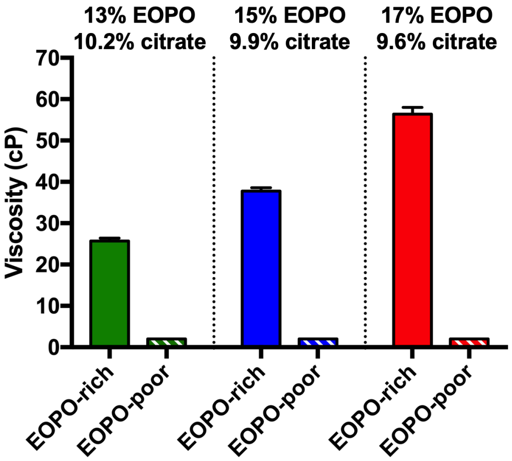

Figure 5-5 Viscosity measurements for the extracted phases from the EOPO-citrate ATPS.

Consistent with our expectations, an increase in the initial concentration of EOPO added to the EOPO-sulfate ATPSs (at a fixed 3:1 volume ratio) resulted in the viscosity of the EOPO-rich phase also increasing from 35 cP for the 15% EOPO – 4% sulfate salt ATPS to 50 cP for the 17.5% EOPO – 3.8% sulfate salt ATPS to 74 cP for the 20% EOPO – 3.7% sulfate salt ATPS to 110 cP for the 22.5% EOPO – 3.75% sulfate salt ATPS, while the viscosities of the EOPO-poor phases were found to be constant at 1.7 cP for all systems tested. Similarly, an increase in the initial concentration of EOPO added to the EOPO-citrate ATPSs (at a fixed 3:1 volume ratio) resulted in the viscosity of the EOPO-rich phase also increasing from 25.7 ± 0.7 cP for the 13% EOPO – 10.2% citrate salt ATPS to 37.8 ± 0.8cP for the 15% EOPO – 9.9% citrate salt ATPS to 56.4 ± 1.6 cP for the 17% EOPO – 9.6% citrate salt ATPS, while the viscosities of the EOPO-poor phases were found to be constant at 2.0 cP for the systems tested.

For each different ATPS, the locations of the air - EOPO-poor phase (air - phase 1) interface and the EOPO-poor phase - EOPO-rich phase (phase 1 - phase 2) interface were tracked as they flowed through the paper setup and plotted versus time (**Figure 5-6** and **Figure 5-7**). It is observed that an increase in the initial concentration of EOPO in the ATPS resulted in a slower moving phase 1 - phase 2 interface. This was expected because increasing the initial EOPO concentration made the EOPO-rich phase more viscous, and higher viscosity leads to slower flow.

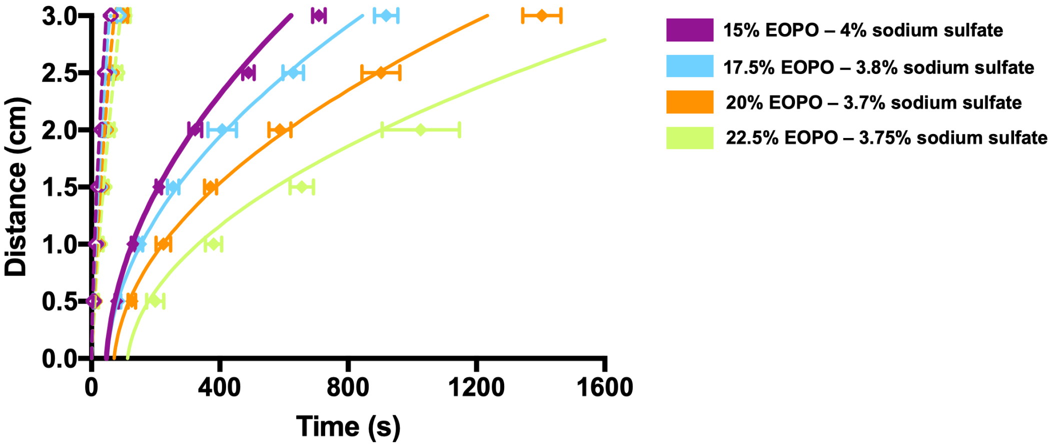

Figure 5-6 Flow study of EOPO-sulfate ATPS

Experimentally measured distance traveled up the paper strip by the air - phase 1 interface (◇, open symbols) and the phase 1 - phase 2 interface (◆, closed symbols) as a function of time. Theoretical model predictions of distance traveled up the paper strip by the air - phase 1 interface (dashed lines) and the phase 1 - phase 2 interface (solid lines) as a function of time.

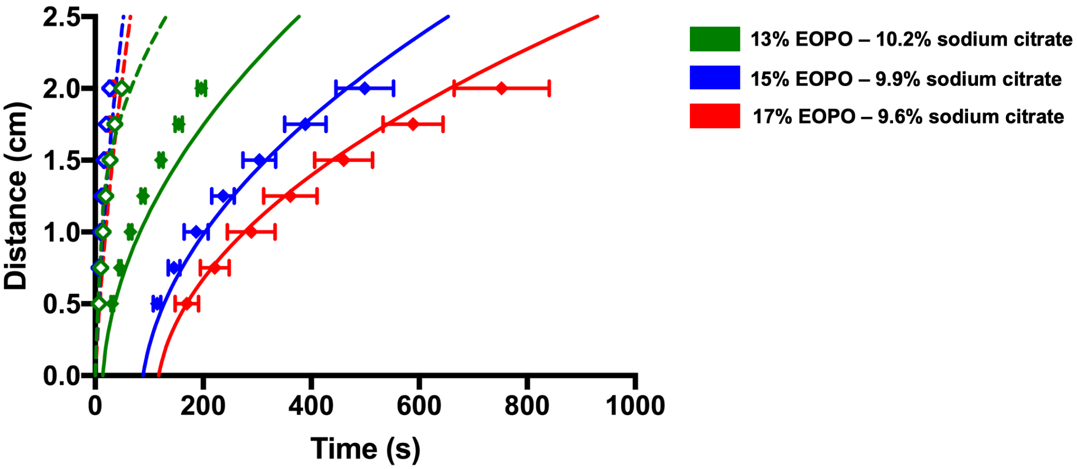

Figure 5-7 Flow study of EOPO-citrate ATPS
Experimentally measured distance traveled up the paper strip by the air - phase 1 interface (◇, open symbols) and the phase 1 - phase 2 interface (◆, closed symbols) as a function of time. Theoretical model predictions of distance traveled up the paper strip by the air - phase 1 interface (dashed lines) and the phase 1 - phase 2 interface (solid lines) as a function of time.

We next calculated the time delay between when the air - phase 1 interface and the phase 1 - phase 2 interface reached the same distance along the paper strip. The time delay is an important metric to be able to control when designing automated reactions and assays, because different applications may require shorter or longer durations of time between the delivery of the reagents. It was observed that the time delay increased with an increase in both the viscosity of the EOPO-rich phase and the distance along the strip. These trends were expected as it is well-established that the viscous resistance, which acts to slow fluid flow, increases with an increase in viscosity and/or an increase in length of the fluid segment.[139] Time delays ranging from 30 to 840 s with the EOPO- citrate ATPS and 71 s to 1320 s with the EOPO-sulfate ATPS were achieved in our experiments (**Figure 5-8** and **Figure 5-9**). Note that greater delays may be obtained by choosing different ATPS systems with phases that have higher viscosities, such as a polymer-polymer or micellar ATPS.

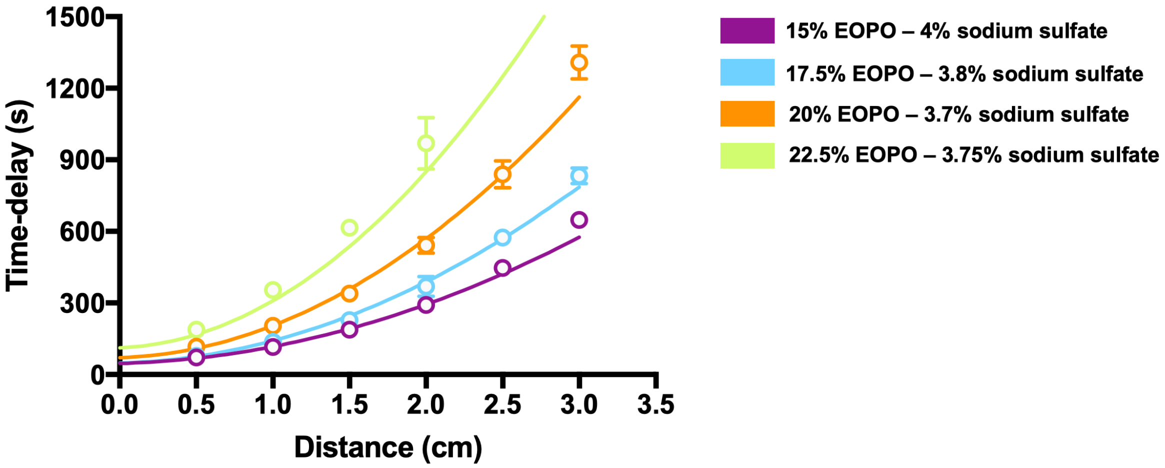

Figure 5-8 Time-delay for EOPO-sulfate ATPS
Time-delay between when the air - phase 1 interface reaches a particular distance along the strip and when the phase 1 - phase 2 interface reaches that same distance. Experimental measurements shown as open symbols (○) and theoretical predictions shown as solid lines

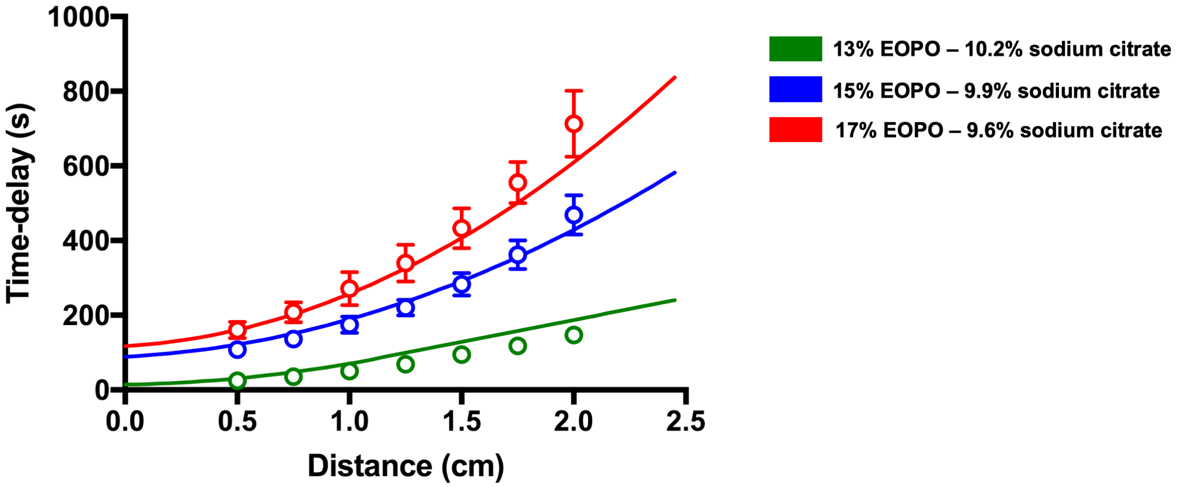

Figure 5-9 Time-delay for EOPO-citrate ATPS
Time-delay between when the air - phase 1 interface reaches a particular distance along the strip and when the phase 1 - phase 2 interface reaches that same distance. Experimental measurements shown as symbols and theoretical predictions shown as solid lines

5.4.2. Theoretical predictions of ATPS flow behavior on paper

In addition to demonstrating tunable flow, we developed a mathematical model to predict the flow behaviors of the ATPSs flowing through paper. Experimentally measured values for surface tension, viscosity, leading phase length, and cross-sectional areas normal to the direction of flow are shown in **Table 5-1** and **Table 5-2**.

Table 5-1 Experimentally measured parameter values for EOPO – sodium sulfate ATPSs flow studies

ATPS Composition	15% EOPO – 4% sulfate	17.5% EOPO – 3.8% sulfate	20% EOPO – 3.7% sulfate	22.5% EOPO – 3.75% sulfate
μ_1 (cP)	1.7	1.7	1.7	1.7
μ_2 (cP)	35	50	74	110
γ_{a1} (mN/m)	57.0 ± 0.6	57.0 ± 0.6	57.0 ± 0.6	57.0 ± 0.6
l_1 (cm)	3	2.7	3	3.5
$l_{w,tot}$ (cm)	1.2	1.2	1.2	1.2
A_w (cm^2)	0.13	0.13	0.13	0.13
A_s (cm^2)	0.011	0.011	0.011	0.011
c	0.085	0.085	0.085	0.085

Table 5-2 Experimentally measured parameter values for EOPO – sodium citrate ATPSs flow studies

ATPS Composition	13% EOPO – 10.2% citrate	15% EOPO – 9.9% citrate	17% EOPO – 9.6% citrate
μ_1 (cP)	2.0 ± 0.0	2.0 ± 0.0	2.0 ± 0.0
μ_2 (cP)	25.7 ± 0.7	37.8 ± 0.8	56.4 ± 1.6
γ_{a1} (mN/m)	57.0 ± 0.6	57.0 ± 0.6	57.0 ± 0.6
l_1 (cm)	1.1	3.5	3.7
$l_{w,tot}$ (cm)	1.2	1.2	1.2
A_w (cm^2)	0.13	0.13	0.13
A_s (cm^2)	0.011	0.011	0.011
c	0.085	0.085	0.085

For the EOPO-sulfate ATPSs, our theoretical model was fit to the 17.5% EOPO – 3.8% sulfate ATPS flow data using a weighted least-squares linear regression in order to back out the effective radii for the strip and the 3D wick (**Table 5-3**). These values of the radii were then used to predict the flow behavior of the 15% EOPO – 4% sulfate, 20% EOPO – 3.7% sulfate, and 22.5% EOPO – 3.75% sulfate ATPSs. For the EOPO-citrate ATPSs, our theoretical model was fit to the 15% EOPO – 9.9% citrate ATPS flow data using a weighted least-squares linear regression in order to back out the effective radii for the strip and the 3D wick (**Table 5-4**). These values of the radii were then used to predict the flow behavior of the 13% EOPO – 10.2% citrate and 17% EOPO – 9.6% citrate ATPSs.

Table 5-3 Parameter values obtained from fitting our model to flow data for the 17.5% EOPO – 3.8% sodium sulfate salt ATPS

	Fit parameter values
R_w (μm)	89.3
R_s (μm)	21.9
n_w (#)	520.4
n_s (#)	730.0

Table 5-4 Parameter values obtained from fitting our model to flow data for the 15% EOPO – 9.9% sodium citrate salt ATPS

	Fit parameter values
R_w (μm)	86.3
R_s (μm)	17.0
n_w (#)	553
n_s (#)	1223

Overall, the predictions using our model were in reasonable quantitative agreement with the experimental results (**Figure 5-6**, **Figure 5-7**, **Figure 5-8** and **Figure 5-9**). The slight deviations that are observed may be explained by differences in the liquid-solid interactions which lead to different phase equilibrium states for the ATPS in paper compared to the ATPS in the tube. Different concentrations of components in the resulting two phases could, in turn, yield differences in the viscosities of the equilibrium phases in paper compared to those experimentally measured in the tube, and thus differences in the predicted versus observed flow behaviors. While future work will aim to understand and address these deviations, the current model can still be used as a design tool to aid in the development of new devices.

5.4.3. Demonstration of improved C. trachomatis detection using ACE-LFA with enzyme signal enhancement

After demonstrating the tunable nature of ATPS flow on paper, we next sought to apply this technology to automate an alkaline phosphatase-based enzyme signal enhancement reaction, and to concentrate and detect *C. trachomatis* on an LFA test. We have called the general technology the **A**TPS-automated **C**oncentration and **E**nhancement of the **L**ateral-**F**low immuno**A**ssay (ACE-LFA). For the ACE-LFA, the LFA test strip was modified to include a 3D paper wick and was then enclosed in an acrylic cassette to protect it from environmental factors and improve device consistency (**Figure 5-3**). To run the ACE-LFA, this test strip is dipped into an ATPS containing *C. trachomatis* and the colorimetric substrates nitro blue tetrazolium/5-bromo-4-chloro-3-indolyl phosphate (NBT/BCIP). Due to its large size and hydrophilicity, the *C. trachomatis* bacteria partitions extremely into the salt-rich phase of the EOPO-sulfate salt ATPS, where it experiences fewer repulsive, steric, excluded-volume interactions with the less abundant

EOPO molecules in that phase. The NBT/BCIP substrates, on the other hand, partition preferentially into the EOPO-rich phase due to their small size and relative hydrophobicity. As this ATPS flows through the 3D wick, it separates into its two macroscopic phases. First, the leading, salt-rich phase containing the concentrated *C. trachomatis* bacteria solubilizes the dehydrated anti-*C. trachomatis* ALP-GNPs and delivers them to the LFA test zone where they can bind to the test and control lines (**Figure 5-10**). This is followed by the lagging, polymer-rich phase which delivers the NBT/BCIP substrates to the LFA detection zone. Once the NBT/BCIP comes into contact with the anti-*C. trachomatis* ALP-GNPs bound to the test and control lines, it will be converted into a dark purple precipitate, thereby enhancing the signal. It's important to note that because the NBT/BCIP substrates partition favorably into the EOPO-rich phase, while the anti- *C. trachomatis* ALP-GNPs are rehydrated by the salt-rich phase, premature signal enhancement is avoided.

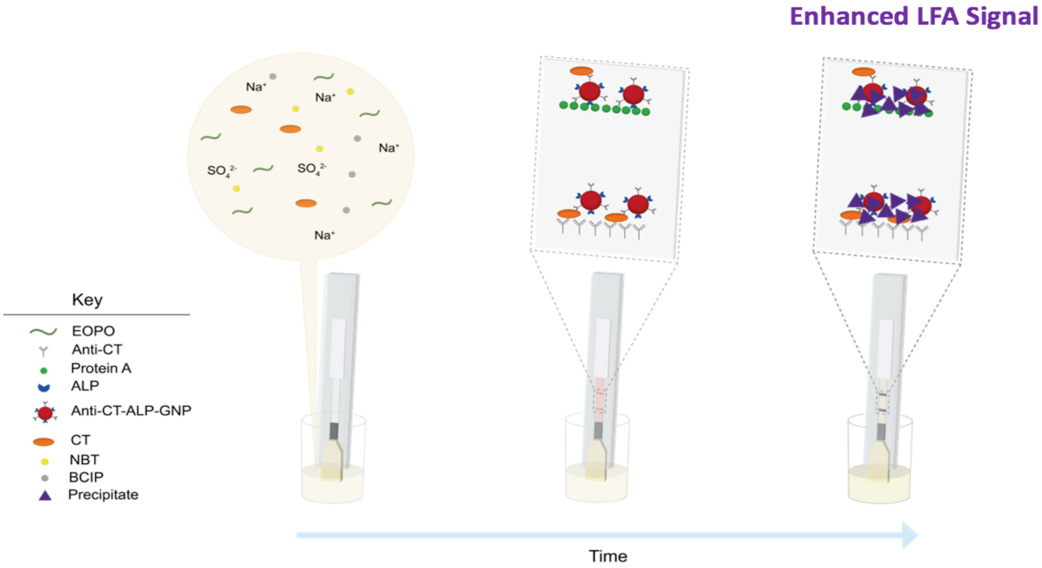

Figure 5-10 Schematic of ACE-LFA for the detection of CT.
The test strip is dipped into an ATPS solution and will phase separate. The leading phase delivers the concentrated CT and rehydrated ALP-GNPs to the detection zone. This is followed by the lagging phase, which delivers the NBT/BCIP substrate to enhance LFA signal.

To demonstrate the ability of the ACE-LFA to automate the signal enhancement reaction and therefore improve signal over the conventional LFA, we tested a sample containing 10 ng/µL of inactivated *C. trachomatis* in both assays. A video of the signal development was taken over the course of 30 minutes. For the conventional LFA, a pink signal developed slowly over the course of 30 min (**Figure 5-11**). For the ACE-LFA on the other hand, a pink test line was visible within the first 5 min of the assay, due to the concentration achieved with the ATPS, and after 15 and 30 min, it was converted into a dark purple line, indicating a successful, automated signal enhancement reaction. We also quantified the test line intensities using a MATLAB script developed in our lab.

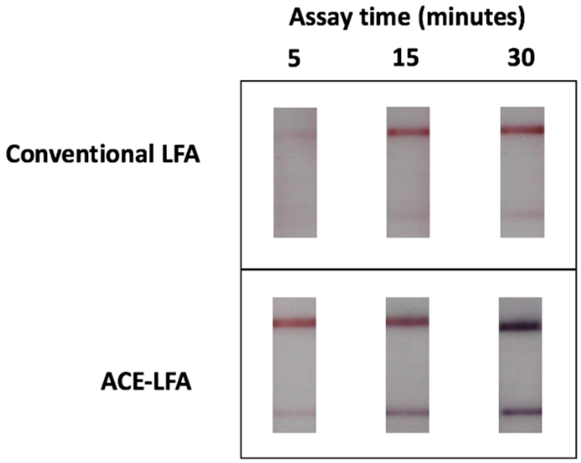

Figure 5-11 Time series development of the conventional LFA and ACE-LFA tested at 10 ng/µL of CT.

The ACE-LFA has a faster signal generation than the conventional LFA at all time points. Additionally, after 30 min of assay time, the test line intensity of the ACE-LFA was measured to be 7 times greater than that of the conventional LFA. After demonstrating the ability of the ATPS to automate a signal enhancement reaction on the LFA, we wanted to determine if this assay had an improved detection limit over the conventional LFA. First we identified the detection limit of the conventional LFA by testing dilutions of inactivated *C. trachomatis* in phosphate-buffered saline (PBS). The conventional LFA was able to successful detect CT at 10 ng/µL at 30 min, indicated by the formation of 2 visible lines. The ACE-LFA was able to detect *C. trachomatis* at 0.32 ng/µL after 30 min, demonstrating a 30-fold improvement in detection limit over the conventional LFA (**Figure 5-12**). This 30-fold improvement in detection limit is a result of the compounding improvements from both biomarker preconcentration and signal enhancement. The conventional LFA detected CT at 10 ng/µL, while the enhanced LFA detected CT at 0.32 ng/µL. This corresponds to a 30-fold improvement in detection limit over the conventional LFA when using the ACE-LFA.

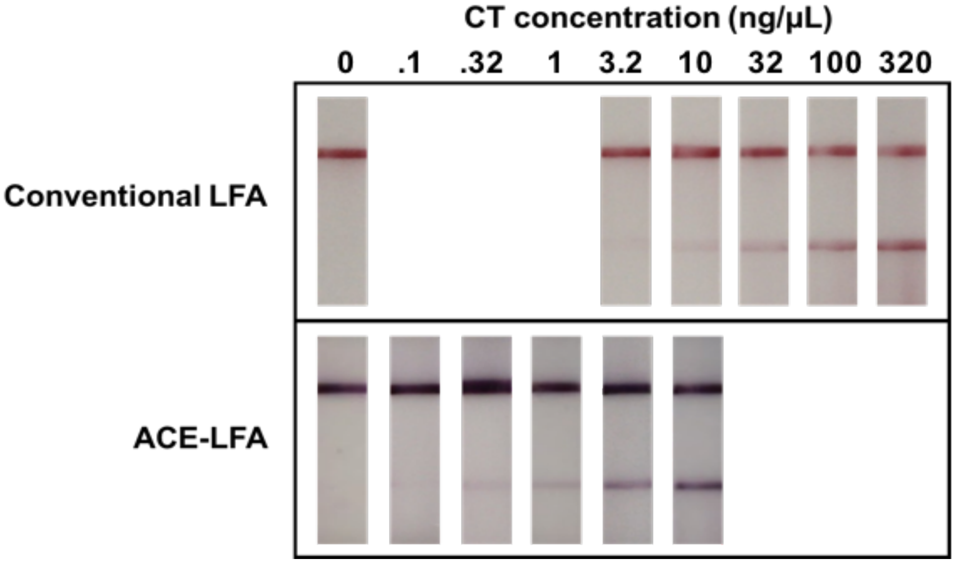

Figure 5-12 Detection limit comparison of conventional LFA and ACE-LFA
The conventional LFA detected CT at 10 ng/µL, while the enhanced LFA detected CT at 0.32 ng/µL. This corresponds to a 30-fold improvement in detection limit over the conventional LFA when using the ACE-LFA.

5.4.4. *Demonstration of improved E. coli detection using ACE-LFA with nanozyme signal enhancement*

Here, we look to further develop our ACE-LFA technology by utilizing a different signal enhancement method as well as demonstrating its application for the detection of a different model bacteria *E. coli*. One disadvantage of our previous demonstration of the ACE-LFA is that we used an enzymatic signal enhancement reaction. Enzymes are often expensive to produce and have poor shelf lives, making them difficult to implement effectively in point-of-care diagnostic devices. As an alternative to enzymes, here we are utilizing nanozymes, which are inorganic nanoparticles that have been shown to possess intrinsic catalytic activities similar to natural enzymes. These nanozymes have been demonstrated to serve as an excellent replacement of traditional signal enhancement enzymes as they are low in cost, possess superior stability and catalytic activity over a wide range of temperatures and pHs, easy to conjugate with proteins, and often possess an inherent visible color, which makes them well suited for use on the LFA.[140] We have utilized a recently developed nanozyme system containing platinum-coated gold nanozymes which catalyze the oxidation of TMB in the presence of hydrogen peroxide to produce a dark purple precipitate.[65] To run the ACE-LFA, a test strip with a 3D wick was dipped into an ATPS containing *E. coli* and the signal enhancement reagents: TMB, hydrogen peroxide, and TMB stabilizing solution. We initially chose the 13% EOPO – 10.2% citrate salt ATPS for use in the ACE-LFA, because it was found to allow ~6 min for antibody binding before the lagging phase crossed the test line. This is comparable to many commercial assays and should allow reasonable time for antibody-antigen binding to occur at the test line as well as signal enhancement reagents to be delivered. When the signal enhancement reagents were added to the 13% EOPO – 10.2% citrate salt ATPS, the observed volume ratio shifted from 3:1 to ~2:1. While this volume ratio shift is not completely understood, the proprietary TMB stabilizing solution, which is required to produce an insoluble rather than a soluble TMB product, was found to be responsible and thus must contain some compound that influences phase separation (i.e., salt, polymer, or organic solvent). Therefore, for the ACE-LFA demonstrations in this work, a 12.9% EOPO – 10% citrate salt ATPS with the TMB stabilizer was used instead, which was found to produce a 3:1 volume ratio in a microcentrifuge tube and also had comparable flow behaviors to 13% EOPO – 10% citrate salt ATPS without the stabilizer (data not shown).

Recall that reagents must be localized in opposite phases of the ATPS in order for them to be sequentially delivered. The partitioning of different molecules and particles between the two phases of an ATPS depends on a variety of physical and chemical properties, such as size, hydrophobicity, and electrochemical properties of the target species.[138] Due to its large size and hydrophilicity, the *E. coli* bacteria was expected to partition extremely into the EOPO-poor phase of the EOPO-citrate salt ATPS, where it would experience fewer repulsive, steric, excluded-volume interactions with the less abundant EOPO molecules in that phase. In the case of the 3:1 volume ratio used in this work, the *E. coli* would be forced into one-fourth of the original ATPS volume, thus concentrating it by four-fold. The TMB substrate, which is small and relatively hydrophobic, was expected to partition preferentially into the more hydrophobic EOPO-rich phase. The partition coefficients for both *E. coli* and TMB in our ATPS were measured to be 0.0029 ± 0.0005 and 11.1 ± 0.3, respectively. A partition coefficient value less than one indicates preferential partitioning to the EOPO-poor phase, while a value greater than one indicates preferential partitioning to the EOPO-rich phase. These results were consistent with our hypothesis that the *E. coli* and TMB would selectively localize into opposite ATPS phases.

When the ATPS containing *E. coli* and the signal enhancement reagents is added to the ACE-LFA test strip, it flows through the 3D wick and separates into its two macroscopic phases. First, the leading, EOPO-poor phase containing the concentrated *E. coli* bacteria solubilizes the dehydrated anti-*E. coli* PtGNPs and delivers them to the LFA detection zone. Here, the presence of the target biomarker *E. coli* in sufficient quantities produces a visible pink or red test line, as the PtGNPs first bind to the *E. coli* and then these PtGNP - *E. coli* complexes become captured by the immobilized antibodies at the test line. An absence or insufficient quantity of *E. coli* results in no visible test line. Regardless of the presence or absence of *E. coli*, the control line appears, indicating that the PtGNPs flowed up the entire strip and that the test is therefore valid (**Figure 5-13**). This is followed by the lagging, EOPO-rich phase, which delivers the TMB to the LFA detection zone. In the presence of hydrogen peroxide, TMB that comes into contact with the PtGNPs bound to the test and control lines will be converted into a dark purple precipitate, thereby enhancing the signal. It is important to note that because the TMB partitions favorably into the EOPO-rich phase, while the anti-*E. coli* PtGNPs are rehydrated into the EOPO-poor phase so the reactive reagents are effectively separated from one another. It is this thermodynamic separation of reactive reagents within the ATPS, along with the ability of the ATPS to phase separate as it flows through paper, that allows for the automation of signal enhancement while avoiding premature signal development.

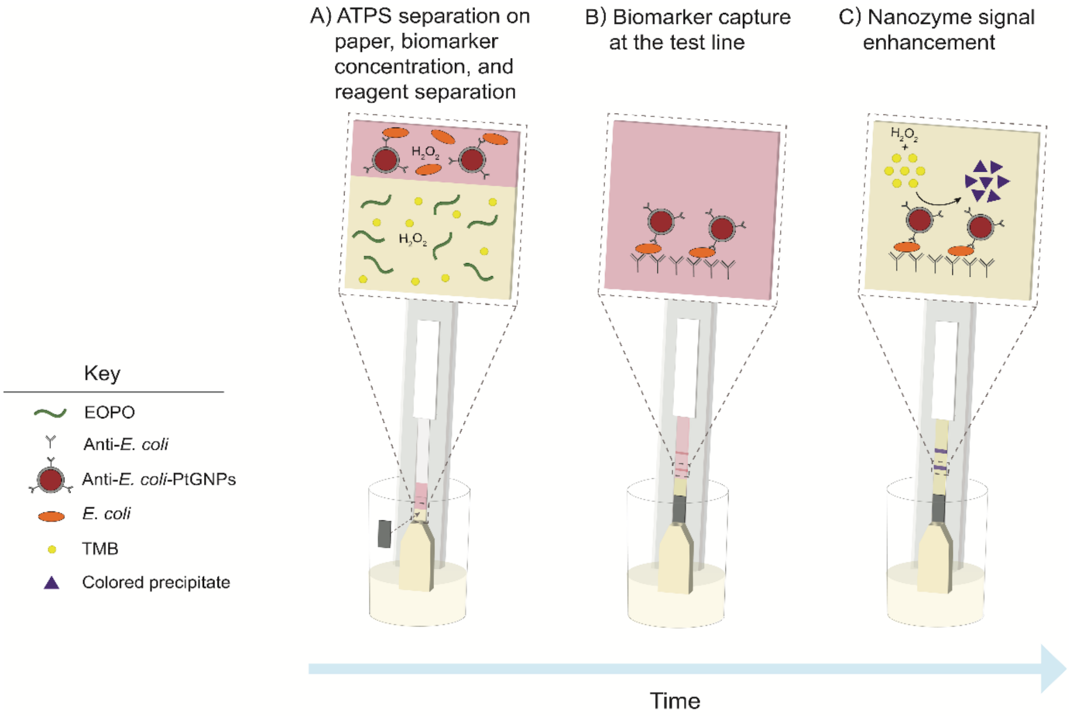

Figure 5-13 Schematic of ACE-LFA for the detection of *E. coli*.
(A) The test strip is dipped into an ATPS solution which phase separates as it flows through the paper. *E. coli* is concentrated in the leading phase, and the TMB partitions preferentially into the lagging phase. The leading phase delivers the concentrated *E. coli* and rehydrated PtGNPs to the detection zone. (B) Biomarker capture occurs at the LFA detection zone where *E. coli* is sandwiched between the test line antibodies and the PtGNPs. (C) This is followed by the lagging phase, which delivers the TMB substrate to initiate the nanozyme signal enhancement reaction.

To demonstrate that the above process does indeed occur *and* to examine the ability of the ACE-LFA to automate the nanozyme signal enhancement reaction and therefore improve signal over the conventional LFA, we tested each assay with an overall *E. coli* concentration of 10^6 colony forming units (cfu)/mL in the sample/ATPS. A video of the signal development was taken over the course of 30 min. For the conventional LFA, a visible pink test line developed within 15 min (**Figure 5-14)**. For the ACE-LFA, a pink test line was visible within the first 6 min of the assay. The earlier formation of the pink test line in the ACE-LFA compared to the conventional LFA was due to the *E. coli* being concentrated in the leading phase of the ATPS which only occurred in the ACE-LFA. For the ACE-LFA, the interface between the leading and lagging phases can be observed in the 6 min photo. After ~7 min, the lagging phase crossed the test line region, delivering the TMB and initiating the nanozyme signal enhancement reaction. Signal enhancement was observed as the test and control line color changed from pink to purple.

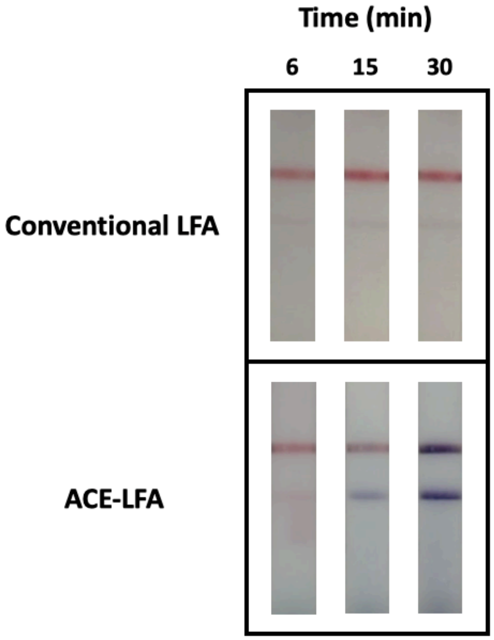

Figure 5-14 Comparing signal development over time for the conventional LFA and the ACE-LFA tested with 10^6 cfu/mL of *E. coli.*

We also quantified the test line intensities using a MATLAB script developed by our lab and the results are plotted in **Figure 5-15**. After 30 min of assay time, the test line intensity of the ACE-LFA was measured to be 14-fold greater than that of the conventional LFA (relative test line signal of ACE-LFA was 100.0 ± 7.9% compared to the conventional LFA at 7.0 ± 0.7%). These results confirmed that our ACE-LFA technology has the ability to successfully automate both biomarker preconcentration and nanozyme signal enhancement while maintaining a low background signal, suggesting that it may serve as a more sensitive alternative to the conventional LFA.

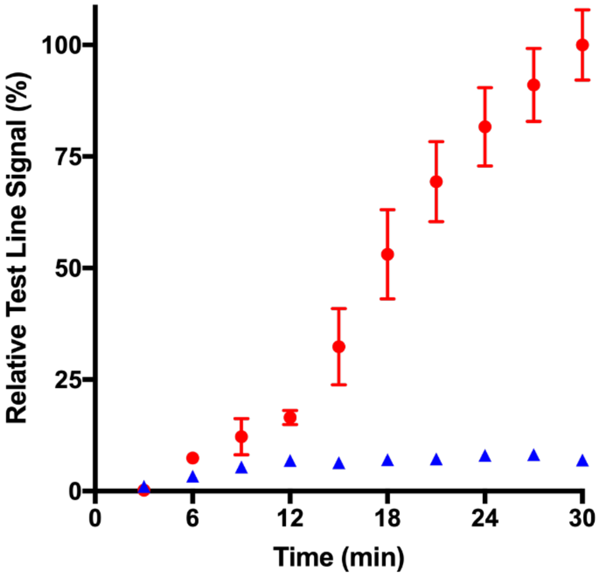

Figure 5-15 Quantification of signal development of the ACE-LFA and conventional LFA for *E. coli* at 10^6 cfu/mL.
Plot of quantified relative test line signal vs. time for both the conventional LFA (blue ▲) and ACE-LFA (red ●). All of the data are presented as mean ± SD (n = 3)

We next wanted to determine if the ACE-LFA had an improved detection limit relative to the conventional LFA. First, we identified the detection limit of the conventional LFA with GNPs by testing dilutions of *E. coli* in PBS. The conventional LFA was able to successfully detect *E. coli* down to a concentration of 10^6 cfu/mL within 30 min, indicated by the formation of 2 visible lines. On the other hand, the ACE-LFA was able to detect *E. coli* at 3.3×10^4 cfu/mL, demonstrating a 30-fold improvement in detection limit over the conventional LFA (**Figure 5-16**). This is also supported by the quantitative results shown in **Figure 5-17**, where the relative test line intensities for the conventional LFA at 10^6 cfu/mL and the ACE-LFA 3.3×10^4 cfu/mL are comparable and the two curves are continuously separated by at least a 30-fold difference in the initial concentration of *E. coli* for approximately the same test line signal. We also found the detection limit of the LFA + ATPS (without the nanozyme-TMB enhancement) to be 3.3×10^5 cfu/mL, demonstrating a 3-fold improvement over the conventional LFA. This is similar to the expected 4-fold improvement in detection limit that would be due to the *E. coli* bacteria being effectively concentrated into the leading phase of the ATPS. This suggests that the nanozyme-TMB enhancement reaction alone was responsible for a 10-fold improvement in the LFA detection limit.

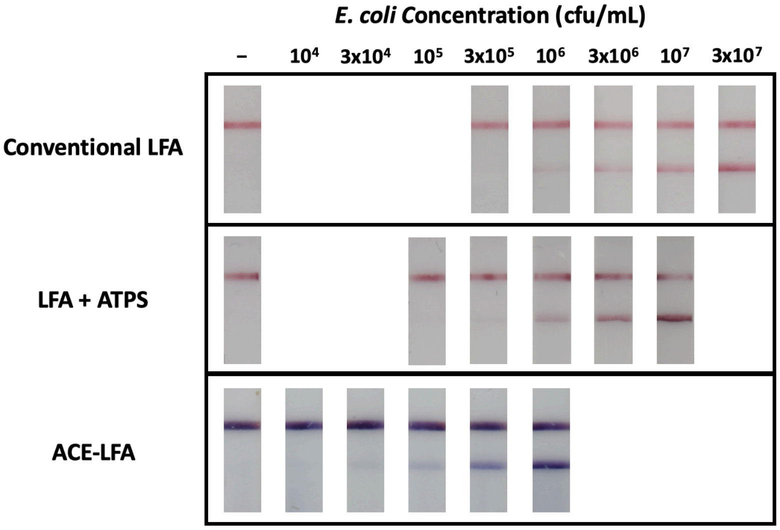

Figure 5-16 Conventional LFA, LFA + ATPS, and ACE-LFA for *E. coli* detection in buffer. Conventional LFA detects down to 10^6 cfu/mL, LFA + ATPS detects down to 3.3×10^5 cfu/mL, and the ACE-LFA detects down to 3.3×10^4 cfu/mL of *E. coli* overall, demonstrating a 30-fold improvement in detection limit when using ACE-LFA over the conventional LFA.

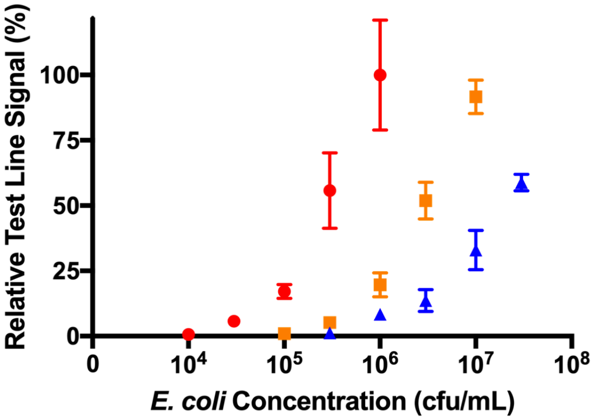

Figure 5-17 Quantification of test line intensity for detection of *E. coli* in buffer
Plot of quantified relative test line signals vs. *E. coli* concentration for the conventional LFA (blue ▲), LFA + ATPS (orange ■) and ACE-LFA (red ●). All of the data are presented as mean ± SD (n = 3).

The detection limit of the conventional LFA using GNPs was also compared to that of the conventional LFA using anti-*E. coli* PtGNPs (**Figure 5-18**). The same LFA test strip setup and procedure were used for both types of nanoprobes with the only difference being the type of nanoprobe dehydrated on the conjugate pad. A red signal was observed on the LFA tests using the GNPs while a pink signal was observed on the LFA tests using anti-*E. coli* PtGNPs. Despite the difference in the color, the detection limit was found to be 10^6 cfu/mL of *E. coli* for both types of nanoprobes. This confirmed that the 30-fold improvement in detection limit obtained from the ACE-LFA is a result of improvements from both biomarker preconcentration via the ATPS and signal enhancement via the ATPS-automated nanozyme reaction, and not any characteristic differences in the optical properties of the nanoprobes.

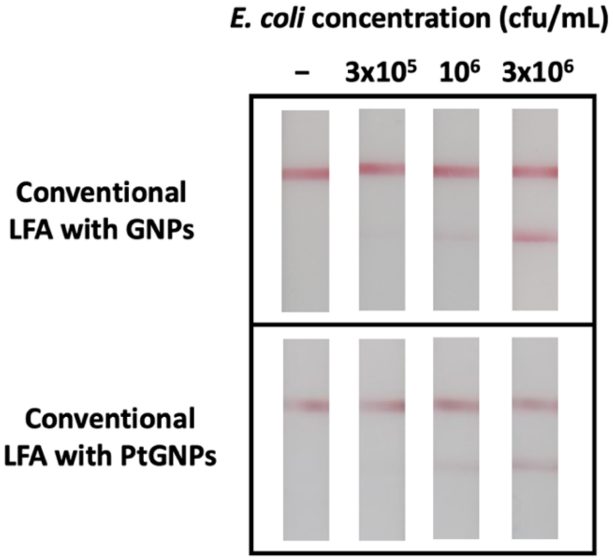

Figure 5-18 **Comparing the detection limit of the conventional LFA with GNPs versus PtGNPs.** Results indicate a conventional LFA detection limit of 10^6 cfu/mL for both the GNPs and PtGNPs.

In these experiments, we demonstrated that the ACE-LFA can achieve a 30-fold improvement in detection limit over the conventional LFA if the overall concentration of *E. coli* was the same between the ATPS of the ACE-LFA and the sample added to the conventional LFA. This comparison is suitable for a swab-based test where a swab must be agitated in an excess of a predetermined buffer to release and dilute the sample prior to application onto a test strip. Using this type of setup, a swab could be agitated in the ATPS of the ACE-LFA ATPS or a buffer of the same volume for the conventional LFA, thus resulting in a similar concentration of *E. coli* in both solutions. Additionally, while the above conventional LFA detection panels were performed with a 4-fold lower volume than the ACE-LFA (125 μL vs. 500 μL), increasing the conventional LFA sample volume to 500 μL did not improve the detection limit (**Figure 5-19**). This is most likely because the solution was too large for all of the *E. coli* in the sample to interact with all of the rehydrated anti-*E. coli* PtGNPs and completely flow past the test line, a common LFA problem. Therefore, one of the benefits of sample concentration techniques is that the biomarker present in a larger volume could be concentrated into a smaller volume where all of the biomarker could effectively interact with the PtGNPs and flow past the test line.

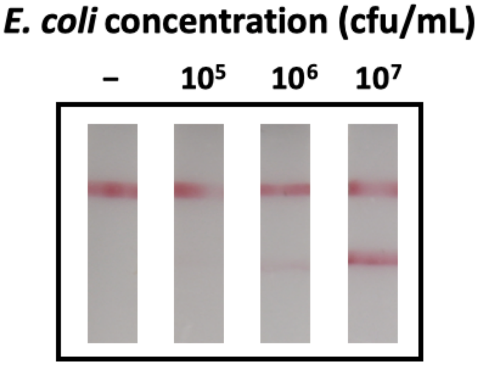

Figure 5-19 Detection panel for *E. coli* of the conventional LFA using a 500 μL sample volume

Finally, we evaluated the applicability of the ACE-LFA for detecting *E. coli* in a physiologically relevant liquid sample. *E. coli* was suspended in Surine Negative Urine Control, which is a Certified Reference Material for applications in clinical and analytical chemistry. For the conventional LFA, a 165 μL sample of *E. coli* in Surine was applied directly to the test strip. *E. coli* was successfully detected down to a concentration of 10^6 cfu/mL within 30 min (**Figure 5-20**). In the case of the ACE-LFA, the 165 μL *E. coli* sample was added to the ATPS phase forming components and enhancement reagents resulting in an approximate 3-fold dilution in the ATPS. The ACE-LFA was able to detect down to 10^5 cfu/mL of *E. coli* in the original Surine sample, demonstrating a 10-fold improvement in detection limit. This is expected because the urine sample was first diluted 3-fold in the ATPS prior to being reconcentrated in the leading phase. This dilution reduced the observed fold improvement in detection limit from the previous 30-fold to 10-fold. Ultimately, even with this dilution and using a more complex sample, we've demonstrated that the ACE-LFA can achieve a significant improvement in detection limit over the conventional LFA.

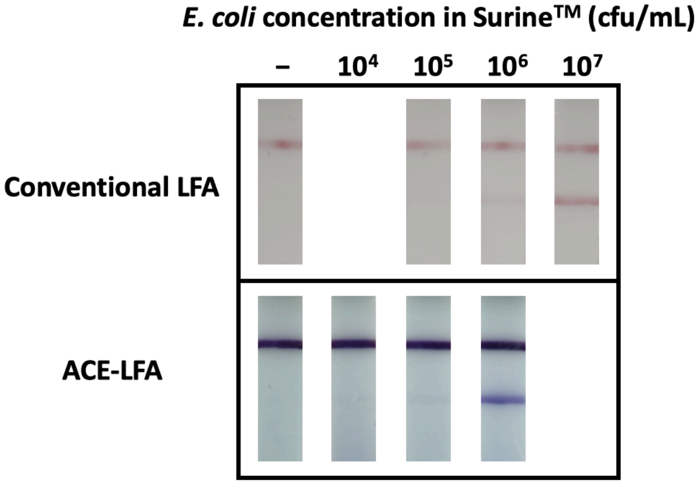

Figure 5-20 Comparison of conventional LFA and ACE-LFA for *E. coli* detection in Surine. Conventional LFA detects down to 10^6 cfu/mL while ACE-LFA detects down to 10^5 cfu/mL of *E. coli* in Surine, demonstrating a 10-fold improvement in detection limit

The importance of developing new methods of fluidic control for paper-based devices that require minimal user intervention and are compatible with high volume manufacturing was recently highlighted by Fu and Downs.[71] We believe that the ACE-LFA technology developed here is a significant contribution to addressing this need with several potential benefits over the previously developed automation techniques. For one, unlike many of the previous techniques, the device footprint of our ACE-LFA is very similar to the conventional LFA and it does not require complex paper geometries or electronic actuators. As a result, the ACE-LFA should be compatible with currently available high-volume LFA manufacturing techniques and will thus retain a low cost. Secondly, the ACE-LFA also has the potential to achieve higher levels of improvement over other techniques, because it can integrate both biomarker concentration and signal enhancement into a single device. This can be useful for the detection of biowarfare agents, infectious diseases, and food-borne illnesses, where it is desirable to detect the target at the lowest possible concentration.

The ACE-LFA procedure used in this work, which required an initial mixing step prior to the addition of the ATPS onto the test strip, is well suited for applications that require initial mixing into a predetermined buffer (i.e., swab-based diagnostics). However, other diagnostic applications may benefit from the direct application of a sample to the test without any mixing or sample dilution steps. To address this, our lab has recently demonstrated that ATPS components can be dehydrated on paper and then rehydrated upon addition of a sample fluid to induce phase separation and biomarker preconcentration without the need for any user mixing steps.[141] Future work will therefore aim to dehydrate the signal enhancement reagents along with the ATPS components to improve ease-of-use of the ACE-LFA for these applications.

5.5. Conclusion

In summary, we have developed a new method to automate sequential reagent delivery on paper-based devices using ATPS separation and flow on paper. The timing of reagent delivery could be controlled by altering the initial composition of the ATPS. To our knowledge, the ACE-LFA is the first reported technology with the capability to automate biomarker concentration, capture, and signal enhancement in a single paper-based device, as well as the first reported automation of a nanozyme signal enhancement reaction. Thus, this work plays a significant role in the advancement of paper-based devices with improved functionalities. Furthermore, with a 10-fold or greater improvement in detection limit within 30 min, the ACE-LFA has the ability to rapidly identify pathogens at lower concentrations than were previously detectable with the conventional LFA, all while maintaining a low cost, involving minimal user interaction, and requiring no electricity or laboratory equipment. Therefore, our ACE-LFA technology has the potential to greatly improve the state of disease detection in resource-limited regions which would ultimately lead to more effective patient management, treatment, and outbreak prevention.

Chapter 6. Nanozyme Signal Enhanced Detection of SARS-CoV-2 Nucleocapsid Protein on the Lateral-Flow Immunoassay

6.1. Introduction

The severe acute respiratory syndrome coronavirus 2 (SARS-CoV-2) has caused an ongoing and devastating pandemic which remains a major threat to global public health.[142] The N-protein is a major structural protein of coronaviruses which is involved in the packing of RNA within the virus. During the first week of infection, the N-protein is shed at relatively high concentrations into serum and nasopharyngeal fluid.[143] It has previously been detected to diagnose SARS-CoV infections, where the viral N-protein could be detected as early as 1 day after onset of symptoms in a variety of different bodily fluids.[144] The clinically relevant N-protein concentration circulating in blood for patients infected with SARS-CoV in the 2003 outbreak was determined to be between 0.1 ng/mL and 3.2 ng/mL. Due to similarities between SARS-CoV and SARS-CoV-2 viral pathogenesis, it has been suggested that the N-protein would also serve as an excellent antigen target for early SARS-CoV-2 detection.

Although serology lateral-flow immunoassays (LFAs) have been and are being commercially developed to detect for antibodies against SARS-CoV-2 (produced after the first week of infection), LFAs that directly detect the viral antigens (both spike protein and N-protein) during the early stages of infection (within the first week of infection) are just beginning to become available.[145,146] It is also important to note that most of the antigen-based LFAs available use nasopharyngeal swabs for sample collection, which do require some level of guidance to ensure proper sample collection and thus are not currently suitable for at-home testing. In fact, swabbing variability has been shown to impact even highly sensitive laboratory diagnostics for SARS-CoV-2.[147,148] An at-home diagnostic would allow for more widespread rapid detection of initial infection in a low-cost manner, which would allow patients to be treated and quarantined to prevent further outbreaks. LFAs can easily be performed at home with the correct sampling method, and its most common application is the over-the-counter pregnancy test. Such a rapid, inexpensive, and easy-to-use test will lead to widespread screening of healthy, asymptomatic, and symptomatic individuals. This blanket screening approach will play a significant role in allowing society to return to normal while maintaining safety. Although LFAs exhibit many of the characteristics desired for POC diagnostics, they commonly suffer from low sensitivity.

This low sensitivity is one reason for the currently available antigen-based LFAs to use the nasopharyngeal swab sampling approach. Overall, a nasopharyngeal swab has the potential to sample and capture the most virus due to the localization of SARS-COV-2 in the upper respiratory tract. However, this collection method does come with the downside of being prone to user error and variation depending on how the user inserts the swab into the nasal cavity. By developing a more sensitive version of the LFA, some of the sample fluids, such as blood, serum, and saliva, can be utilized which are easier to collect consistently, however they cannot be used with the currently available LFA technology due to having lower viral load or antigen concentration. Regardless of the sample type, an LFA with improved sensitivity can more effectively detect patients at their early stages of infection and allow for effective treatment and quarantining procedures to be implemented.[149]

6.2. Materials and Methods

6.2.1. Preparation of biotinylated anti-N-protein capture antibodies

Biotinylated anti-N-protein capture antibodies were prepared by NHS-ester linkage using NHS-PEG-biotin. 30 μL of a 3 mM NHS-PEG-biotin solution was then added to 100 μL of 0.5 mg/mL anti-N-protein antibodies (#40143-MM05, Sino Biological, Wayne, PA) in PBS and reacted for 30 min, allowing the NHS-PEG-biotin to conjugate onto the free surface primary amines of the antibodies. The conjugation reaction was stopped via buffer exchange in fresh PBS using the Zeba Spin Desalting Columns and diluted to a final volume of 150 μL. All reagents were purchased from Sigma-Aldrich unless otherwise noted.

6.2.2. Preparation of anti-N-protein detection antibody decorated platinum-coated gold nanozyme probes (anti-N-protein PtGNPs)

First, platinum-coated gold nanozymes (PtGNs) were synthesized using a protocol derived from Gao *et al*.[65] Briefly, 4 mL of 40 nm citrate-capped gold nanoparticles (GNs) (Nanocomposix, San Diego, CA) and 1827 μL of filtered ultrapure water were preheated to 90°C in an oil bath under magnetic stirring for 20 min. Following the preheating, 173 μL of a 0.82 mM chloroplatinic acid hydrate solution and 2 mL of a 3.3 mM ascorbic acid solution were injected separately into the gold nanoparticle suspension using a syringe pump at rates of 0.6 and 1.2 mL/h, respectively. The reaction was allowed to proceed for 30 min after the injection was complete.

To create anti-N-protein detection platinum-coated gold nanozyme probes (anti-N-protein PtGNPs), 30 μL of a 0.1 M sodium borate solution (pH 9) was first added to 1 mL of PtGNs. Then, 4 μg of primary anti-N-protein antibody (#40143-R001, Sino Biological, Wayne, PA) was added to the suspension and incubated for 30 min at room temperature (22 °C). 100 μL of a 10% (w/v) bovine serum albumin (BSA) in filtered ultrapure water solution was then added to the suspension and incubated for 10 min. Free antibodies were removed with three centrifugation cycles at 9000 RCF for 6 min each. For the first two cycles, the pellet was resuspended in 200 μL of 1% (w/v) BSA in filtered ultrapure water, and the final pellet was resuspended in 50 μL of a 0.1 M sodium borate (pH 9) solution.

6.2.3. Preparation of LFA test strip

To prepare the detection region of the LFA, proteins were first printed and immobilized on a nitrocellulose membrane using an Automated Lateral Flow Reagent Dispenser (Claremont BioSolutions LLC, Upland, CA) with the voltage setting at 4.5 V and a Fusion 200 syringe pump (Chemyx Inc, Stafford, TX) with a flow rate of 250 μL/min. The test line was formed by printing a solution of a 2 mg/mL polystreptavidin (Biotez, Berlin, Germany) solution in 25% (w/v) sucrose. The control line was formed by printing a solution of 0.5 mg/mL goat anti-rabbit IgG secondary antibody. The printed membrane was left in a vacuum-sealed desiccator overnight.

To create each nanozyme conjugate pad, 5 μL of anti-N-protein PtGNPs was diluted to 20 μL with an overall concentration of 5% w/w trehalose and 1% w/v BSA and then dehydrated onto a 5 mm × 10 mm fiberglass paper. The conjugate pads were dehydrated in a desiccator at 37 °C. To create each capture antibody pad, 3.3 μL of a 0.05 mg/mL biotinylated anti-N-protein capture antibody solution was diluted to 20 μL with an overall concentration of 5% (w/v) trehalose and 1% (w/v) BSA and then dehydrated onto a 5 mm × 10 mm fiberglass paper. The pads were dehydrated in a vacuum-sealed desiccator overnight.

To assemble the LFA test strip, the nitrocellulose membrane was first adhered to an adhesive backing. Individual strips were cut to be 5 mm in width. To each strip, a cotton linter absorbent pad was placed on the adhesive backing downstream of the control line, overlapping the nitrocellulose membrane by 2 mm. The PtGNP conjugate pad was placed on the adhesive backing upstream of the test line, overlapping the nitrocellulose membrane by 2 mm. The biotinylated-capture antibody pad was placed on the adhesive backing upstream and overlapping to the PtGNP conjugate pad by 2 mm. Assembled strips were stored in a bag containing Drierite desiccant.

6.2.4. Design and assembly of device for enhancement reagent storage and delivery on LFA

We designed a casing to eliminate the need for multiple liquid- and test strip-handling steps. This 3D printed device provides on-test liquid reagent storage, dehydrated enhancement reagents, and movable paper architecture which directs the flow of liquid through the LFA test strips. The three major components of the device are outlined in **Figure 6-1**. The parts shown in gray were 3D printed using an Ultimaker 3 (Ultimaker B.V., Geldermalsen, Netherlands) out of Ultimaker CPE filament (Co-polyester).

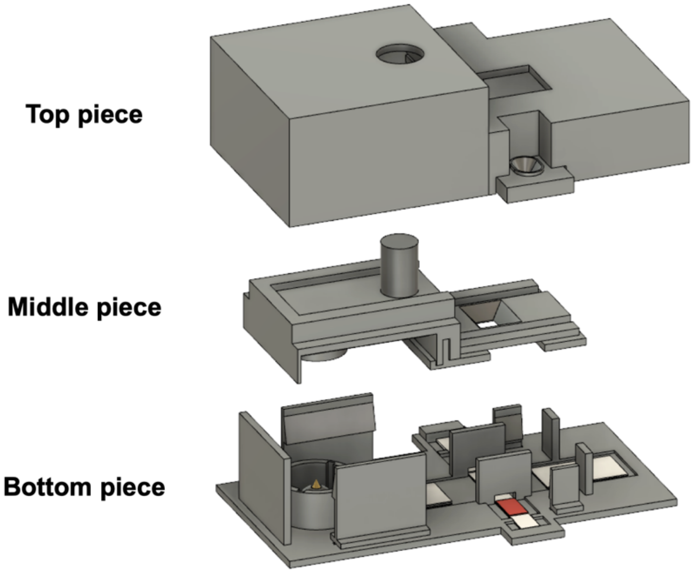

Figure 6-1 Design of the three main casing pieces for nanozyme signal enhancement of the LFA

The bottom piece of the casing along with the inserted paper pad and test strip components are detailed in **Figure 6-2**. This bottom component holds the LFA test strip which is composed of the absorbent pad, detection zone, anti-N-protein PtGNP conjugate pad, and biotinylated-anti-N protein antibody pad. The enhancement buffer release well is an enclosed, hollow cylinder with a spiked dome in the center. The dome is 3D printed with a nail housed inside of it which serves to rupture a foil sealed buffer reservoir on the middle piece of the casing. 0.2 g of sodium perborate was sprinkled on an adhesive backing surrounding the dome and then covered with a ring of fiberglass paper. A 62.5 µL solution of 6.5 mM 3,3’,5,5’-tetramethylbenzidine (TMB), 15% (w/v) trehalose, and 20% (w/v) dimethylformamide (DMF) in 0.1 M sodium citrate buffer (pH 5) was dehydrated onto a 13 mm × 12 mm fiber glass pad overnight in a vacuum sealed desiccator to create the TMB pad. The enhancement reagent absorbent pad is composed of a 13 mm × 23 mm cotton fiber pad. The four aligning snap fit joints hold the middle piece of the casing in a lifted position until the user presses down on it. The middle piece will then snap into place and be held down in a constant position by the snap fit joints.

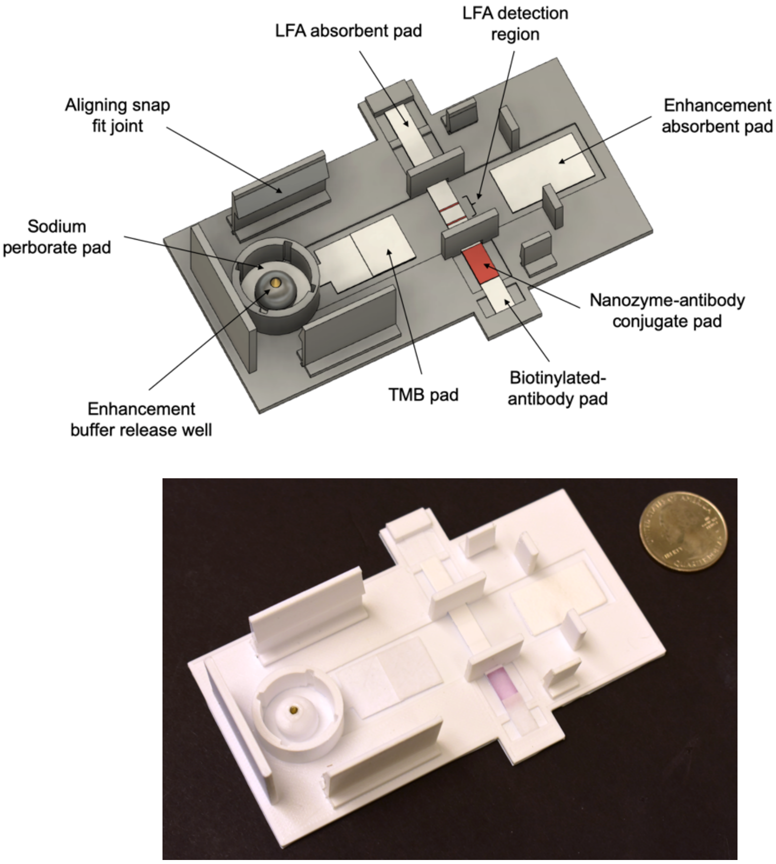

Figure 6-2 Detailed view of bottom piece of casing.
Labeled CAD drawing of bottom piece of casing (top). Photograph of 3D printed bottom piece of casing with LFA test strip and enhancement reagent paper pads in position. US quarter included for size comparison.

The movable middle piece of the casing, shown in **Figure 6-3**, contains the enhancement buffer reservoir and two connector pads. The left pad is made up of fiberglass paper while the right pad is a cotton fiber pad. The enhancement buffer, which will resolubilize the sodium perborate and TMB during the assay, was stored within the reservoir of the middle piece. To fill the buffer within the reservoir, 750 μL of 1% (w/v) dextran sulfate in 0.1 M sodium citrate buffer (pH 5) was pipetted into the reservoir. To seal the liquid in the reservoir, a sheet of mylar foil was placed on top of the reservoir and heat was applied using a hot iron for 5 s followed by complete cooling. This was repeated for a total of 5 times to ensure a tight seal. The top piece of the casing serves to help hold the other components in place and protect them from external and environmental factors. It also contains a sample well which is located above the capture antibody pad when the device is fully assembled and a viewing window to observe the detection results (**Figure 6-4**).

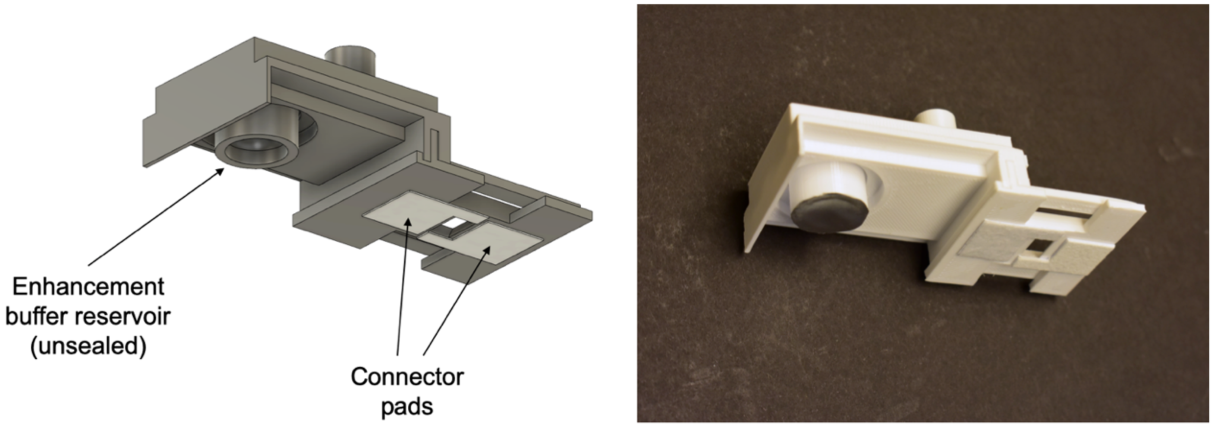

Figure 6-3 Detailed view of middle piece of casing.
CAD drawing (left) and 3D printed piece (right) showing the underside view of the middle piece of the casing showing the location of the enhancement buffer fluid reservoir and the paper connector pads.

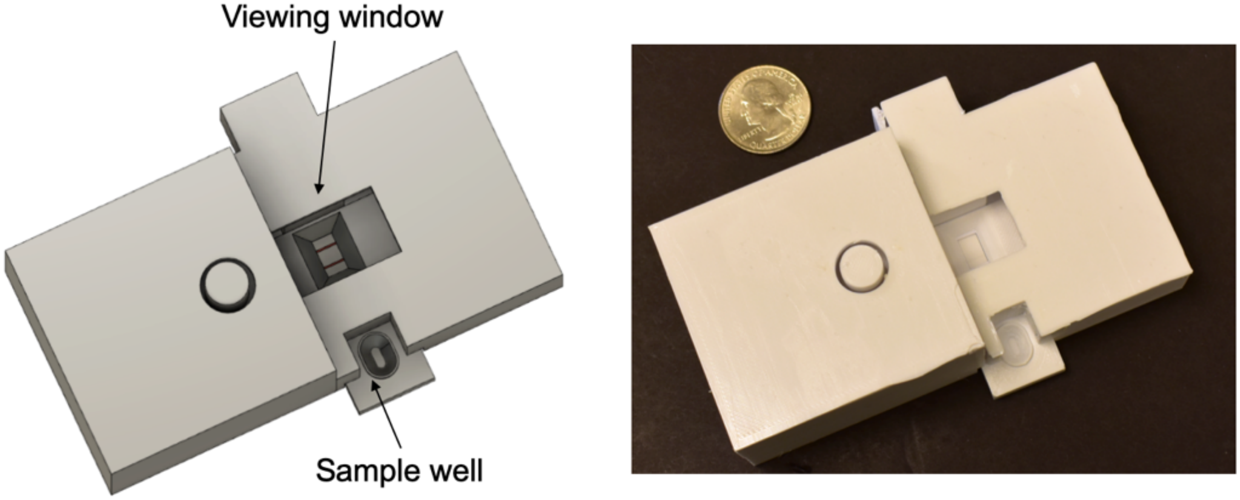

Figure 6-4 Detailed view of full casing assembly
CAD drawing of (left) and 3D printed (right) full casing assembly with labeled viewing window and sample pad. US quarter included for size comparison.

6.2.5. Detection of N-protein in human serum with nanozyme signal enhanced LFA

To detect for N-protein using our nanozyme signal enhanced LFA, a 25 µL human serum sample containing varying concentrations of N-protein is added to the sample well on the LFA (above the biotinylated capture antibody pad). This is immediately followed by the application of 75 µL of chase buffer (2% polyvinylpyrrolidone 10kDa, 0.2 % BSA, 0.2% Tween 20, and 0.2% casein in 0.1 M potassium phosphate, pH 7.2). After 20 min, the user would press down the middle piece of the casing (**Figure 6-5**). The movement of the middle casing piece results in the rupture of the mylar seal to release the enhancement buffer and also serves to lower the connector pads to provide a continuous flow path for the enhancement reagents to flow through the LFA strip. Final results were observed after 20 min of enhancement. In the preliminary detection results shown here, the top piece of the casing was not utilized and the enhancement buffer was simply pipetted into the release well where the sodium perborate was stored, rather than the buffer being sealed in the reservoir on the middle piece of the casing. This was done to conserve materials and time during these stages of development. Results were photographed before and after the signal enhancement reaction with a Nikon D3400 digital camera (Nikon, Tokyo, Japan) in a controlled lighting environment.

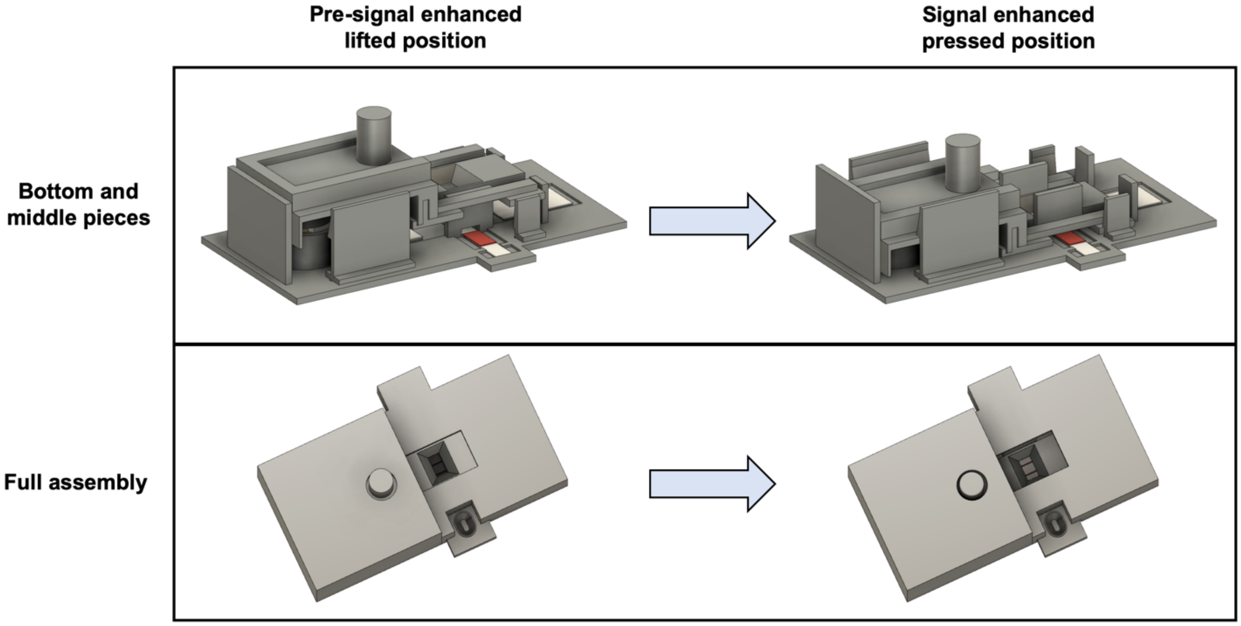

Figure 6-5 CAD drawings showing the casing before and after pressing the middle piece

6.3. Results and Discussion

6.3.1. Demonstration of improved N-protein detection using nanozyme signal enhancement

The operation of our device for the nanozyme signal enhanced detection of N-protein occurs in two main steps. The first is the analyte capture step and the second is the signal enhancement step (**Figure 6-6**). The user first applies the serum sample to the sample well immediately followed by the addition of the chase buffer. The liquid will first resolubilize the biotinylated capture anti-N-protein antibody followed by the anti-N-protein PtGNPs. These antibody species will bind to any N-protein in the sample resulting in the formation of sandwich complexes. As these complexes flow through the LFA strip, they will be captured at the test line due to the strong biotin-streptavidin interaction between the biotinylated capture antibody and the streptavidin immobilized on the test line. This will ultimately result in the capture of PtGNPs at the test line region. In the case of a negative sample where no N-protein is present, no sandwich complex will form and therefore even though the biotinylated capture antibody will bind to the streptavidin at the test line, no PtGNPs will be captured. Regardless of the sample being positive or negative for N-protein, any PtGNPs that do not get captured at the test line will be able to be captured by the secondary antibody at the control line to indicate that the sample flowed properly through the test strip.

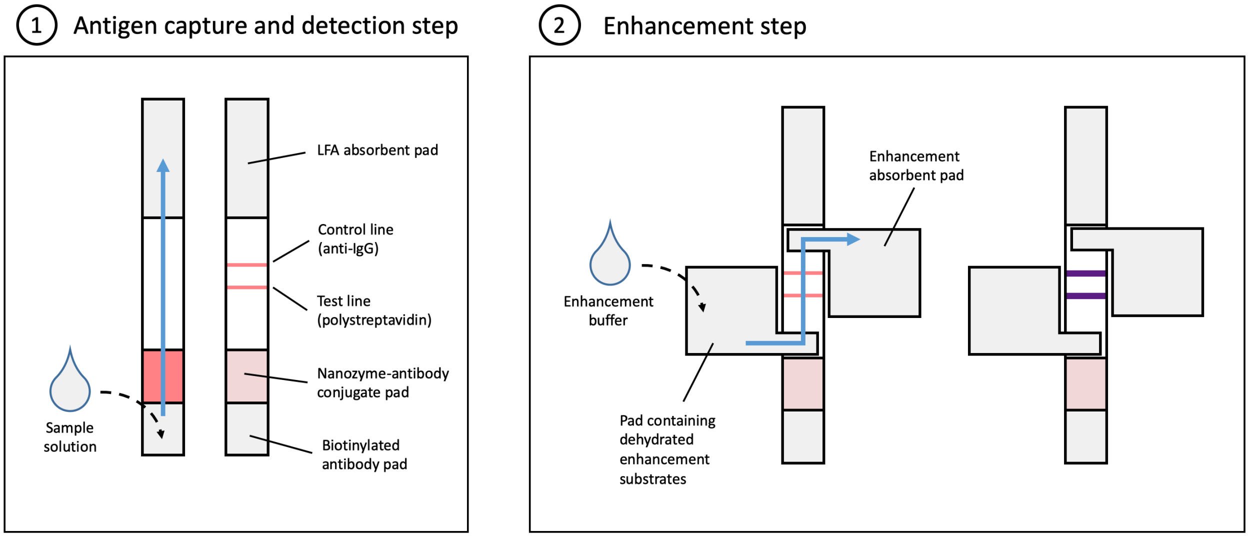

Figure 6-6 Simplified schematic of assay steps and paper segments touching the LFA test strip
(1) Sample is applied to the sample well above the test strip where biotinylated antibody and PtGNPs are rehydrated and antigen capture occurs at detection zone. (2) After pressing the middle piece of the casing down, enhancement buffer is released to rehydrate dehydrated enhancement reagents and flow through the test strip resulting in signal enhancement at detection zone.

After 20 min, the user will press down on the button connected to the middle piece of the casing. This lowers the middle piece where it snaps into place with the connector pads bridging gaps between the dehydrated TMB pad and the LFA strip, as well as the LFA strip and the enhancement absorbent pad. Additionally, as the middle piece is lowered, the mylar seal on the enhancement buffer reservoir becomes ruptured by the pointed dome which allows the enhancement buffer into flow into the release well. Once released, the buffer resolubilizes the sodium perborate, followed by the TMB. This enhancement solution then flows through the LFA test strip and into the enhancement absorbent pad. As the solution passes the detection zone, any PtGNPs bound to the test line will catalyze the oxidation of TMB to TMB^{+}. The TMB^{+} will complex with the negatively charged dextran sulfate, leading to the formation of an insoluble purple product which becomes deposited at the test line. This results in the enhancement of the test line signal. As mentioned in *Section 6.2.5*, for the preliminary detection panel results presented, the top piece of the casing and the reservoir on the middle piece of the casing were not utilized to save materials. The enhancement buffer was simply pipetted into the well containing the sodium perborate. We have performed experiments with the full setup and it performs identical to that used in these experiments.

To evaluate the performance of this assay, we tested samples containing 0, 1, 3, and 10 ng/mL of N-protein spiked into human serum. The results are shown below in **Figure 6-7**. Before the enhancement step, a clearly visible test line is present at 3 ng/mL but not at 1 ng/mL, indicating a detection limit of 3 ng/mL. After enhancement, the test lines at 3 and 10 ng/mL become significantly darker and a visible test line also appears at 1 ng/mL, demonstrating at least a 3-fold improvement in detection limit. These results demonstrate the ability of our nanozyme signal enhanced assay to detect for N-protein and improve detection limit when compared to the unenhanced LFA. Additionally, the current detection limit falls within the concentration range of 0.1 to 3 ng/mL of N-protein which was found to be the window of N-serum protein concentrations to achieve sensitive detection of SARS in 2003.[144] Due to high similarities in viral genome and pathogenesis, it is likely that a similar concentration range is relevant for SARS-COV-2. Besides serum N-protein detection, our signal enhanced assay would be suitable for the detection of N-protein in swab-based samples and could also be adapted for the detection of SARS-CoV-2 spike protein or other antigen targets.

While our device has a more complex construction than the conventional LFA, the casing can still be mass produced using injection molding processes and the test strips can be created using existing diagnostic manufacturing infrastructure. However, compared to other approaches to improve sensitivity such as the integration of electronic readers, our device is much less complex where it will be easier to scale production and be more affordable to the end user.[150] The steps for operation are also not much more difficult than the conventional LFA, requiring just an additional press of a button. Future work will focus on increasing the degree of signal enhancement through reagent optimization, performing a more thorough study of the detection limit to compare with other diagnostic assays, and evaluate the shelf life of the complete device.

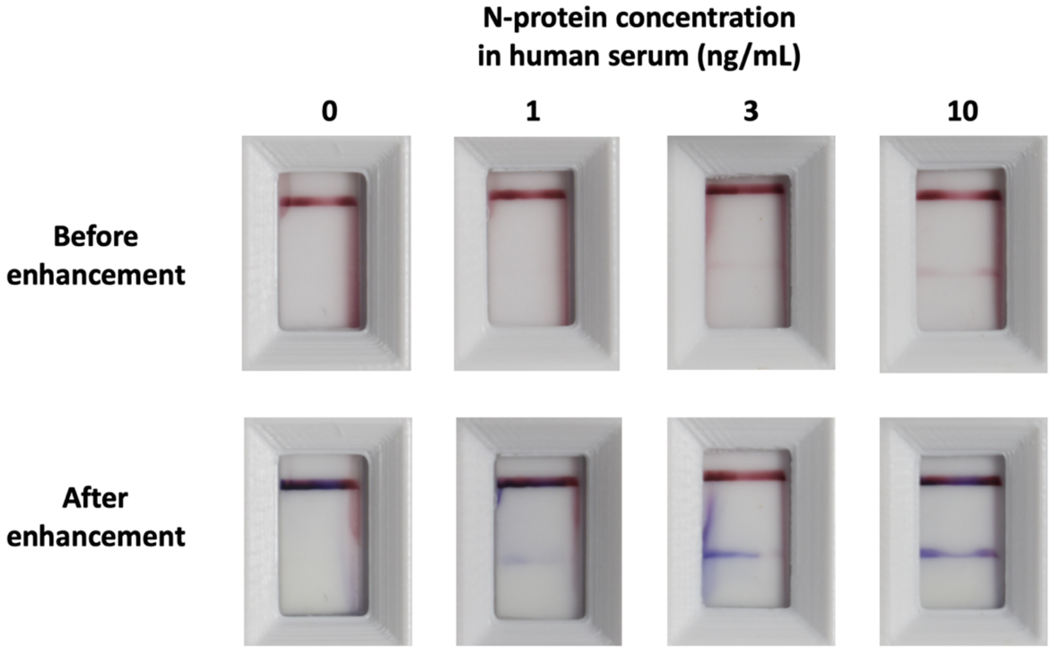

Figure 6-7 Detection of the N-protein of SARS-CoV-2 in human serum using nanozyme signal enhanced LFA
Detection limit before enhancement is 3 ng/mL while after enhancement it is 1 ng/mL, demonstrating at least a 3-fold improvement in detection limit and detection of N-protein within the desired concentration range.

6.4. Conclusion

In summary, we have developed a nanozyme signal enhanced LFA for the improved detection of the N-protein of SARS-CoV-2. A 3D printable casing was designed, which stored all assay components including the LFA test strip, dehydrated signal enhancement reagents, and a sealed chamber with stored liquid enhancement buffer. In preliminary testing, our device was able to improve the detection of N-protein by at least 3-fold. The development of devices that have the ability to detect for SARS-CoV-2 antigen biomarkers with improved sensitivity, while maintaining a user-friendly design and scalable manufacturing is vital to increasing the frequency in screening asymptomatic individuals. This has the potential to significantly improve the response to the COVID-19 pandemic by effectively detecting patients at their early stages of infection and allowing for effective treatment and quarantining procedures to be implemented.

Chapter 7. Rapid Detection of SARS-CoV-2 Nucleocapsid Protein on the Lateral-Flow Immunoassay Using Novel Monobody Binders

7.1. Introduction

As discussed in *Chapter 6,* the severe acute respiratory syndrome coronavirus 2 (SARS-CoV-2) has caused an ongoing and devastating pandemic which remains a major threat to global public health. The diagnosis of SARS-COV-2 infections is essential to identify and quarantine infected individuals, thus lessening the spread of the infection. The antibody-specific serology LFAs were developed many months before antigen-based LFAs due to the relatively long time that is needed to produce high quality monoclonal antibodies against novel antigenic targets using hybridomas. Beyond the initial development time, scaling up the production of monoclonal antibodies to meet the global demands of for mass asymptomatic testing is not a trivial matter. In a global pandemic of this scale, having the ability to produce antigen-based assays without waiting months for monoclonal antibody development and production as well as having the ability for a more easily scalable manufacturing could allow for significantly more widespread testing and quarantining to prevent future outbreaks.

Here we developed an LFA platform with the potential for improved scalability which utilizes fibronectin-based antibody mimetics, also called monobodies, as a capture protein in place of a monoclonal antibody. These monobodies were produced using the mRNA display method, where a library of 10.5 million amino acid variants was screened and the optimal sequences were determined within just a few weeks. In addition to the quick initial screening of the monobodies, they were recombinantly produced in *E. coli*, which makes it possible to scale up manufacturing production to meet global demands more rapidly and affordably than with monoclonal antibodies.

7.2. Materials and Methods

7.2.1. *Biotinylation of anti-N-protein NN2 monobody*

Monobodies that could bind to N-protein were produced by Ren and coworkers.[151] Biotinylated monobodies were prepared by NHS-ester linkage using NHS-PEG-biotin. Briefly, the Tris-buffered saline storage buffer (pH 8) for the monobodies (0.5 mg/mL, 50 µL) was exchanged with phosphate-buffered saline (PBS, pH 7.4) using a Zeba Spin Desalting column (MWCO of 7000). 1.7 µL of a 3 mM NHS-PEG-biotin solution was then added to the 50 µL of 0.5 mg/mL monobodies in PBS and reacted for 30 min, allowing the NHS-PEG-biotin to conjugate onto the free surface primary amines of the monobodies. The conjugation reaction was stopped via buffer exchange in fresh PBS using the Zeba Spin Desalting Columns and diluted to a final volume of 150 µL. All reagents were purchased from Sigma-Aldrich unless otherwise noted.

7.2.2. *Preparation of anti-N-protein antibody gold nanoshell conjugates*

Anti-N-protein antibody functionalized gold nanoshells were created using a NHS-ester covalent chemistry method. First, 8 µg of EDC (8 µL of 1 mg/mL EDC) and 16 µg (16 µL of 1 mg/mL Sulfo-NHS) were added to 100 µL of 150 nm BioReady Carboxyl Gold Nanoshells (nanoComposix, San Diego, CA). The suspension was incubated for 30 min on a nutator followed by centrifugation at 2000 RCF for 5 min. The supernatant was discarded to remove excess EDC/sulfo-NHS and the pellet was resuspended in 100 µL of reaction buffer (0.5% w/w 20kDa polyethylene glycol in 0.1x PBS, pH 7.4). Next, 2.5 µg of rabbit anti-N-protein monoclonal antibody clone #001 (Sino biological, Wayne, PA) was added to the suspension and allowed to react for 60 min while shaking at 700 RPM on a Compact Digital Microplate Shaker (Thermo Fisher Scientific, Waltham, MA). To deactivate any remaining NHS-ester, 5 µL of 1 M Tris buffer (pH 8) was added to the suspension and incubated for 10 min. To purify our conjugates and remove any free antibody, the suspension was then centrifuged for 5 min at 2000 RCF. The supernatant was discarded and the pellet was resuspended in 100 μL of reaction buffer. The suspension was centrifuged again and resuspended in 100 μL of a conjugate dilution buffer (0.5% w/w bovine serum albumin and 0.5% w/w Tween 20 in 10 mM sodium borate, pH 9). Lastly, the conjugate suspension was sonicated for 3 min to completely resuspend the particles.

7.2.3. Preparation of lateral-flow immunoassay (LFA) test strips

To prepare the detection region of the LFA, proteins were first printed and immobilized on a nitrocellulose membrane using an Automated Lateral Flow Reagent Dispenser (Claremont BioSolutions LLC, Upland, CA) with the voltage setting at 4.5 V and a Fusion 200 syringe pump (Chemyx Inc, Stafford, TX) with a flow rate of 250 μL/min. The test line was formed by printing a solution of a 2 mg/mL polystreptavidin (Biotez, Berlin, Germany) solution in 25% (w/v) sucrose. The control line was formed by printing a solution of 0.5 mg/mL goat anti-rabbit IgG secondary antibody. The printed membrane was left in a vacuum-sealed dessicator overnight.

To assemble the LFA test strip, the nitrocellulose membrane was first adhered to an adhesive backing. A cotton linter absorbent pad was placed on the adhesive backing downstream of the control line, overlapping the nitrocellulose membrane by 2 mm. A fiberglass sample pad was placed on the adhesive backing upstream of the test line, overlapping the nitrocellulose membrane by 2 mm. Individual test strips were cut to be 3 mm in width and stored in a bag with Drierite desiccant.

*7.2.4. Detection of N-*protein *on the lateral-flow immunoassay*

The perform the LFA for the detection of N-protein, a test strip was dipped vertically into a solution containing a 25 μL sample of N-protein in either FBS (Invitrogen, Carlsbad, CA) or pooled human serum (Innovative Research, Novi, MI), 18 μL of running buffer (2% w/w 10 kDa polyvinylpyrrolidone, 0.2 % BSA, 0.2% casein, and 0.2% Tween 20 in 50 mM potassium phosphate buffer pH, 7.4), 5 μL of anti-N-protein gold nanoshell conjugates, and 2 μL of biotinylated monobody. After 20 min, the results were observed and photographs were taken with a Nikon D3400 digital camera (Nikon, Tokyo, Japan) in a controlled lighting environment. All LFA experiments were performed in triplicate. To quantify the test line intensities, images of the LFA test strips were processed using a custom MATLAB script developed by our lab.[57] The visible limit of detection was determined as the lowest concentration that could produce a test line that is reliably distinguishable by the naked-eye, and the statistical limit of detection was calculated based on the guidelines provided by the National Committee for Clinical Laboratory Standards for a relatively small sample size with unknown population variance detailed below.[152,153]

7.2.5. Statistical calculation of LFA limit of blank and limit of detection

The statistical limit of detection was calculated in MATLAB using the guidelines provided by the National Committee for Clinical Laboratory Standards for a relatively small sample size with unknown population variance which is described briefly below. First, the limit of blank threshold (L_c) was calculated using Eq. (59):

$$L_c = \mu_{blank} + 2.920\sigma_{blank} \tag{59}$$

where μ_{blank} is the mean signal intensity of the negative control, and σ_{blank} is the standard deviation of the negative control. The blank standard deviation multiplier, 2.920, was determined from a t-distribution table with 2 degrees of freedom and $\alpha = 0.05$. In this case the degrees of freedom was calculated from $n-1$, where n is the number of replicates tested which in our case is 3.

Next, a pooled standard deviation was calculated for low concentration positive tests using Eq. (60):

$$\sigma_{test} = \sqrt{\frac{\sum_{i=1}^{m} \sigma_i^2}{m}} \tag{60}$$

where σ_i is the standard deviation of test line signal intensities calculated from n replicates of the i th concentration, and m is the total number of concentrations included in the pool. For both FBS and human serum calculation, the standard deviation of test line signals from the 3 lowest positive concentrations was included (0.1, 0.3, and 0.6 ng/mL for FBS, and 0.3, 1, and 3 ng/mL for human serum).

Third, the signal threshold for the limit of detection (L_D) was calculated using Eq. (61):

$$L_D = L_C + 1.934\sigma_{test} \tag{61}$$

The pooled standard deviation multiplier, 1.934, was also determined from a t-distribution table with 6 degrees of freedom and $\alpha = 0.05$. The degrees of freedom here is calculated as $m(n-1)$, where the number of concentrations pooled is $m = 3$ and the number of replicates for each concentration is $n = 3$.

With L_D calculated, a curve fit was performed using a 4PL calibration curve, in order to translate the L_D in the signal domain to an estimated LOD in the concentration domain. Prior to the curve fit, the analyte concentration C was first shifted by adding 2 to each value and then transformed to a base 10 logarithmic scale. The +2 shift is used to allow the signal measurements for the blank concentration to be included after the log transformation. An equation for the 4 PL curve, shown below as Eq. (62), was fit using a nonlinear least-squares approach in MATLAB.

$$S = \frac{a-d}{1+\left(\frac{\log(C+2)}{c}\right)^{b}} + d \tag{62}$$

S is the signal intensity, and a, b, c, and d are parameters that are fit to create a curve that best represents the data. Equation (62) is then rearranged and solved for C as a function of S. The concentration at the LOD is finally calculated by plugging in L_D for S as well as the values for the parameters determined from the lease-squares regression. For FBS, the LOD was calculated to be 0.23 ng/mL, whereas for human serum it was calculated to be 4.9 ng/mL

7.3. Results and Discussion

7.3.1. Detection of N-protein on the lateral-flow immunoassay using monobodies

We developed an LFA using a biotinylated anti-N-terminal nucleocapsid protein monobody as a capture protein and monoclonal anti-nucleocapsid protein antibody-conjugated gold nanoshells as a detection probe. The LFA test strip contained polystreptavidin immobilized at the test line and anti-rabbit IgG secondary antibody at the control line. To evaluate the performance of the LFA, the sample solution to be tested was first mixed with the running buffer, biotinylated monobody, and antibody-nanoshell conjugates. This mixture was then applied to the LFA test strip and results were interpreted after 20 min. When testing samples of N-protein spiked in FBS, we determined the visible limit of detection of our LFA to be 0.6 ng/mL, because this was the lowest concentration that produced a test line that could be reliably distinguished by the naked eye (**Figure 7-1**). After quantifying the images of our LFA test strips using a MATLAB script developed by our lab and performing statistical analysis, a limit of detection was calculated to be 0.23 ng/mL (**Figure 7-2**). This demonstrates that the combination of our LFA along with image analysis has the potential to produce a lower limit of detection than the LFA alone. This falls within the concentration range of 0.1 to 3 ng/mL of N-protein which was found to be the window of N-serum protein concentrations to achieve sensitive detection of SARS in 2004.[144] Due to high similarities in viral genome and pathogenesis, it is likely that a similar concentration range is relevant for SARS-COV-2.

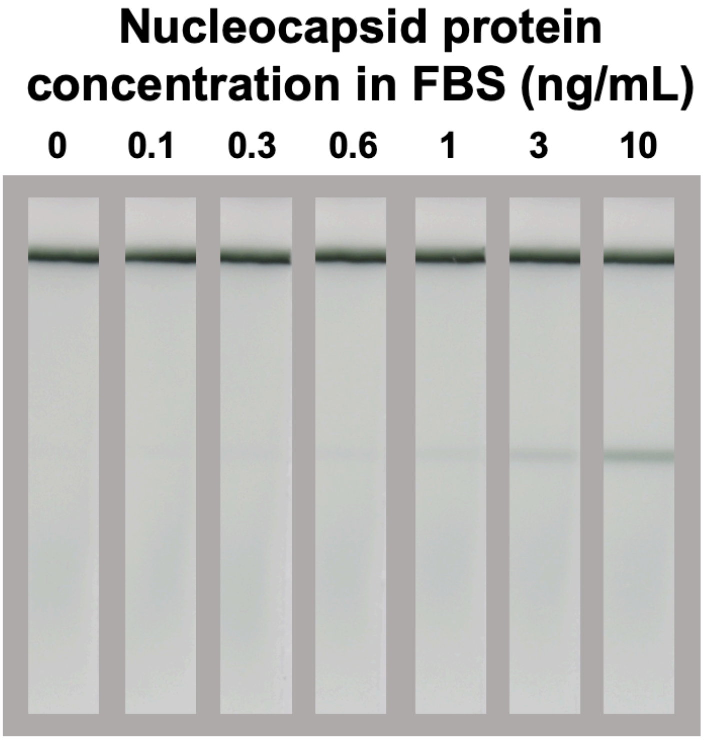

Figure 7-1 LFA detection of N-protein in FBS
Visible limit of detection of 0.6 ng/mL of N-protein. All data presented as mean ± SD (n = 3).

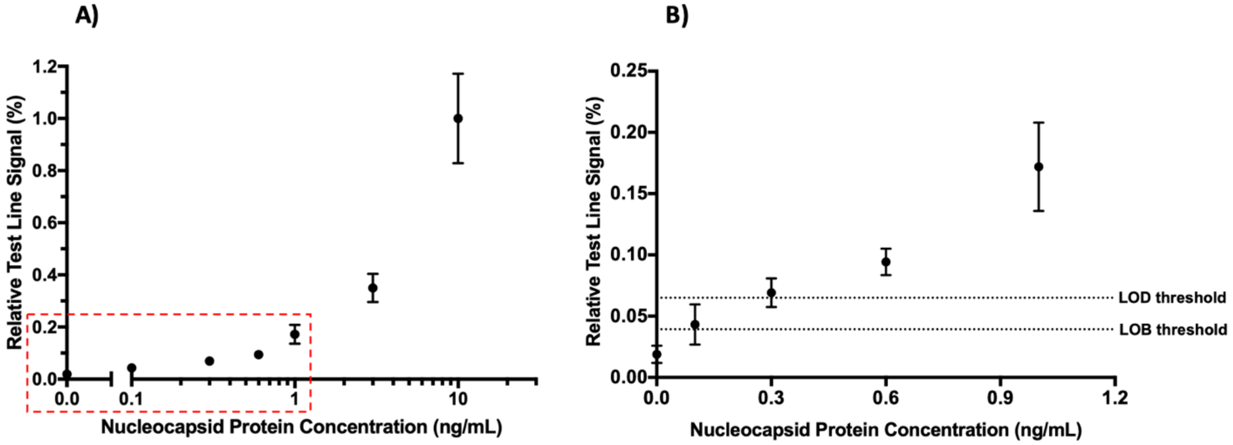

Figure 7-2 Quantification of N-protein detection in FBS on LFA
A) Quantification of full detection range. B) Expanded region shown around the lower N-protein concentration (boxed in A) with statistical limit of blank (LOB) and limit of detection (LOD) signal thresholds marked. LOD concentration calculated to be 0.23 ng/mL of N-protein.

Detection of N-protein in human serum resulted in a visible limit of detection of 6 ng/mL (**Figure 7-3**). Image quantification and statistical analysis resulted in a calculated limit of detection of 4.9 ng/mL N-protein in human serum **(Figure 7-4)**. The increase in detection limit that is observed when switching from FBS to human serum may be due to interference from the higher concentration of antibodies and complement proteins present in human serum.[154] While these observed limits of detection limits are above the desired concentration range of 0.1 to 3 ng/mL, the detection limit can be lowered in the future by integrating it with the nanozyme signal enhancement technologies discussed in *Chapters 5* and *6*, as well as further screening of the monobody mRNA library. To our knowledge, this is the first reported use of monobodies as a binding protein for the lateral-flow immunoassay.

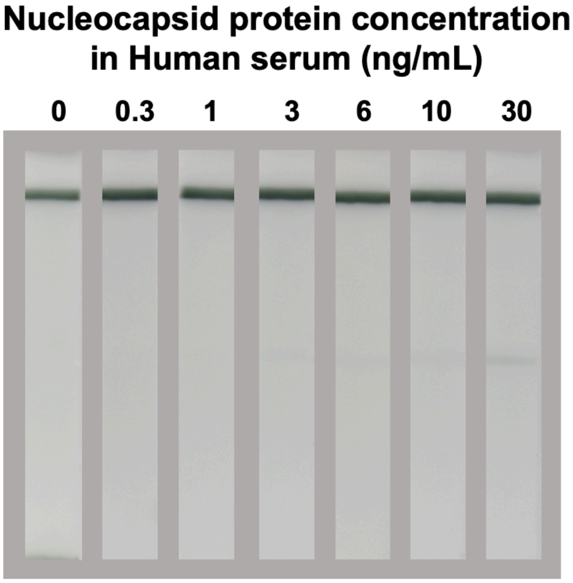

Figure 7-3 LFA detection of N-protein in human serum
Visible limit of detection of 6 ng/mL of N-protein. All data presented as mean ± SD (n = 3).

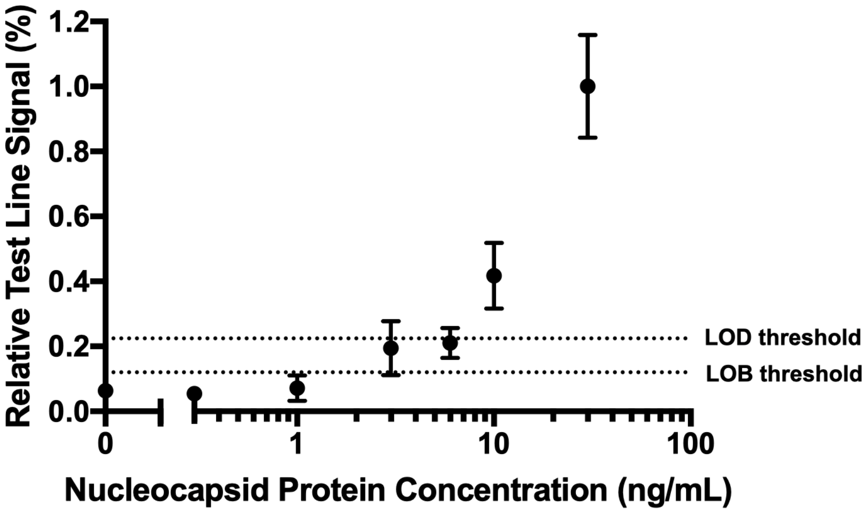

Figure 7-4 Quantification of N-protein detection in human serum on LFA.
Statistical limit of blank (LOB) and limit of detection (LOD) signal thresholds are shown. LOD concentration calculated to be 4.9 ng/mL of N-protein. All data presented as mean ± SD (n = 3).

7.4. Conclusion

In summary, we have developed a lateral-flow immunoassay that detects for N-protein using a combination of antibody and novel monobodies. To our knowledge, this is the first reported integration of monobodies with the LFA. Using this LFA, the N-protein was successfully detected at the low ng/mL range, rivaling the detection limit of fully antibody-based LFAs. The introduction of monobodies into the rapid diagnostic testing landscape has the potential to greatly speed up the assay development process due to their faster development time compared to antibodies. This has the potential to significantly improve the response to new emerging pathogens such as SARS-COV-2, ultimately saving resources and countless lives.

References

1. Top 10 causes of death. *World Heal. Organ.* Geneva, Switzerland (2016).
2. Mouton, C. P., Hayden, M. & Southerland, J. H. Cardiovascular Health Disparities in Underserved Populations. *Prim. Care Clin. Off. Pract.* **44**, 37–71 (2017).
3. Yager, P., Domingo, G. J. & Gerdes, J. Point-of-care diagnostics for global health. *Annu. Rev. Biomed. Eng.* **10**, 107–144 (2008).
4. Yager, P. *et al.* Microfluidic diagnostic technologies for global public health. *Nature* **442**, 412–418 (2006).
5. Cheung, S. F., Cheng, S. K. L. & Kamei, D. T. Paper-Based Systems for Point-of-Care Biosensing. *J. Lab. Autom.* **20**, 316–333 (2015).
6. Martinez, A. W., Phillips, S. T., Whitesides, G. M. & Carrilho, E. Diagnostics for the developing world: Microfluidic paper-based analytical devices. *Anal. Chem.* **82**, 3–10 (2010).
7. Mudanyali, O. *et al.* Integrated rapid-diagnostic-test reader platform on a cellphone. *Lab Chip* **12**, 2678–86 (2012).
8. Chen, Y. *et al.* Near-infrared fluorescence-based multiplex lateral flow immunoassay for the simultaneous detection of four antibiotic residue families in milk. *Biosens. Bioelectron.* **79**, 430–434 (2016).
9. Akanda, M. R. *et al.* An interference-free and rapid electrochemical lateral-flow immunoassay for one-step ultrasensitive detection with serum. *Analyst* **139**, 1420 (2014).
10. Workman, S. *et al.* Rapid detection of HIV-1 p24 antigen using magnetic immuno-chromatography (MICT). *J. Virol. Methods* **160**, 14–21 (2009).
11. Wang, Y. *et al.* Thermal Contrast Amplification Reader Yielding 8-Fold Analytical

Improvement for Disease Detection with Lateral Flow Assays. *Anal. Chem.* **88**, 11774–11782 (2016).

12. Zhu, X. *et al.* Using a glucose meter to quantitatively detect disease biomarkers through a universal nanozyme integrated lateral fluidic sensing platform. *Biosens. Bioelectron.* **126**, 690–696 (2019).
13. Lin, B. *et al.* Lateral flow assay with pressure meter readout for rapid point-of-care detection of disease-associated protein. *Lab Chip* **18**, 965–970 (2018).
14. Fu, E. Enabling robust quantitative readout in an equipment-free model of device development. *Analyst* **139**, 4750 (2014).
15. Lou, S. C., Patel, C., Ching, S. & Gordon, J. One-step competitive immunochromatographic assay for semiquantitative determination of lipoprotein(a) in plasma. *Clin. Chem.* **39**, 619–624 (1993).
16. Leung, W. *et al.* InfectCheck CRP barcode-style lateral flow assay for semi-quantitative detection of C-reactive protein in distinguishing between bacterial and viral infections. *J. Immunol. Methods* **336**, 30–36 (2008).
17. Panferov, V. G., Safenkova, I. V, Zherdev, A. V & Dzantiev, B. B. Setting up the cut-off level of a sensitive barcode lateral flow assay with magnetic nanoparticles. *Talanta* **164**, 69–76 (2017).
18. Gasperino, D. J. *et al.* Threshold-Based Quantification in a Multiline Lateral Flow Assay via Computationally Designed Capture Efficiency. *Anal. Chem.* **90**, 6643–6650 (2018).
19. Li, Z., Chen, H. & Wang, P. Lateral flow assay ruler for quantitative and rapid point-of-care testing. *Analyst* (2019). doi:10.1039/C9AN00374F
20. Papavassiliou, G. C. Optical properties of small inorganic and organic metal particles. *Prog.*

Solid State Chem. **12**, 185–271 (1979).

21. Petryayeva, E. & Krull, U. J. Localized surface plasmon resonance: Nanostructures, bioassays and biosensing-A review. *Anal. Chim. Acta* **706**, 8–24 (2011).
22. Liz-Marzán, L. M. Tailoring surface plasmons through the morphology and assembly of metal nanoparticles. *Langmuir* **22**, 32–41 (2006).
23. Cao, J., Sun, T. & Grattan, K. T. V. Gold nanorod-based localized surface plasmon resonance biosensors: A review. *Sensors Actuators, B Chem.* **195**, 332–351 (2014).
24. Ni, W., Kou, X., Yang, Z. & Wang, J. Tailoring longitudinal surface plasmon wavelengths, scattering and absorption cross sections of gold nanorods. *ACS Nano* **2**, 677–686 (2008).
25. Zheng, Y., Xiao, M., Jiang, S., Ding, F. & Wang, J. Coating fabrics with gold nanorods for colouring, UV-protection, and antibacterial functions. *Nanoscale* **5**, 788–795 (2013).
26. Howes, P. D., Rana, S. & Stevens, M. M. Plasmonic nanomaterials for biodiagnostics. *Chem. Soc. Rev.* **43**, 3835–53 (2014).
27. Satija, J., Punjabi, N., Mishra, D. & Mukherji, S. Plasmonic-ELISA: expanding horizons. *RSC Adv.* **6**, 85440–85456 (2016).
28. Chen, X., Liang, Y., Zhang, W., Leng, Y. & Xiong, Y. A colorimetric immunoassay based on glucose oxidase-induced AuNP aggregation for the detection of fumonisin B1. *Talanta* **186**, 29–35 (2018).
29. Zhan, L., Wu, W. B., Yang, L. & Huang, C. Z. Sensitive detection of respiratory syncytial virus based on a dual signal amplified plasmonic enzyme-linked immunosorbent assay. *Anal. Chim. Acta* **962**, 73–79 (2017).
30. Chen, T., Pourmand, M., Feizpour, A., Cushman, B. & Reinhard, B. M. Tailoring plasmon coupling in self-assembled one-dimensional Au nanoparticle chains through simultaneous

control of size and gap separation. *J. Phys. Chem. Lett.* **4**, 2147–2152 (2013).

31. Turkevich, J., Stevenson, P. C. & Hillier, J. A study of the nucleation and growth processes in the synthesis of colloidal gold. *Discuss. Faraday Soc.* **11**, 55–75 (1951).
32. de la Rica, R. & Stevens, M. M. Plasmonic ELISA for the ultrasensitive detection of disease biomarkers with the naked eye. *Nat. Nanotechnol.* **7**, 821–824 (2012).
33. Xuan, Z. *et al.* Plasmonic ELISA based on the controlled growth of silver nanoparticles. *Nanoscale* **8**, 17271–17277 (2016).
34. Gao, J. *et al.* Prereduction-promoted enhanced growth of silver nanoparticles for ultrasensitive colorimetric detection of alkaline phosphatase and carbohydrate antigen 125. *Talanta* **189**, 129–136 (2018).
35. Li, Y. *et al.* Multicolor ELISA based on alkaline phosphatase-triggered growth of Au nanorods. *Analyst* (2016). doi:10.1039/C6AN00117C
36. Yang, X. & Gao, Z. Enzyme-catalysed deposition of ultrathin silver shells on gold nanorods: a universal and highly efficient signal amplification strategy for translating immunoassay into a litmus-type test. *Chem. Commun. (Camb).* **51**, 6928–31 (2015).
37. Rodríguez-Lorenzo, L., De La Rica, R., Álvarez-Puebla, R. A., Liz-Marzán, L. M. & Stevens, M. M. Plasmonic nanosensors with inverse sensitivity by means of enzyme-guided crystal growth. *Nat. Mater.* **11**, 604–607 (2012).
38. Xu, S. *et al.* Highly Uniform Gold Nanobipyramids for Ultrasensitive Colorimetric Detection of Influenza Virus. *Anal. Chem.* **89**, 1617–1623 (2017).
39. Chandrasekar, G., Mougin, K., Haidara, H., Vidal, L. & Gnecco, E. Shape and size transformation of gold nanorods (GNRs) via oxidation process : A reverse growth mechanism. *Appl. Surf. Sci.* **257**, 4175–4179 (2011).

40. Tsung, C. *et al.* Selective Shortening of Single-Crystalline Gold Nanorods by Mild Oxidation. 5352–5353 (2006). doi:10.1021/ja060447t

41. Pesic, B. & Sergent, R. H. Reaction mechanism of gold dissolution with bromine. *Metall. Trans. B* **24**, 419–431 (1993).

42. Zhu, Q., Wu, J., Zhao, J. & Ni, W. Role of bromide in hydrogen peroxide oxidation of ctab-stabilized gold nanorods in aqueous solutions. *Langmuir* **31**, 4072–4077 (2015).

43. Rodríguez-Fernández, J., Pérez-Juste, J., Mulvaney, P. & Liz-Marzán, L. M. Spatially-directed oxidation of gold nanoparticles by Au(III)-CTAB complexes. *J. Phys. Chem. B* **109**, 14257–14261 (2005).

44. Ma, X. *et al.* Gold Nanorods as Colorful Chromogenic Substrates for Semiquantitative Detection of Nucleic Acids, Proteins, and Small Molecules with the Naked Eye. *Anal. Chem.* **88**, 3227–3234 (2016).

45. Saa, L., Coronado-Puchau, M., Pavlov, V. & Liz-Marzán, L. M. Enzymatic etching of gold nanorods by horseradish peroxidase and application to blood glucose detection. *Nanoscale* **6**, 7405 (2014).

46. Lin, Y. *et al.* Multicolor Colormetric Biosensor for the Determination of Glucose based on the Etching of Gold Nanorods. *Sci. Rep.* 1–7 (2016). doi:10.1038/srep37879

47. Ma, X. *et al.* A universal multicolor immunosensor for semiquantitative visual detection of biomarkers with the naked eyes. *Biosens. Bioelectron.* **87**, 122–128 (2017).

48. Chiu, R. Y. T. *et al.* Simultaneous concentration and detection of biomarkers on paper. *Lab Chip* **14**, 3021–30288 (2014).

49. Pereira, D. Y., Chiu, R. Y. T., Zhang, S. C. L., Wu, B. M. & Kamei, D. T. Single-step, paper-based concentration and detection of a malaria biomarker. *Anal. Chim. Acta* **882**, 83–

89 (2015).

50. Walter, H., Brooks, D. E. & Fisher, D. *Partitioning in Aqueous Two-Phase Systems: Theory, Methods, Uses, and Applications to Biotechnology*. (Academic Press, Inc, 1985).

51. Kenkare, P. U. & Hall, C. K. Modeling of phase separation in PEG–salt aqueous two-phase systems. *AIChE J.* **42**, 3508–3522 (1996).

52. Albertsson, P.-A. *Partition of Cell Particles and Macromolecules*. (John Wiley & Sons, Ltd, 1986).

53. Lladosa, E., Silvério, S. C., Rodríguez, O., Teixeira, J. A. & MacEdo, E. A. (Liquid + liquid) equilibria of polymer-salt aqueous two-phase systems for laccase partitioning: UCON 50-HB-5100 with potassium citrate and (sodium or potassium) formate at 23 °c. *J. Chem. Thermodyn.* **55**, 166–171 (2012).

54. Kabiri-Badr, M. & Cabezas, H. A thermodynamic model for the phase behavior of salt-polymer aqueous two-phase systems. *Fluid Phase Equilib.* **115**, 39–58 (1996).

55. Mashayekhi, F. *et al.* Enhancing the lateral-flow immunoassay for viral detection using an aqueous two-phase micellar system. *Anal. Bioanal. Chem.* **398**, 2955–2961 (2010).

56. Mashayekhi, F., Le, A. M., Nafisi, P. M., Wu, B. M. & Kamei, D. T. Enhancing the lateral-flow immunoassay for detection of proteins using an aqueous two-phase micellar system. *Anal. Bioanal. Chem.* **404**, 2057–2066 (2012).

57. Jue, E., Yamanishi, C. D., Chiu, R. Y. T., Wu, B. M. & Kamei, D. T. Using an aqueous two-phase polymer-salt system to rapidly concentrate viruses for improving the detection limit of the lateral-flow immunoassay. *Biotechnol. Bioeng.* **111**, 2499–2507 (2014).

58. Chiu, R. Y. T. *et al.* Dextran-Coated Gold Nanoprobes for the Concentration and Detection of Protein Biomarkers. *Ann. Biomed. Eng.* **42**, 2322–2332 (2014).

59. Chiu, R. Y. T., Thach, A. V., Wu, C. M., Wu, B. M. & Kamei, D. T. An aqueous two-phase system for the concentration and extraction of proteins from the interface for detection using the lateral-flow immunoassay. *PLoS One* **10**, e0142654 (2015).

60. Zhang, L. *et al.* Hierarchical Flowerlike Gold Nanoparticles Labeled Immunochromatography Test Strip for Highly Sensitive Detection of *Escherichia coli* O157:H7. *Langmuir* **31**, 5537–5544 (2015).

61. Choi, D. H. *et al.* A dual gold nanoparticle conjugate-based lateral flow assay (LFA) method for the analysis of troponin I. *Biosens. Bioelectron.* **25**, 1999–2002 (2010).

62. Liu, G. Gold-nanoparticle-decorated silica nanorods for sensitive visual detection of proteins. (2014).

63. Cho, I.-H., Bhunia, A. & Irudayaraj, J. Rapid pathogen detection by lateral-flow immunochromatographic assay with gold nanoparticle-assisted enzyme signal amplification. *Int. J. Food Microbiol.* **206**, 60–66 (2015).

64. Duan, D. *et al.* Nanozyme-strip for rapid local diagnosis of Ebola. *Biosens. Bioelectron.* **74**, 134–141 (2015).

65. Gao, Z. *et al.* Platinum-Decorated Gold Nanoparticles with Dual Functionalities for Ultrasensitive Colorimetric in Vitro Diagnostics. *Nano Lett.* **17**, 5572–5579 (2017).

66. Yang, W. *et al.* A colloidal gold probe-based silver enhancement immunochromatographic assay for the rapid detection of abrin-a. *Biosens. Bioelectron.* **26**, 3710–3713 (2011).

67. Badu-Tawiah, A. K. *et al.* Polymerization-based signal amplification for paper-based immunoassays. *Lab Chip* **15**, 655–659 (2015).

68. Cho, J. H., Paek, E. H., Cho, I. I. H. & Paek, S. H. An enzyme immunoanalytical system based on sequential cross-flow chromatography. *Anal. Chem.* **77**, 4091–4097 (2005).

69. Fu, E., Lutz, B., Kauffman, P. & Yager, P. Controlled reagent transport in disposable 2D paper networks. *Lab Chip* **10**, 918–920 (2010).

70. Ramachandran, S., Fu, E., Lutz, B. & Yager, P. Long-term dry storage of an enzyme-based reagent system for ELISA in point-of-care devices. *Analyst* **139**, 1456–62 (2014).

71. Fu, E. & Downs, C. Progress in the development and integration of fluid flow control tools in paper microfluidics. *Lab Chip* **17**, 614–628 (2017).

72. Naunheim, M. R. *et al.* Immediate and Delayed Complications Following Endoscopic Skull Base Surgery. *J. Neurol. Surgery, Part B Skull Base* **76**, 390–396 (2015).

73. Ramakrishnan, V. R., Kingdom, T. T., Nayak, J. V, Hwang, P. H. & Orlandi, R. R. Nationwide incidence of major complications in endoscopic sinus surgery. *Int. Forum Allergy Rhinol.* **2**, 34–39 (2012).

74. Daneshi, A. *et al.* Complications in a series of 4400 paediatric cochlear implantation. *Int. J. Pediatr. Otorhinolaryngol.* **79**, 1401–1403 (2015).

75. Rao, N. & Redleaf, M. Spontaneous middle cranial fossa cerebrospinal fluid otorrhea in adults. *Laryngoscope* **126**, 464–468 (2016).

76. Marshall, A. H., Jones, N. S. & Robertson, I. J. A. An algorithm for the management of CSF rhinorrhoea illustrated by 36 cases. *Rhinology* **37**, 182–185 (1999).

77. Oakley, G. M., Alt, J. A., Schlosser, R. J., Harvey, R. J. & Orlandi, R. R. Diagnosis of cerebrospinal fluid rhinorrhea: An evidence-based review with recommendations. *Int. Forum Allergy Rhinol.* **6**, 8–16 (2016).

78. Arrer, E. *et al.* β-trace protein as a marker for cerebrospinal fluid rhinorrhea. *Clin. Chem.* **48**, 939–941 (2002).

79. Reiber, H., Walther, K. & Althaus, H. Beta-trace protein as sensitive marker for CSF

rhinorrhea and CSF otorrhea. *Acta Neurol. Scand.* **108**, 359–62 (2003).

80. Schnabel, C. *et al.* Comparison of B2-Transferrin and B-Trace Protein for Detection of Cerebrospinal Fluid in Nasal and Ear Fluids. *Clin. Chem.* **50**, 661–663 (2004).

81. Bachmann-Harildstad, G. Diagnostic values of beta-2 transferrin and beta-trace protein as markers for cerebrospinal fluid fistula. *Rhinology* **46**, 82–85 (2008).

82. Morell-Garcia, D., Bauça, J. M., Sastre, M. P., Yañez, A. & Llompart, I. Sample-dependent diagnostic accuracy of prostaglandin D synthase in cerebrospinal fluid leak. *Clin. Biochem.* **50**, 27–31 (2017).

83. Bernasconi, L. *et al.* Retrospective validation of a beta-trace protein interpretation algorithm for the diagnosis of cerebrospinal fluid leakage. *Clin Chem Lab Med* **55**, 554–560 (2017).

84. Oberascher, G. & Arrer, E. *Efficiency of Various Methods of Identifying Cerebrospinal Fluid in Oto- and Rhinorrhea*. *ORL; journal for oto-rhino-laryngology and its related specialties* **48**, (1986).

85. Normansell, D. E., Stacy, E. K., Booker, C. F. & Butler, T. Z. Detection of beta-2 Transferrin in Otorrhea ad Rhinorrhea in a Routine Clinical Laboratory Setting. *Clin. Diagn. Lab. Immunol.* **1**, 68–70 (1994).

86. Foster, M. C. *et al.* Serum β-Trace Protein and β2-Microglobulin as Predictors of ESRD, Mortality, and Cardiovascular Disease in Adults with CKD in the Chronic Renal Insufficiency Cohort (CRIC) Study. *Am. J. Kidney Dis.* **68**, 68–76 (2016).

87. Melegos, D. N., Grass, L., Pierratos, A. & Diamandis, E. P. Highly elevated levels of prostaglandin D synthase in the serum of patients with renal failure. *Urology* **53**, 32–37 (1999).

88. Melegos, D. N., Diamandis, E. P., Oda, H., Urade, Y. & Hayaishi, O. Immunofluorometric

assay of prostaglandin D synthase in human tissue extracts and fluids. *Clin. Chem.* **42**, 1984–1991 (1996).

89. Risch, L. *et al.* Rapid, accurate and non-invasive detection of cerebrospinal fluid leakage using combined determination of beta-trace protein in secretion and serum. *Clin. Chim. Acta.* **351**, 169–76 (2005).

90. Prosser, J. D., Vender, J. R. & Solares, C. A. Traumatic Cerebrospinal Fluid Leaks. *Otolaryngol. Clin. North Am.* **44**, 858–859 (2011).

91. Daudia, A., Biswas, D. & Jones, N. S. Risk of meningitis with cerebrospinal fluid rhinorrhea. *Ann. Otol. Rhinol. Laryngol.* **116**, 902–905 (2007).

92. Bernal-Sprekelsen, M., Bleda-Vázquez, C. & Carrau, R. L. Ascending Meningitis Secondary to Traumatic Cerebrospinal Fluid Leaks. *Am. J. Rhinol.* **14**, 257–260 (2000).

93. Eljazzar, R., Loewenstern, J., Dai, J. B., Shrivastava, R. K. & Iloreta, A. M. Detection of Cerebrospinal Fluid Leaks: Is There a Radiologic Standard of Care? A Systematic Review. *World Neurosurg.* **127**, 307–315 (2019).

94. Fransen, P., Sindic, C. J. M., Thauvoy, C., Laterre, C. & Stroobandt, G. Highly sensitive detection of beta-2 transferrin in rhinorrhea and otorrhea as a marker for cerebrospinal fluid (C.S.F.) leakage. *Acta Neurochir. (Wien).* **109**, 98–101 (1991).

95. Athanasia, W. *et al.* Diagnostic Relevance of Beta 2-Transferrin for the Detection of Cerebrospinal Fluid Fistulas. **130**, 1178–1184 (2004).

96. Papadea, C. & Schlosser, R. J. Rapid Method for beta-2-Transferrin in Cerebrospinal Fluid Leakage Using an Automated Immunofixation Electrophoresis System. *Clin. Chem.* **51**, 464–470 (2005).

97. McCudden, C. R. *et al.* Evaluation of high resolution gel β 2 -transferrin for detection of

cerebrospinal fluid leak. *Clin. Chem. Lab. Med.* **51**, 311–315 (2013).

98. Mantur, M. *et al.* Cerebrospinal fluid leakage-Reliable diagnostic methods. *Clin. Chim. Acta* **412**, 837–840 (2011).

99. Reiber, H. Dynamics of brain-derived proteins in cerebrospinal fluid. *Clin. Chim. Acta* **310**, 173–186 (2001).

100. Kita, A. E., Bradbury, D. W., Taylor, Z. D., Kamei, D. T. & St. John, M. A. Point-of-Care Cerebrospinal Fluid Detection. *Otolaryngol. Neck Surg.* **159**, 824–829 (2018).

101. Borysiak, M. D. *et al.* Translating diagnostic assays from the laboratory to the clinic: analytical and clinical metrics for device development and evaluation. *Lab Chip* **16**, 1293–1313 (2016).

102. Mozaffarian, D. *et al. Heart Disease and Stroke Statistics—2016 Update*. *Circulation* **133**, (2016).

103. Heidenreich, P. A. *et al.* Forecasting the future of cardiovascular disease in the United States: A policy statement from the American Heart Association. *Circulation* **123**, 933–944 (2011).

104. Ziff, O. J. & Kotecha, D. Digoxin: The good and the bad. *Trends Cardiovasc. Med.* **26**, 585–595 (2016).

105. Grześk, G. *et al.* Therapeutic drug monitoring of digoxin- 20 years of experience. *Pharmacol. Reports* **70**, 184–189 (2018).

106. R., V. J., S.A., J. & M., G. Standards of laboratory practice: Cardiac drug monitoring. *Clin. Chem.* **44**, 1096–1109 (1998).

107. Kang, J. S. & Lee, M. H. Overview of therapeutic drug monitoring. *Korean J. Intern. Med.* **24**, 1–10 (2009).

108. Aonuma, K. *et al.* Guidelines for therapeutic drug monitoring of cardiovascular drugs clinical use of blood drug concentration monitoring (Jcs 2015) — digest version —. *Circ. J.* **81**, 581–612 (2017).

109. Sanavio, B. & Krol, S. On the Slow Diffusion of Point-of-Care Systems in Therapeutic Drug Monitoring. *Front. Bioeng. Biotechnol.* **3**, 1–15 (2015).

110. Tang, L. & Li, J. Plasmon-Based Colorimetric Nanosensors for Ultrasensitive Molecular Diagnostics. *ACS Sensors* acssensors.7b00282 (2017). doi:10.1021/acssensors.7b00282

111. Yin, H. Y., Chu, P. T., Tsai, W. C. & Wen, H. W. Development of a barcode-style lateral flow immunoassay for the rapid semi-quantification of gliadin in foods. *Food Chem.* **192**, 934–942 (2016).

112. Kita, A. E., Bradbury, D. W., Taylor, Z. D., Kamei, D. T. & St. John, M. A. Point-of-Care Cerebrospinal Fluid Detection. *Otolaryngol. - Head Neck Surg. (United States)* **159**, 824–829 (2018).

113. Zhang, J., Shen, Z., Xiang, Y. & Lu, Y. Integration of Solution-Based Assays onto Lateral Flow Device for One-Step Quantitative Point-of-Care Diagnostics Using Personal Glucose Meter. *ACS Sensors* **1**, 1091–1096 (2016).

114. Ruppert, C., Phogat, N., Laufer, S., Kohl, M. & Deigner, H. P. A smartphone readout system for gold nanoparticle-based lateral flow assays: application to monitoring of digoxigenin. *Microchim. Acta* **186**, (2019).

115. Ye, X. *et al.* Improved size-tunable synthesis of monodisperse gold nanorods through the use of aromatic additives. *ACS Nano* **6**, 2804–2817 (2012).

116. Loynachan, C. N. *et al.* Platinum Nanocatalyst Amplification: Redefining the Gold Standard for Lateral Flow Immunoassays with Ultra-Broad Dynamic Range. *ACS Nano*

acsnano.7b06229 (2017). doi:10.1021/acsnano.7b06229

117. Li, J., Liu, W., Wu, X. & Gao, X. Mechanism of pH-switchable peroxidase and catalase-like activities of gold, silver, platinum and palladium. *Biomaterials* **48**, 37–44 (2015).

118. Liu, Y., Wu, H., Li, M., Yin, J.-J. & Nie, Z. pH dependent catalytic activities of platinum nanoparticles with respect to the decomposition of hydrogen peroxide and scavenging of superoxide and singlet oxygen. *Nanoscale* **6**, 11904–11910 (2014).

119. Zhu, Z. *et al.* Au@pt nanoparticle encapsulated target-responsive hydrogel with volumetric bar-chart chip readout for quantitative point-of-care testing. *Angew. Chemie - Int. Ed.* **53**, 12503–12507 (2014).

120. Saa, L., Grinyte, R., Sánchez-Iglesias, A., Liz-Marzán, L. M. & Pavlov, V. Blocked Enzymatic Etching of Gold Nanorods: Application to Colorimetric Detection of Acetylcholinesterase Activity and Its Inhibitors. *ACS Appl. Mater. Interfaces* **8**, 11139–11146 (2016).

121. D.J., T., C., N., A.H., T. & A.A., V. Cost-effectiveness of therapeutic drug monitoring: A systematic review. *Ther. Drug Monit.* **27**, 10–17 (2005).

122. Meredith, N. *et al.* Paper-Based Analytical Devices for Environmental Analysis. *Analyst* (2016). doi:10.1039/C5AN02572A

123. Gubala, V., Harris, L. F., Ricco, A. J., Tan, M. X. & Williams, D. E. Point of care diagnostics: status and future. *Anal. Chem.* **84**, 487–515 (2012).

124. Fu, E., Kauffman, P., Lutz, B. & Yager, P. Chemical signal amplification in two-dimensional paper networks. *Sensors Actuators, B Chem.* **149**, 325–328 (2010).

125. Fu, E. *et al.* Enhanced sensitivity of lateral flow tests using a two-dimensional paper network format. *Anal. Chem.* **83**, 7941–7946 (2011).

126. Lutz, B. R., Trinh, P., Ball, C., Fu, E. & Yager, P. Two-dimensional paper networks: programmable fluidic disconnects for multi-step processes in shaped paper. *Lab Chip* **11**, 4274–4278 (2011).

127. Fu, E. *et al.* Two-dimensional paper network format that enables simple multistep assays for use in low-resource settings in the context of malaria antigen detection. *Anal. Chem.* **84**, 4574–4579 (2012).

128. Park, J., Shin, J. H. & Park, J. K. Pressed Paper-Based Dipstick for Detection of Foodborne Pathogens with Multistep Reactions. *Anal. Chem.* **88**, 3781–3788 (2016).

129. Toley, B. J. *et al.* Tunable-Delay Shunts for Paper Microfluidic Devices. *Anal. Chem.* **85**, 11545–52 (2013).

130. Gerbers, R., Foellscher, W., Chen, H., Anagnostopoulos, C. & Faghri, M. A New Paper-Based Platform Technology for Point-of-Care Diagnostics. *Lab Chip* **14**, 4042–4049 (2014).

131. Toley, B. J. *et al.* A versatile valving toolkit for automating fluidic operations in paper microfluidic devices. *Lab Chip* **15**, 1432–1444 (2015).

132. Phillips, E. A., Shen, R., Zhao, S. & Linnes, J. C. Thermally actuated wax valves for paper-fluidic diagnostics. *Lab Chip* **16**, 4230–4236 (2016).

133. Kong, T. *et al.* A fast, reconfigurable flow switch for paper microfluidics based on selective wetting of folded paper actuator strips. *Lab Chip* **17**, 3621–3633 (2017).

134. Lutz, B. *et al.* Dissolvable fluidic time delays for programming multi-step assays in instrument-free paper diagnostics. *Lab Chip* **13**, 2840–2847 (2013).

135. Jahanshahi-Anbuhi, S. *et al.* Automating Multi-Step Paper-Based Assays Using Integrated Layering of Reagents. *Lab Chip* **17**, 943–950 (2017).

136. Washburn, E. W. The dynamics of capillary flow. *Phys. Rev.* **17**, 273–283 (1921).

137. Camplisson, C. K., Schilling, K. M., Pedrotti, W. L., Stone, H. A. & Martinez, A. W. Two-ply channels for faster wicking in paper-based microfluidic devices. *Lab Chip* **15**, 4461–4466 (2015).

138. Asenjo, J. A. & Andrews, B. A. Aqueous two-phase systems for protein separation: Phase separation and applications. *J. Chromatogr. A* **1238**, 1–10 (2012).

139. Oh, K. W., Lee, K., Ahn, B. & Furlani, E. P. Design of pressure-driven microfluidic networks using electric circuit analogy. *Lab Chip* **12**, 515–45 (2012).

140. Gao, L. *et al.* Intrinsic peroxidase-like activity of ferromagnetic nanoparticles. *Nat. Nanotechnol.* **2**, 577–583 (2007).

141. Mosley, G. L. *et al.* Improved lateral-flow immunoassays for chlamydia and immunoglobulin M by sequential rehydration of two-phase system components within a paper-based diagnostic. *Microchim. Acta* **184**, 4055–4064 (2017).

142. Pokhrel, P., Hu, C. & Mao, H. Detecting the Coronavirus (COVID-19). *ACS sensors* (2020). doi:10.1021/acssensors.0c01153

143. Kammila, S. *et al.* A rapid point of care immunoswab assay for SARS-CoV detection. *J. Virol. Methods* **152**, 77–84 (2008).

144. Che, X. Y. *et al.* Nucleocapsid protein as early diagnostic marker for SARS. *Emerg. Infect. Dis.* **10**, 1947–1949 (2004).

145. Linares, M. *et al.* Panbio antigen rapid test is reliable to diagnose SARS-CoV-2 infection in the first 7 days after the onset of symptoms. *J. Clin. Virol.* **113**, (2020).

146. Santiago, I. Trends and Innovations in Biosensors for COVID-19 Mass Testing. *ChemBioChem* **21**, 2880–2889 (2020).

147. Lippi, G., Simundic, A. M. & Plebani, M. Potential preanalytical and analytical

vulnerabilities in the laboratory diagnosis of coronavirus disease 2019 (COVID-19). *Clin. Chem. Lab. Med.* **58**, 1070–1076 (2020).

148. Basso, D. *et al.* SARS-CoV-2 RNA identification in nasopharyngeal swabs: Issues in pre-analytics. *Clin. Chem. Lab. Med.* **58**, 1579–1586 (2020).

149. Liu, D. *et al.* Nanozyme chemiluminescence paper test for rapid and sensitive detection of SARS-CoV-2 antigen. *Biosens. Bioelectron.* **173**, 112817 (2021).

150. Peng, T. *et al.* Enhancing sensitivity of lateral flow assay with application to SARS-CoV-2. *Appl. Phys. Lett.* **117**, 2–5 (2020).

151. Du, Y. *et al.* Development of high affinity monobodies recognizing SARS-CoV-2 antigen. 1–30 (2020). doi:10.21203/rs.3.rs-25828/v1

152. Tholen, D. W. *et al. Protocols for Determination of Limits of Detection and Limits of Quantitation; Approved Guideline Global Consensus Standardization for Health Technologies (EP17-A)*. **24**, (2004).

153. Holstein, C. a., Griffin, M., Hong, J. & Sampson, P. D. S. M. for D. and C. L. of D. of B. Statistical Method for Determining and Comparing Limits of Detection of Bioassays. *Anal. Chem.* 150925090850005 (2015). doi:10.1021/acs.analchem.5b02082

154. Selby, C. Interference in Immunoassay. *Ann. Clin. Biochem. An Int. J. Biochem. Lab. Med.* **36**, 704–721 (1999).